Mixed-Signal Instrumentation for Large-Signal Device Characterization and Modelling

Mauro Marchetti

Mixed-Signal Instrumentation for Large-Signal Device Characterization and Modelling

PROEFSCHRIFT

ter verkrijging van de graad van doctor
aan de Technische Universiteit Delft,
op gezag van de Rector Magnificus Prof. ir. K. C. A. M. Luyben,
voorzitter van het College voor Promoties,
in het openbaar te verdedigen

op maandag 25 november 2013 om 15.00uur

door

Mauro MARCHETTI

Dottore in Ingegneria Elettronica
van Università degli Studi di Napoli "Federico II", Italië
geboren te Napoli, Italië

Dit proefschrift is goedgekeurd door de promotor:
Prof. dr. J. R. Long

Samenstelling promotiecommissie:

Rector Magnificus, voorzitter
Prof. dr. J.R. Long, Technische Universiteit Delft, promotor
Dr. ing. L.C.N. de Vreede, Technische Universiteit Delft, toegevoegd promotor
Prof. dr. L.K. Nanver, Technische Universiteit Delft
Prof. dr. V. Teppati, Eidgenössische Technische Hochschule Zürich
Prof. dr. H.F.F. Jos, Chalmers University of Technology
Prof. dr. D. Schreurs, Katholieke Universiteit Leuven
Dr. M. Vanden Bossche, National Instruments Belgium NV/SA
Prof. dr. A. Neto, Technische Universiteit Delft, reservelid

Mauro Marchetti,
Mixed-Signal Instrumentation for Large-Signal Device Characterization and Modelling,
Ph.D. Thesis Delft University of Technology,
with summary in Dutch.

Keywords: load-pull, isothermal, large-signal, complex modulated signals, dynamic range, linearity, device, power amplifier, radio frequency (RF), base station, handset, high power.

ISBN: 978-94-6203-471-6

Cover design by twoeight studio, www.twoeight.it.
Printed by CPI, Wohrmann Print Service, Zutphen, the Netherlands.

To my family

Contents

Chapter 1

Introduction

The appearance of modern smart phones and their quick penetration to consumer markets has drastically changed the way we communicate as a society. The manner in which social networks, for example, are influencing every day life has been magnified by the capabilities of truly portable, always connected devices. While just a few years ago the cellular phone was only used for voice calls and SMS, the newer generation smart phones are reaching more and more the capabilities of pocket size personal computers which are always connected to the network. Consequently, applications ranging from internet browsing to video chatting, from high-quality video streaming to internet calls and social networks, which were previously tied to personal computers alone, have become accessible anytime and from almost anywhere to the user.

As a result, it is becoming increasingly more difficult to imagine our life without a mobile internet connection. This trend is reflected in the 2012 Cisco World Technology Report [1], which indicates that more than 60 % of "Gen Y" (18 to 30 year olds) do not even wait to get out of bed in the morning before checking their smart phones, while more than 40 % of them (including the author of this thesis) would feel anxious, almost lost, if they couldn't check their smart phones constantly.

1.1 Trends in wireless communication

As more and more people and devices get connected, the amount of data traffic increases exponentially. Consequently, while according to the United Nations expectations there will be 7.6 billion people in 2017, in that same year, based on the scenario depicted by the Cisco visual networking index (VNI) global mobile data traffic forecast 2012-2017 [2], there will be more internet access

Figure 1.1: Mobile data traffic forecast vs. time in exabytes per month. Source Cisco VNI Mobile Forecast [2].

points than people on this planet. Moreover, driven by applications such as high definition video streaming or cloud computing, the mobile data traffic will grow 13 times in the coming five years, increasing from the 0.9 exabytes per month of 2012 to the 11.2 exabytes per month of 2017, as shown in Fig. 1.1.

The exponential increase in the amount of mobile data transferred and the consequent request for higher data rates in communication systems has led, over the past decade, to the introduction of 3G and 4G communication standards, such as UMTS and LTE, which employ larger bandwidths and more complex modulation schemes to achieve higher data rate capabilities. The development of data rates over time in wireless networks is depicted in Fig. 1.2. It can be seen that the transmission speed has been increasing by approximately a factor of 10 every 5 years [3].

Another important aspect in the development of mobile communications and the related infrastructure is the electricity consumption of mobile networks. From an economic point of view this is a primary issue, since the biggest portion of the operational expenditures (OPEX) of mobile networks resides into energy costs. In fact, it is estimated that the worldwide mobile network OPEX for electricity is more than 10 billion dollars [4]. Furthermore, due to the growing awareness of the environmental impact of wireless communication systems, reducing their energy consumption is becoming a more crucial point. According to some figures [5], information and communication technology (ICT) is already responsible for about 2 to 4 % of the world-wide

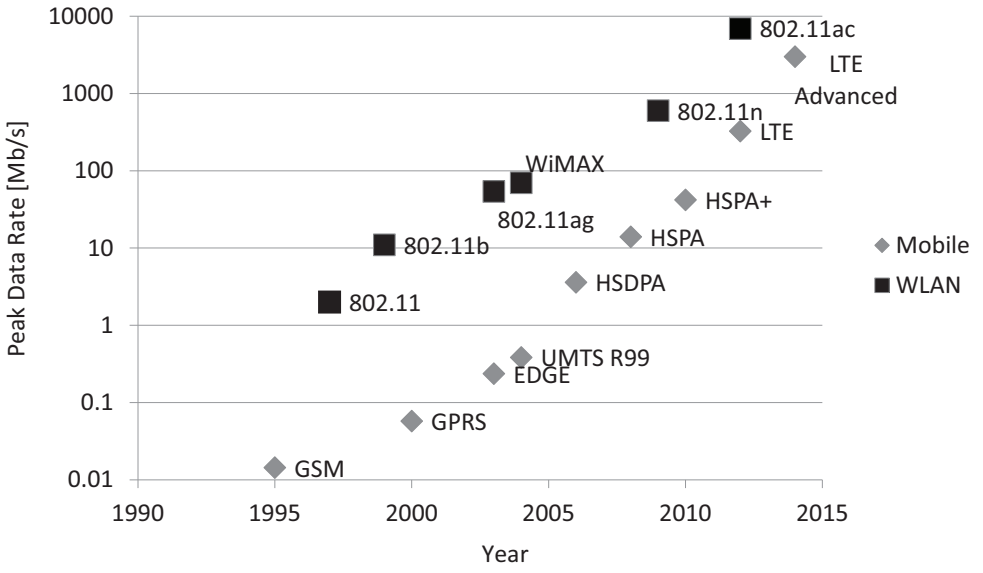

Figure 1.2: Development of data rates over time in wireless networks [3].

CO_2 emissions and its contribution is growing by $16 - 20$ % yearly, doubling every 4 to 5 years. To put things into perspective, the CO_2 emissions caused by ICT correspond already to those caused by all international air traffic [3], and it is equivalent to the annual greenhouse gas emissions from about 8 million cars [4]. While in 2002, the contribution of mobile communications corresponded only to about 10 % of the total amount for ICT, this value is expected to grow three times by 2020 [6].

However, when considering a wireless network, it is estimated that 60 to 80 % of the total energy is consumed by the base-station [4], the fixed radio station which relays the information to and from the mobile devices. As a consequence, cellular network operators have been placing particular emphasis into trying to minimize the energy consumption of base-stations, by constantly evaluating different strategies, ranging from hardware improvements, to better cooling approaches, to advanced operation and deployment schemes. A few potential opportunities which are currently under study, and that can allow a significant reduction of the energy expenditure of wireless networks involve:

- Operational strategies such as dynamic shut down of some base-stations during off-peak hours [4].
- Network architectures based on low power microcells, instead of high power macrocells [3].

- The increase of the transmission range of base-stations by using smart antenna technology [7], such as multiple receiving and transmitting antennas (Multiple-Input and Multiple-Output).
- The design and implementation of novel and more energy efficient hardware.

Nevertheless, when considering the architecture of any base-station, the most "power-hungry" component in these networks is the power amplifier (PA) which is boosting the signal power before this is transmitted over the air [8]. This is true not only because of the power consumption of the amplifier itself, but also due to the energy which is necessary to cool it. Therefore, it is not surprising that, despite all the different available strategies for minimizing energy consumption, there is currently, worldwide, an enormous interest in designing more energy efficient PAs, while at the same time improving their signal handling capabilities in terms of bandwidth and linearity [8].

1.2 Requirements on the power amplifier

Society's need for higher data rates and reduced energy consumption translates into very stringent technology requirements for the underlying hardware.

First of all, modern advanced modulation schemes employ both phase and amplitude modulation to increase the transmission data-rate. As a consequence, the signal peak-to-average ratio, which is the ratio between the peak power and the average power of the signal, is high (e.g., ≈ 9.8 dB for a typical W-CDMA signal [9] for downlink transmission). This requires that the PA is as efficient as possible not only close to compression, but also in power back-off where statistically the PA is transmitting most of the time, and therefore most of the energy is consumed. This can be easily explained by looking, as an example, at the probability distribution function of a W-CDMA signal in Fig. 1.3, which shows how the signal instantaneous power has the highest probability to be about 9.8 dB in back-off with respect to the peak power.

Secondly, to operate correctly, the wireless transmitter should be able to broadcast the desired signals without generating significant in-band distortion and without interfering with the other channels. This means that the signal should not leak considerably into the other transmission channels and therefore its spectrum should not exceed the levels given by the so called spectral mask (see Fig. 1.4), which is defined by the communication standard. This is achieved either by designing PAs which are extremely linear over a wide frequency range, or by linearizing the final transmitted signal by digitally predistorting the data at the source to compensate for the PA distortion.

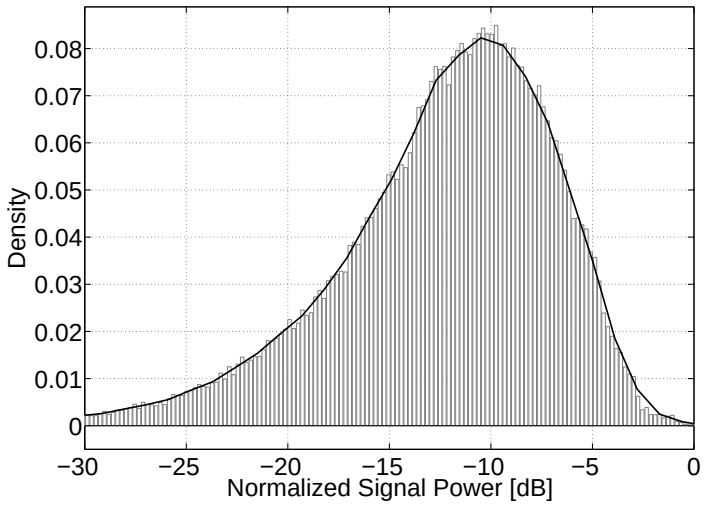

Figure 1.3: Probability Density Function (PDF) for a downlink W-CDMA signal [9].

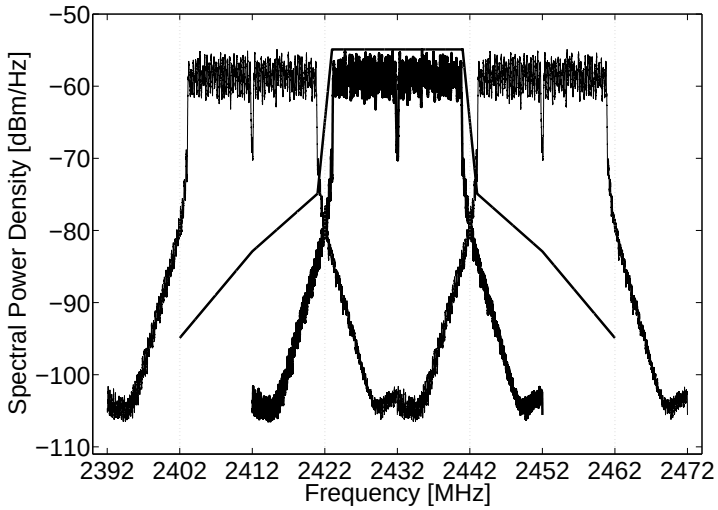

Figure 1.4: Example of a spectral mask of a 802.11n WiFi signal. The transmitted signal should not exceed the levels specified by the spectral mask to avoid interfering with the other channels [10].

To complicate matters, the demands for high efficiency and high linearity are normally in conflict with each other. The linearity requirement, in fact, could very simplistically be met by operating the PA well below its saturation point, in its linear region of operation. However, since the peak efficiency of a PA is normally achieved at peak output power, this would drastically reduce PA efficiency [11]. On the other hand, driving the PA closer to its saturation point, in its nonlinear region of operation, would certainly increase efficiency, but would result in nonlinear distortion effects.

For this reason, higher complexity amplifier concepts like Doherty [12], outphasing [13] and envelope tracking [14], which make use of dynamic variations of the load and voltage conditions for the output stage transistor(s), are becoming increasingly more popular, since they can relax the compromise between efficiency and linearity. It is clear that all these constraints on efficiency and linearity, in combination with these dynamic changes to the operating conditions for the active devices, make designing a power amplifier capable of meeting today's communication industry standards a challenging task, which requires accurate, fast and versatile measurement tools.

1.3 The need for advanced measurement tools

Looking in detail at the hardware design of state-of-the-art PAs for telecommunications, it can be stated that, for a given transistor technology, the performance parameters of a power amplifier depend entirely on how well the active devices, embedded in these circuits, are matched (i.e., electrically terminated), or embedded in their surrounding circuitry. In other words, active devices employed in these applications can only perform well if the proper electrical terminations are provided around the fundamental frequency band, as well as at all of the other frequencies (i.e., harmonics and baseband), because they strongly influence the device operation in terms of linearity and efficiency [15]. Therefore, a PA designer has to find the optimum trade-off among the different performance parameters, such as efficiency, linearity and output power, by "searching" the multi-dimensional design space across all of the different tunable parameters, such as bias, source and load impedance at baseband, fundamental and harmonic frequencies.

To accomplish this difficult task, the PA designer has to rely on either a model of the active device to perform the design in a circuit simulator, or on measurement data coming from a load-pull measurement system (see Chapter 3), which can measure the transistor performance parameters, such

as output power, efficiency, linearity, and many others, while tuning the various impedances offered to the active device.

Due to the aforementioned need to operate the transistor close to its nonlinear region, the models used for PA design need to correctly represent the large-signal and distortion behaviors of the active device. Moreover, to properly predict the transistor performance when employing wideband complex modulated signals, effects such as bias or temperature-induced memory [16] must be included in the model. Finally, the transistor model needs to be verified.

Therefore, to enable the extraction and the verification of accurate large-signal transistor models, there is a great need for advanced large-signal RF and microwave measurement tools. In fact, while linear device characterization (e.g., small-signal S-parameters) is mainly useful to extract the small-signal behavior of the transistor, pulsed DC, RF and large-signal measurements are mandatory to extract the nonlinear behavior of the active device and to verify the model. As an example, pulsed-DC and S-parameters measurements are required to characterize the active device under isothermal conditions (maintaining the core of the transistor at a constant temperature), in order to develop device models which include self-heating or trapping effects [17–20]. Moreover, load-pull measurements are necessary to obtain realistic large-signal data (e.g., gain and phase distortion data), for the extraction of large-signal behavioral models [21], or for model validation.

Additionally, since the model creation process can be a lengthy and cumbersome task, it is in many cases common practice to directly use load-pull measurement data for all activities related to PA design, from the technology development to the actual power amplifier design. Therefore it is of fundamental importance that the measurement data extracted from these characterization systems is able to predict with the highest level of accuracy the active device behavior in the final application environment (i.e., circuit termination and signal stimulus).

However, in spite of the significant progress made over the last decade in the field of RF measurements, there is still a great need for more accurate and advanced isothermal and large-signal characterization systems. In particular, pulsed-DC and S-parameter measurement systems still suffer from limitations in the minimum pulse widths that can be used and in measurement accuracy [22–26]. These impairments limit the usability of these systems for the characterization of new device technologies under truly isothermal conditions.

A comparable situation exists in load-pull measurement techniques. Although significant advances were made during past years [27], bringing conventional load-pull setups employing passive mechanical tuners and power meters

to advanced load-pull setups with large-signal vector measurements, there is still a big discrepancy between these traditional single-tone or two-tones characterization methods, and the actual signal conditions present in telecommunication systems operating with standard compliant signals like WCDMA or LTE.

As a consequence, the development and testing of new power amplifier technologies (e.g., LDMOS, GaN, SiGe, etc.) and their application in PAs are significantly hampered, yielding costly and lengthy technology and design iterations.

1.4 Thesis objectives

Having reviewed in Section 1.1 and 1.2 the current trends in the telecommunication industry and how these specifically reflect on the PA development, two major areas of improvements for PAs can be identified: the increase in available bandwidth, and the improvement of the overall average efficiency for modern communication signals, while at the same time satisfying the linearity specifications of the communication standard under consideration.

This thesis concentrates on the development of advanced large-signal measurement and characterization tools that support transistor technology development, model extraction and validation, and design of PAs that address these new communication standards. In particular, the measurement systems which will be described throughout this thesis work aim to extend the limits of state-of-the-art, large-signal characterization systems in terms of bandwidth, peak output power, speed and multi-functional capabilities.

For this purpose, an innovative mixed-signal approach, which replaces traditional analog techniques with digital data acquisition and digital signal generation and advanced digital signal processing, will be followed. This method provides, compared to traditional techniques, a much higher flexibility, functionality, performance and speed in many different applications.

In particular, to support compact model developments, and to facilitate the characterization of RF / microwave devices under truly isothermal conditions, the first part of this thesis work focuses on the development of an innovative pulsed-DC and pulsed-RF system, capable of providing very short DC and RF pulses (down to 200 ns), with arbitrarily low duty-cycle and an improved dynamic range. The setup will be used to characterize several different PA device technologies to gain insight into their electrical / thermal behavior.

The second, and dominant part of this thesis work introduces a revolutionary active harmonic load-pull approach to enable for the first time the characterization of RF and microwave transistors under realistic (circuit-like) condi-

tions with wideband modulated signals. By further exploiting this technique, a system will be presented to allow extremely high-speed PA device characterization of up to 1000 measurement points per minute, with impedance control of up to three harmonics, and the capability to measure RF voltage and current waveforms at the device under test. The usefulness of the realized system will be evaluated by applying the newly developed load-pull characterization system to several relevant application examples.

1.5 Thesis outline

This thesis is organized as follows.

In Chapter 2, the theory and the requirements for pulsed-RF and pulsed-DC measurements are discussed. Moreover, a new isothermal measurement approach with its hardware implementation is introduced, providing the ability to measure with DC and RF pulses as low as 200 ns, while featuring a high dynamic range under pulsed-RF conditions. The realized system performance is discussed in detail through a set of benchmarks, and some measurement examples on active devices are provided.

In Chapter 3, conventional passive and active source and load-pull architectures are reviewed. The basic limitations of conventional load-pull measurement systems are examined, with particular attention to the problems arising when characterizing devices with wideband complex modulated signals. Moreover, the requirements of active load-pull for performing high power measurements with complex modulated signals are also explained.

In Chapter 4, a new active harmonic load-pull system based on a mixed-signal approach is developed and described in detail. The system and the underlying measurement concepts were developed during this thesis work specifically to solve the problems of conventional load-pull setups when dealing with wideband modulated signals. In its current implementation, it enables the measurement of active devices up to 120 MHz of modulation bandwidth. Measurement data highlighting the system performance, and measurement results on active devices are presented.

In Chapter 5, a new approach for enabling high-speed multidimensional source and load-pull parameter sweeps is introduced. The method described allows any combination of multiple parameters (e.g., input power and/or fundamental and harmonic load impedance) to be swept, at a very high speed, while maintaining all other parameters (e.g., second harmonic source impedance) accurately controlled to a user-defined constant value. Moreover, several measurements are reported, with particular emphasis on the high-power capabilities of the system, both in CW as well as under modulated

signal excitations.

In Chapter 6, the basic theory behind the measurement of the high frequency time-domain voltage and current waveforms at the device reference planes is discussed. An extension of the mixed-signal load-pull system described in the previous chapters is presented, with particular attention on the requirements of the calibration device used for the system calibration. Finally, an approach to time-domain waveform analysis of multi-tone signals which are closely spaced in frequency is introduced.

In Chapter 7, several examples of applications that highlight the most unique capabilities of the system described are reported. In particular an out-of-band linearity optimization of an HBT device, the characterization of a GaN device for high efficiency PA design, and some high power device measurements for base-station applications are described.

Finally, in Chapter 8 some conclusions are drawn, with recommendations for future work.

Chapter 2

Isothermal Measurement Systems

Isothermal measurement systems are typically used to evaluate the performance of microwave devices under non-continuous (pulsed-RF and pulsed-DC) operation. These measurements are essential when dealing with pulsed-RF applications like radar or burst-mode transmitters, or in semiconductor device characterization when dissipation problems need to be avoided. From a modelling point of view, isothermal characterization is indispensable in the development of device models which include self-heating and trapping effects. Currently, these advanced device models [17–20] receive high interest in literature since they provide a more accurate prediction for the linearity degradation of PA's due to memory effects. Typically, the extraction of the parameters for these models involves the characterization of the bias dependent small-signal parameters under pulsed-bias and pulsed-RF conditions. In general, activities such as database-oriented modelling strongly benefit from improvements in measurement accuracy and speed, when aiming for high-quality device data which is densely spaced versus bias. Over time, several implementations of isothermal setups have been reported [22–26], however, previously reported isothermal measurement setups only partly fulfill the above mentioned requirements since their core hardware was based on equipment, which was not fully optimized for the pulsed conditions used in isothermal measurements. This resulted in restrictions in pulse width, duty cycle, dynamic range and measurement speed.

In this chapter, the theory and the requirements for pulsed-RF and pulsed-DC measurements are discussed. Moreover, a new isothermal measurement approach with its hardware implementation is introduced, providing the ability to measure with DC and RF pulses as low as 200 ns, while featuring a high

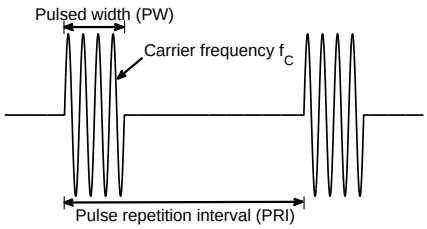

Figure 2.1: Pulsed-RF signal.

dynamic range under pulsed-RF conditions. The realized system performance is discussed in detail through a set of benchmarks, and some measurement examples on active devices are provided.

2.1 Pulsed measurements fundamentals

A pulsed-RF signal is a continuous wave (CW) signal with a certain frequency f_C, that is switched on and off at regular intervals. The pulse width (PW) is the time interval during which the signal is switched on, while the pulse repetition interval (PRI) is the time period at which the pulses are repeated (Fig. 2.1). The inverse of the PRI is the pulse repetition frequency (PRF) and the duty cycle is the amount of time the pulse is on, compared to the period of the pulses ($DutyCycle = PW/PRI$). To see what the frequency-domain spectrum of a pulsed signal looks like it is necessary to analyze the time-domain response mathematically [28]. A pulsed signal is generated by first creating a rectangular-windowed version of the signal with pulse width PW. A *shah* function, which is defined as a train of impulses equally spaced in time, is then realized with a period of $\frac{1}{PRF}$. The windowed version of the signal is then convolved with the *shah* function to generate a periodic pulse train in time corresponding to the pulsed signal (Fig. 2.2).

$$y(t) = [rect_{PW} \cdot x(t)] * shah\left[\frac{1}{PRF}(t)\right] \tag{2.1}$$

where,

$$shah\left[\frac{1}{PRF}(t)\right] = \sum_n \delta(t - n(\frac{1}{PRF})) \ . \tag{2.2}$$

The Fourier transform of the signal y(t) is,

$$Y(s) = [PW \cdot sinc(PW \cdot s) * X(s)] \cdot [PRF \cdot shah(PRF \cdot s)] \tag{2.3}$$

$$Y(s) = [PW \cdot sinc(PW \cdot s)] \cdot [PRF \cdot shah(PRF \cdot s)] \tag{2.4}$$

$$Y(s) = DutyCycle \cdot sinc(PW \cdot s) \cdot shah(PRF \cdot s)\ . \tag{2.5}$$

As shown in equation 2.5 the signal's spectrum in the frequency domain has a $\frac{\sin(x)}{x}$ envelope (Fig. 2.3). The width of the lobes are inversely related to the pulse width. This means that as the pulses get shorter in duration, the spectral energy is spread across a wider bandwidth. Furthermore, the spacing between the various spectral components is equal to the pulse repetition frequency.

In general two types of measurements can be distinguished when considering pulsed-RF characterization, based on the bandwidth of the IF filter and the timing circuits available in the network analyzer: wideband and narrowband detection [29].

Wideband detection can be used when the receiver is synchronized with the pulse stream, and only the "on state" of the pulse is acquired. In this case the majority of the pulsed-RF spectrum falls within the bandwidth of the receiver. This requires a pulse trigger that is synchronized to the pulse repetition frequency of the signal. The advantage of the wideband mode is that there is no loss in dynamic range when the pulses have a low duty cycle. The disadvantage of this technique is that when the pulse duration gets shorter, the bandwidth of the signal becomes larger and will eventually fall outside the bandwidth of the receiver. Consequently, to measure smaller pulse widths the bandwidth of the receiver, along with the bandwidth of the intermediate frequency (IF) filter, must increase, yielding a higher noise power, which reduces the dynamic range.

Narrowband detection is based on the continuous asynchronous sampling of the RF pulses, yielding a discrete, sinc-like frequency spectrum. With this technique, all of the pulse spectrum is removed by digital filtering except for the central frequency component, which represents the RF carrier. After filtering, the pulsed-RF signal appears as a sinusoid or CW signal. With

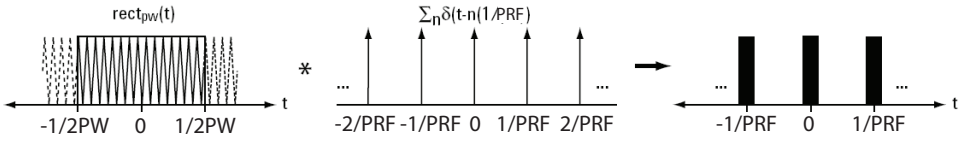

Figure 2.2: Mathematical representation of a pulsed-RF signal. Source Agilent Technologies [28].

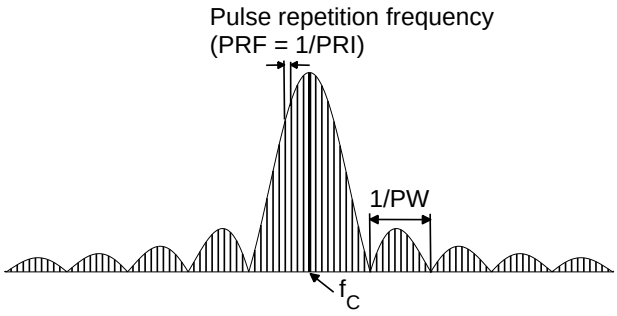

Figure 2.3: Frequency spectrum of the pulsed-RF signal of Fig. 2.2.

narrowband detection, the analyzer samples are not synchronized with the incoming pulses, therefore no trigger pulse is required. The advantage of this detection mode is that there is no lower pulse-width limit, since no matter how broad the pulse spectrum is, most of it is filtered away, leaving only the central spectral component. The disadvantage of narrowband detection is that measurement dynamic range decreases as the duty cycle increases. This phenomenon is also known as pulse desensitization and the degradation in dynamic range can be expressed as $20 \cdot \log(DutyCycle)$.

At the time of commencing this project two different network analyzer products from Agilent Technologies were available for performing pulsed-RF measurements: the 8510C (with pulsed option 008) and the PNA. The 8510C [30] uses the wideband detection technique. After a first superheterodyne down-conversion to 20 MHz, the pulsed signal is down-converted to baseband IQ pulses and then digitized (Fig. 2.4a). Each I and Q output has a bandwidth of 1.5 MHz, for a total bandwidth of 3 MHz, yielding pulses with 300 ns rise and fall times ($t_r/t_f = 1/BW$). Since the pulse width must be larger than several t_r/t_s in order for the detector to properly acuire the pulses, this results in a minimum specified measurable pulse width of 1 μs [29]. The down-conversion chain of the PNA network analyzer [29] is shown in Fig. 2.4b. After a first down-conversion to 8.33 MHz, the pulsed signal is down-converted again to an IF of 41.7 kHz. An anti-alias filter is placed just in front of the analog-to-digital converter. The PNA has the possibility to operate both with a wideband and narrowband detection technique. However, due to the low IF bandwidth of 35 kHz for the PNA and of 250 kHz for the PNA-L version, the minimum pulse durations that can be measured with the wideband technique are 50 μs and 10 μs respectively, therefore this mode is not suitable for performing

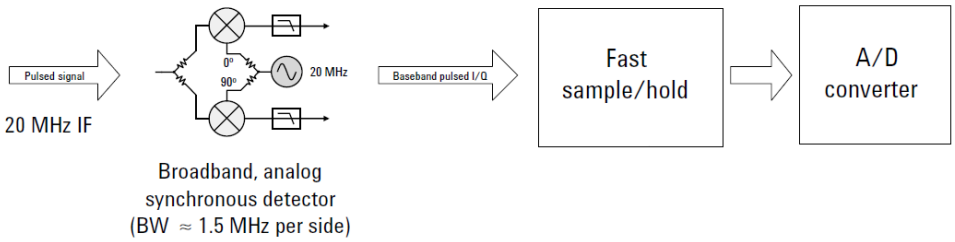

(a)

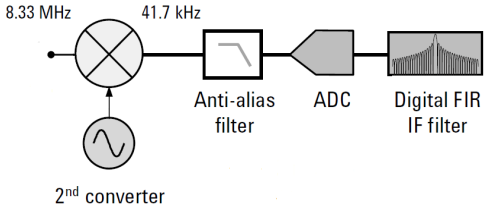

(b)

Figure 2.4: (a) 8510C down-conversion chain using the wideband detection technique. (b) PNA down-conversion chain. The PNA has the possibility to operate both with a wideband and narrowband detection technique. Source Agilent Technologies [28].

isothermal measurements. When using the narrowband technique, instead, digital filtering is used to select the RF carrier after the digital data acquisition. In this case, no trigger is used for synchronizing the pulse acquisition, therefore much lower pulse widths can be measured.

The dynamic range of the two different families of network analyzers [29] is depicted in Fig. 2.5. The 8510C network analyzer's dynamic range is constant versus duty cycle, thanks to the use of the wideband detection technique, however, it is limited to about 65 dB. For this reason, a high number of averages is required to reduce the noise floor and increase the dynamic range. This results in extremely long measurement times. Regarding the PNA, although this type of pulsed network analyzer has a very high dynamic range for high duty cycles (close to 100 dB at 10 % duty cycle) and it is extremely fast, its performance drastically decreases as the duty cycle gets lower (Fig. 2.5), becoming even worse than that of the 8510. This is a significant disadvantage in isothermal measurements where, depending on the device technology, the pulse width has to be as small as possible and the duty cycle very low in order to guarantee

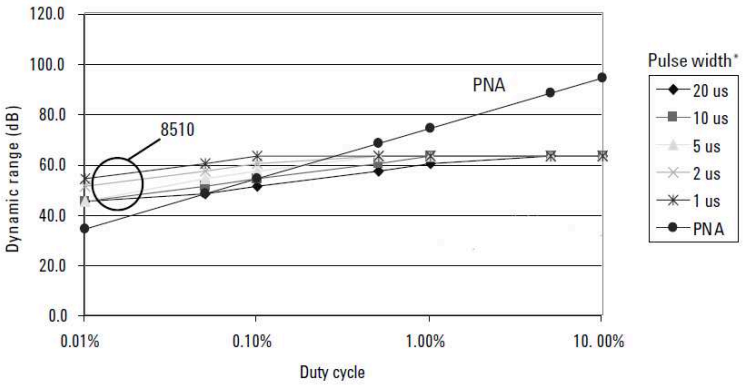

Figure 2.5: Dynamic range vs. duty cycle for different pulse widths for the Agilent 8510 and the PNA pulsed network analyzers [28].

that the device will remain isothermal. For example, a pulse width of 100 ns with a duty cycle of 0.1 % can be considered a satisfactory condition for most devices. However, at these settings the performance of current pulsed network analyzers is strongly reduced, as the dynamic range becomes lower than 60 dB, as shown in Fig. 2.5.

It is important to note that further developments to the PNA have improved the dynamic range of the new PNA-X for low duty cycles. In particular, for this instrument the pulse desensitization problem, although still present, it has now been reduced to a value of $10 \cdot \log(DutyCycle)$ [31], enabling the use of this instrument for isothermal measurements. These later developments, which occurred after this thesis work, are not discussed here.

2.2 System configuration

In the previous section, the basics of pulsed network analysis and the commercially-available solutions at the beginning of the project were discussed. When looking at the commercial instrumentation available for performing pulsed-RF measurements, a custom, dedicated solution for performing high-speed, high-dynamic range measurements is needed to tackle the isothermal modelling problem.

The hardware configuration of the proposed isothermal setup is given in Fig. 2.6. Since our application requires a dynamic range as high as possible even for low duty cycles, a wideband detection technique is employed for performing pulsed-RF measurements. The setup utilizes a PXI based data

acquisition system to implement the pulsed network analyzer, which provides high-dynamic range (see Section 2.3.1), independent of pulse width and duty cycle. Also the data acquisition needed for synchronized pulsed I-V measurements is implemented in the PXI platform, which ensures high data transfer rates of up to 78 MB/s and thus high measurement speed.

The pulsing of the DC biasing, the RF stimulus, as well as all the data acquisition is synchronized by two external Agilent 8110A pulse generators, each having two outputs, which trigger the two DC pulsers and the RF pulse generation. The user is free to choose the delay between the pulses. The RF pulse trigger is also used to synchronize the acquisition of all DC and RF waveforms. All the triggering, biasing and pulse generation have been realized using commercially-available hardware instrumentation only.

2.2.1 Pulsed VNA architecture

The improved pulsed vector network analyzer (VNA) has been realized by replacing the acquisition part of the HP 8510C [32] with a NI PXI-5105 12-bit A/D converter board, which features 60 MS/s sampling frequency. The new hardware configuration is controlled by custom-developed signal processing and filtering software.

An RF synthesizer with pulsed-RF capabilities generates the stimulus for the device under test (DUT), and the reflected, transmitted and reference signals are down-converted by the S-parameter test-set and subsequently acquired by the two external A/D converters. The HP 85110A H05 test-set is developed specifically for pulsed operation since it employs wideband frequency mixers to work with wideband IF detection, and covers a frequency range between 0.5 and 20 GHz. The synthesizers and the data acquisition cards are triggered by an external reference pulse generated by the Agilent 8110A pulse pattern generator. The synthesizers, along with the test-set, are controlled by a computer using the GPIB bus, while the A/D converters are controlled using the PXI standard.

Since the data acquisition and the signal generation are synchronized with an external trigger, only the "on part" of the RF pulse is acquired. The only filtering before the A/D converters is an anti-aliasing filter with a cut-off frequency of 24 MHz. Consequently, a wideband detection technique is employed. By choosing a high IF, thus avoiding the IQ down-conversion as used in the 8510C, and by making use of wideband digitizers, the traditional limitations on the minimum pulse width are removed, and as result our setup is only limited by the pulse generation capability of the synthesizers.

After the data acquisition a FFT is performed on the acquired waveform to extract the magnitude and phase information of the signal components

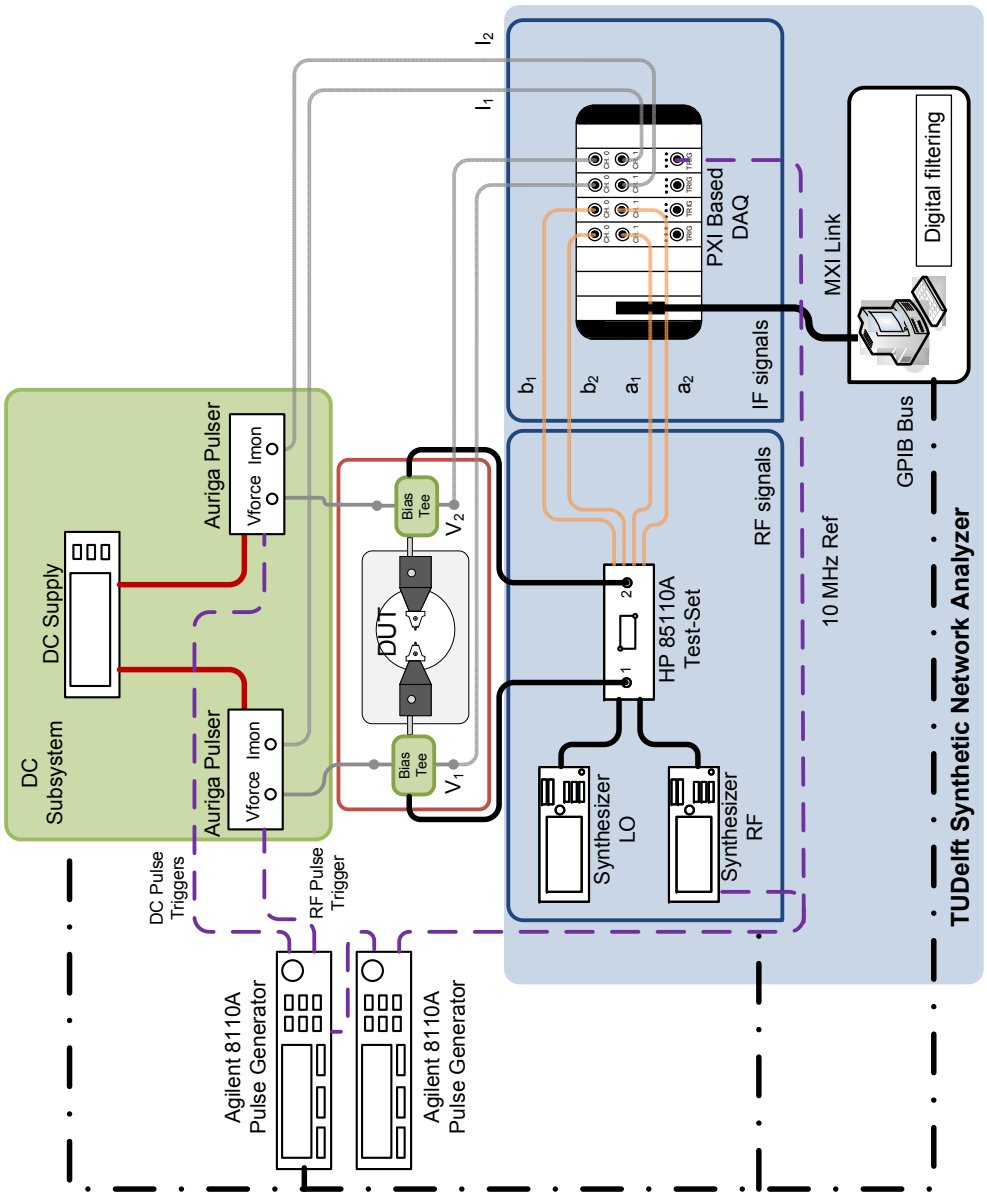

Figure 2.6: Block diagram of the custom pulsed RF - pulsed I-V setup.

at the frequency of interest. Finally, a ratio between two of the measured signals gives the S-parameter measurement. In order to ensure that the FFT algorithm works properly in a practical implementation, coherent sampling [33] has to be performed. This means that the FFT has to be applied on an integer number of periods of the down-converted RF signal to avoid spectral leakage. To establish this, the frequencies of the local oscillator (LO) and of the RF source are synchronized to produce an IF output of 12 MHz, which results in 5 samples per period due to the 60 MHz sampling frequency. This in principle facilitates a minimum pulse width of 83 ns. However, to allow for transients in the RF during the start of the trigger, we use a minimal pulse width of 100 ns.

Signal processing and dynamic range considerations

The dynamic range (DR) of an ADC is the ratio of the largest to the smallest signal that the converter can represent. The largest signal is usually taken to be a sine wave that covers the full voltage range of the ADC, while the smallest signal is usually taken to be the total noise level of the ADC. Consequently the dynamic range expressed in decibels (dB) is

$$DR = 20 \cdot \log\left(\frac{S}{R}\right) \ , \tag{2.6}$$

where S is the rms amplitude of the largest signal, and R is the rms amplitude of the smallest signal. In an ideal ADC, the noise is a direct result of the quantization noise of the ADC [34], therefore the dynamic range can be calculated directly from the number of bits N as

$$DR = 6.02 \cdot N + 1.76 \ . \tag{2.7}$$

In a real ADC, though, the presence of noise other than from quantization is responsible for a decrease in dynamic range. In our particular situation, the A/D converters employed are 60 MS/s NI PXI-5105 12-bit digitizers, and their theoretical dynamic range can be calculated from the number of bits and the input range. For an input range of 50 mV peak-to-peak, the maximum

power level that can be measured with a 50 Ω input impedance is

$$\begin{aligned} P_{max}(dBm) &= 10 \cdot \log\left[1000 \cdot \frac{(V\max_{RMS})^2}{50\ \Omega}\right] = \\ &= 10 \cdot \log\left[1000 \cdot \frac{(V\max_{Peak}/\sqrt{2})^2}{50\ \Omega}\right] = \\ &= 10 \cdot \log\left[1000 \cdot \frac{(25\ mV/\sqrt{2})^2}{50\ \Omega}\right] \approx -22\ dBm\ . \end{aligned} \tag{2.8}$$

The lowest power that can be measured due to the total noise of the digitizer as specified in the data sheet is

$$\begin{aligned} P_{min}(dBm) &= 10 \cdot \log\left[1000 \cdot \frac{(Vnoise_{RMS})^2}{50\ \Omega}\right] = \\ &= 10 \cdot \log\left[1000 \cdot \frac{(19\ \mu V)^2}{50\ \Omega}\right] \approx -81.4\ dBm\ , \end{aligned} \tag{2.9}$$

yielding a dynamic range of

$$DR = P\max(dBm) - P\min(dBm) \approx 59.4\ dB\ . \tag{2.10}$$

If we assume that the source of noise in our ADC appears as white noise, we can use digital filtering to filter out noise components outside the bandwidth of interest. In this case a correction factor, called process gain [34], must be added to equation 2.7 to account for the related increase in the signal-to-noise ratio,

$$DR = 6.02 \cdot N + 1.76 + 10\log\frac{f_S}{2 \cdot BW}\ . \tag{2.11}$$

The process of sampling a signal at a rate which is greater than twice the bandwidth is referred to as oversampling. Performing an M-point FFT over the acquired waveform to extract information about a particular frequency component, is equivalent to digitally filtering the signal with a bandwidth equal to the frequency resolution of the FFT, that is f_S/M. Therefore the dynamic range due to the discrete Fourier transform is

$$DR = 6.02 \cdot N + 1.76 + 10\log\frac{M}{2}\ . \tag{2.12}$$

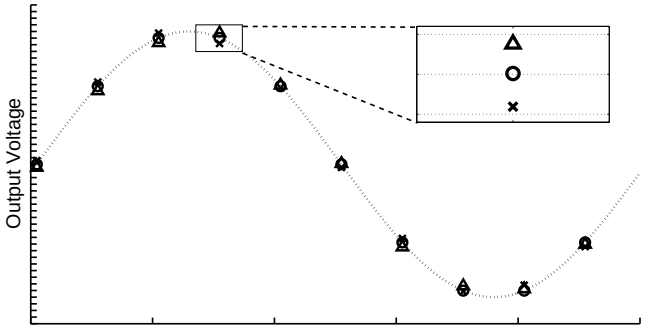

Figure 2.7: Time-domain averaging of different periods of a sine wave.

From equation 2.12 it's clear that to improve the dynamic range it is sufficient to acquire a higher number of samples. In particular, doubling the number of FFT points drops the magnitude of the asynchronous noise components by a factor of 2, or 3 dB on a log scale. This expected improvement drops off somewhat for large record lengths due to round-off errors in computing the FFT.

Time-domain averaging is another technique to improve dynamic range as it attenuates asynchronous noise sources by averaging time-domain waveforms from multiple triggers. Averaging in the time domain not only reduces the white noise present on the signal acquired, but also permits to increase the number of effective bits of the digitizer, and thus increases the dynamic range. This technique, often referred to as "oversampling and decimation" [35], can be achieved by oversampling the signal and then taking the average of the subsequent samples. For each additional bit of resolution, n, the signal must be oversampled four times,

$$f_{oversample} = 4^n \cdot f_{Niquist} \ . \tag{2.13}$$

To guarantee proper operation of this approach, the signal-component of interest should not vary during a conversion, however, there should be enough noise present over the input signal so that the results of successive acquisitions vary the least significant bits of the A/D converter. For our application, the signal to process is a sine wave. In this case it is also possible to apply the same concept by acquiring different periods of the sine wave and averaging the time samples relative to the same time reference, as depicted in Fig. 2.7. In particular, averaging 10 different acquired sine waves yields a 10 dB increase in the dynamic range.

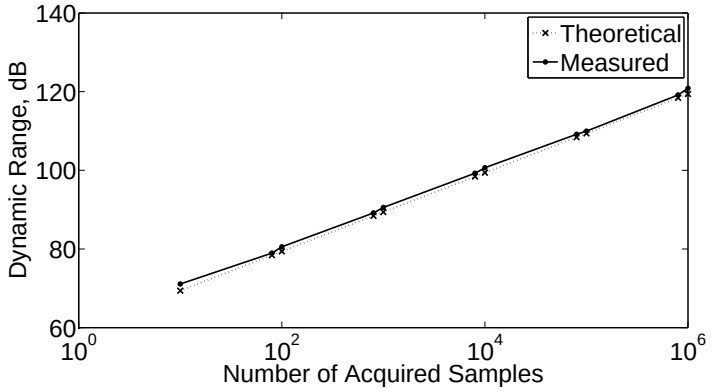

Figure 2.8: Measured vs. theoretical dynamic range, as calculated from equations 2.10 and 2.12, of the PXI-5105 A/D Converters.

A comparison between the theoretical dynamic range as calculated from equations 2.10 and 2.12 and the measured dynamic range of the PXI-5105 A/D converters is shown in Fig. 2.8. The dynamic range of the A/D converter is measured as the difference between the power of a full-scale sinusoidal signal and the noise floor of the converter. Note that this will be higher than the spurious-free dynamic range as this calculation does not take into account any spurious signals which are present within the A/D acquisition bandwidth. In fact the influence of spurs can be avoided by carefully selecting the IF. It is important to point out that this dynamic range analysis only takes into account the noise limitation of the receiver, and is useful only for understanding the techniques used to improve the dynamic range. The graph of Fig. 2.8, therefore, represents the best case scenario, as in reality the detected signal will contain a certain amount of noise by itself that reduces the effective dynamic range. The dynamic range of the pulsed VNA will be discussed further in Section 2.3.1.

2.2.2 Pulsed-DC measurements

The pulsed bias conditions to the DUT input and output are applied through the use of two Auriga AU4102 IV Pulsers, which switch the bias provided by an external Agilent 6629A power supply. To achieve the best pulse shape, parasitic loading was minimized in the setup by using very short cables and connecting the bias tees (Auriga AU0609) directly to the wafer probes. Within our system hardware configuration this combination can provide pulse widths as short as 200 ns. The maximum voltage and current ratings of the pulsers

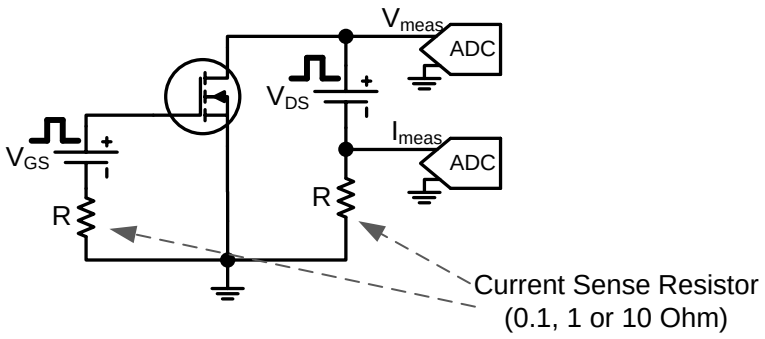

Figure 2.9: Current sense configuration with series resistor in the DUT ground path.

are 200 V and 10 A. The pulsed currents and voltages at the device ports are measured using 4 channels of the same PXI NI-5105 A/D converter board used for the RF measurements. Time-domain averaging is also used on the DC waveforms to increase the measurement accuracy.

Two different methods are available for sensing the current. The DC pulsers employed provide a current monitor port with an internal 0.1 Ω sense resistor to measure high currents. This resistor is inserted in the ground path going from the DUT ground to the negative port of the DC supply as illustrated in Fig. 2.9. To sense lower currents with high resolution, a 1 Ω or 10 Ω resistor can be placed in the external ground path just before the bias-tee. Before the actual measurement can take place, the sense resistor is calibrated by applying a range of voltages over a set of known resistors, while measuring the current. For the highest accuracy, the calibration resistors and voltages have to be selected according to the intended measurement range.

One advantage of using this method for sensing the current is certainly the high bandwidth, which will result in shorter transient times, allowing measurement of shorter pulses. On the other end, the sense resistor will cause a voltage drop at the device terminals. For this reason the voltage needs to be constantly monitored and iterations are necessary to reach the desired voltage at the DUT ports. Furthermore, due to the position of the sense resistor in the ground path, the source providing biasing to the pulser should have a floating ground with respect to the common ground of the measurement setup. Failing to do so would result in a parasitic current flow which is not directed through the current sense resistor, reducing the current measurement accuracy. The use of a completely floating source, like an Agilent 6629A, can solve this problem.

Another possibility to measure a pulsed current is to use a commercial clamp-on current probe. These types of probes employ a hybrid technology that uses a Hall sensor and an AC transformer to measure both DC as well as AC currents up to hundreds of MHz of bandwidth. These probes can measure currents up to tens of amperes and provide a relatively easy way to implement a current measurement since they do not require breaking the circuit and therefore cause no voltage drop. On the other hand, they can only measure down to current levels of a few milliamperes with good accuracy.

2.3 System performance

Device scaling of power devices through (compact) modelling techniques is quite often based on the characterization of relatively small device cells. In this process, isothermal device characterization is useful in simplifying the modelling problem, enhancing understanding and speeding up the modelling process. Consequently, an isothermal measurement system should be capable of measuring, with good accuracy, a wide range of pulsed voltages and currents to allow accurate characterization of different device sizes, from the single cell to the complete high-power device. At the same time, a high dynamic range for the S-parameter device characterization is of fundamental importance for two reasons:

- To guarantee accuracy, while ensuring truly small-signal device operation at low RF drive power levels.
- To accurately characterize a wide scope of device sizes / impedance levels.

In the following paragraphs, both the accuracy of the DC current measurement, as well as the RF measurement dynamic range of the proposed system are reported.

2.3.1 Pulsed VNA dynamic range

In order to illustrate the dynamic range performance of the realized pulsed network analyzer, several measurements on a bandpass filter were performed under different pulse conditions in the frequency range from 2.3 GHz to 4.5 GHz. A calibration was performed using a coaxial, 3.5 mm calibration kit. All of the measurements were made using an averaging factor of 1,024. Fig. 2.10a shows the measured S_{21} (in dB) for the pulse widths ranging from 100 ns to 100 μs with a fixed pulse repetition period of 1 ms. As can be seen, the dynamic

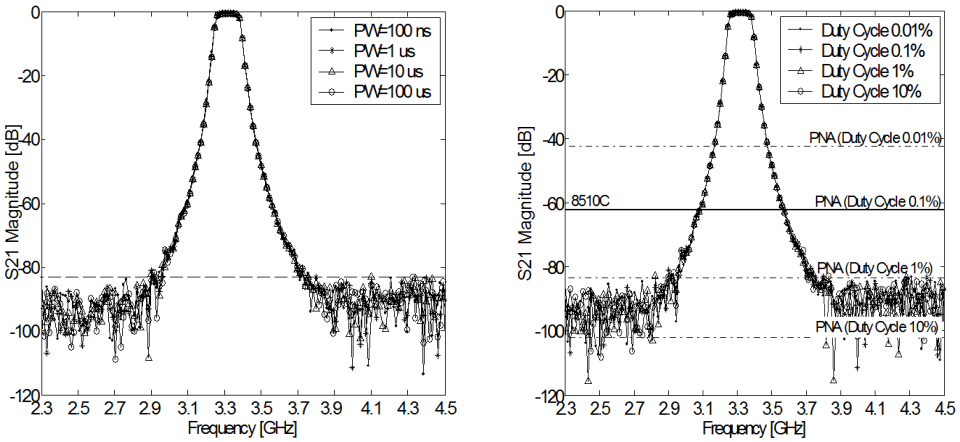

(a) (b)

Figure 2.10: (a) S_{21} (dB) of a band-pass filter for different pulse widths with a PRP of 1 ms, (b) S_{21} (dB) of a band-pass filter for different duty cycles with a PW of 1 μs.

range of the setup is more than 80 dB. The use of the wideband detection technique, which employs a trigger to synchronize the data acquisition, combined with digital processing of the acquired signal, ensures a wide dynamic range that is totally independent from the pulse width. Moreover, the high sampling rate of the A/D converters significantly reduces the constraints on the minimum pulse width, which can be as short as 100 ns. In Fig. 2.10b the results obtained for different duty cycle values, with a fixed pulse width of 1 μs, are presented. As expected, the duty cycle does not affect the dynamic range of the setup. Fig. 2.10 also shows a comparison between the dynamic range of the synthetic pulsed VNA with that of commercially-available instruments such as the HP 8510C and the Agilent PNA. It is clear that the new setup has a 20 dB improvement in dynamic range with respect to the 8510C. Also, for low duty cycles the new setup has a higher dynamic range than the PNA and the PNA-X.

2.3.2 DC measurement accuracy

To investigate the accuracy of our system, the isothermal setup was calibrated using various loading resistors ranging from 1 Ω to 2 $k\Omega$, while using three

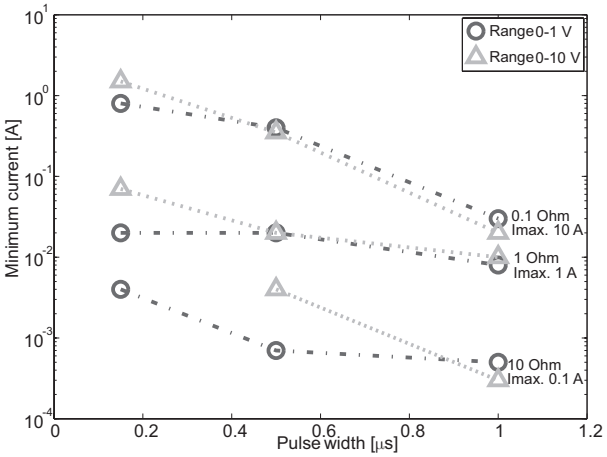

Figure 2.11: Minimum current vs. pulse width which can be measured with 1 % accuracy using the current sense resistors for the indicated current ranges (Imax). Due to ringing effects the current measurement accuracy is dependent on the voltage range (0-1 V) and (0-10 V) used in the calibration.

different current sense resistors (0.1, 1.0 and 10 Ω). After calibration, independent reference resistors, which were not included in the calibration, ranging from 5 Ω to 220 Ω are measured and the deviation of the measured value from their nominal resistance value is calculated to quantify the relative error in the current measurement. The loading and reference resistors were previously measured, in a temperature-controlled environment, by using a recently calibrated Agilent E5270B parameter analyzer, at small applied voltages to avoid thermal effects on the resistors. Since the accuracy of the parameter analyzer is higher than the A/D converter, the resistance values are accurately known. Note that the gain and offset errors of the current measurement are corrected by the current calibration. Therefore, the error calculated in such a way includes the inaccuracies of the A/D converters, the errors in the voltage setting and the ringing of the pulse for smaller pulse widths.

The minimum current that can be measured with 1 % accuracy is plotted as a function of pulse width for the different sense resistors in Fig. 2.11. In all the experiments the averaging in the data acquisition was kept constant at 1,024. From Fig. 2.11 it's possible to conclude that currents above 1 mA can be measured with an accuracy of 1 % on a resistive load, provided that the pulse width is at least 500 ns. It appears that the low-voltage range has a

slightly better accuracy for short pulse widths. This can be explained by the lower ringing of the bias pulse in the low voltage range. This effect disappears when the pulse width increases.

2.4 Measurements examples

One of the most common applications that requires pulsed-RF and DC conditions is the parameter extraction of active devices. To model an active device under small-signal conditions, the lumped parameters of the small-signal model must be extracted under isothermal conditions (afterwards the thermal node is extracted). In order to extract these values for different bias conditions, all four S-parameters must be measured at a fixed frequency at different base and collector voltages [36, 37].

In this section, we provide some measurement examples for different device technologies to highlight the capabilities of the realized measurement setup.

2.4.1 LDMOS devices

A GEN6 NXP LDMOS device [38] with a gate width of 2 mm has been measured and the cut-off frequency extracted from the pulsed S-parameter data (plotted in Fig. 2.12 as contours on the Id(Vds) plane).

At the input, a continuous voltage on the gate was applied, which was stepped from 1 V to 15 V (29 points), while at the output the pulsed voltage was changed from 0 V to 24 V (49 points). A current sense resistor of 1 Ω was used. The cut-off frequency of the device was extracted from the measured S-parameters at a frequency of 2 GHz. The DC pulse duration was varied from 0.2 to 150 μs, while the RF pulse was kept at 100 ns and the pulse period was fixed to 1 ms. The applied RF power within the pulse at the device input plane was set to -30 dBm to guarantee small-signal operation of the device under test.

The measurement data in Fig. 2.12 clearly demonstrates the expected behavior of the LDMOS device with respect to self-heating, namely the drain current reduction due to self-heating is nearly eliminated when using a very short pulse width. There are already some differences between the measurements at 1 μs and at 200 ns (both the f_T and I_{ds} go up). These results demonstrate that the realized measurement setup is able to measure power devices with very small pulse widths.

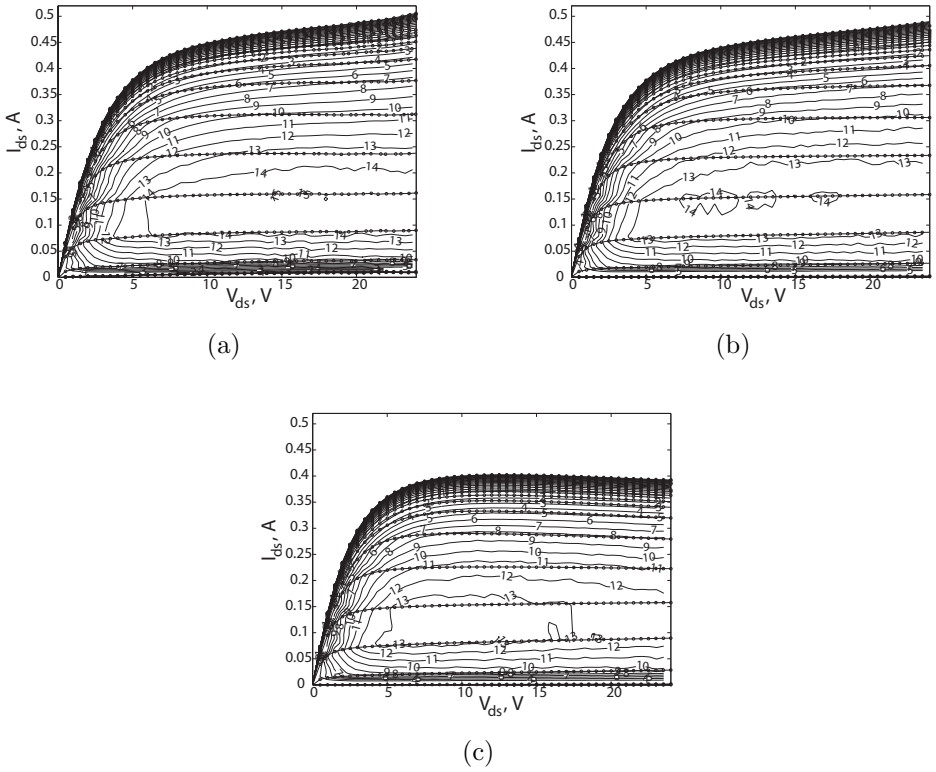

Figure 2.12: Measured contours of constant f_T(GHz) for a GEN6 NXP LDMOS device plotted in the $I_d(V_{ds})$ plane using (a) pulse width of 0.2 μs (pulse period = 1 ms), (b) pulse width of 1.0 μs (pulse period = 1 ms), (c) pulse width of 150 μs (pulse period = 1 ms).

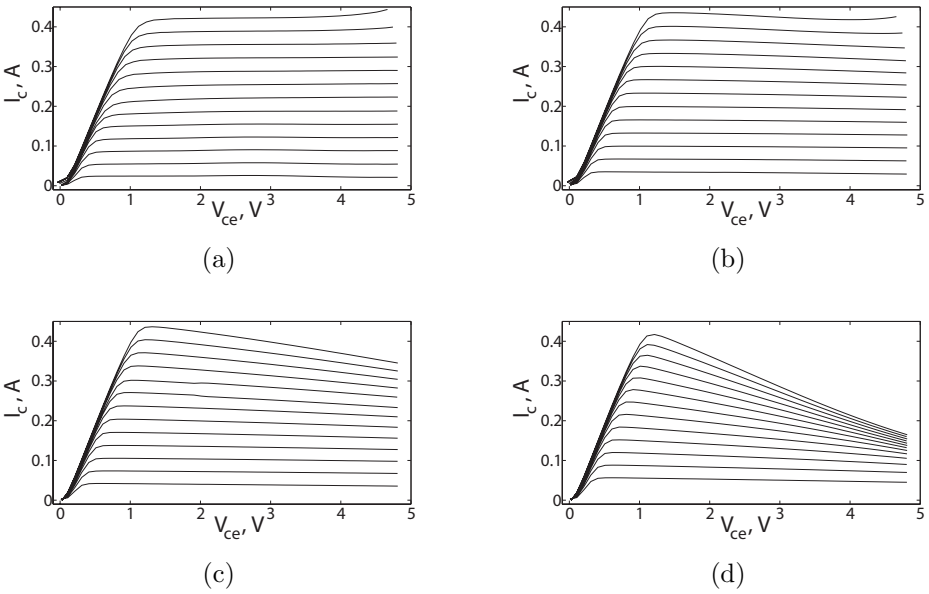

Figure 2.13: Measured output characteristic for a GaAs HBT device for a pulse width of (a) 300 ns, (b) 500 ns, (c) 1 μs, and (d) 5 μs, with a pulse period = 1 ms.

2.4.2 III-V HBT devices

A GaAs HBT device with 4 emitter fingers, 3.0 μm wide and 44 μm long has also been measured, using DC pulse durations of 0.3, 0.5, 1 and 5 μs, to highlight the capabilities of the setup for devices with higher thermal resistances. At the input, the current was stepped from 1 mA to 7 mA (25 points), while at the output the voltage was pulsed from 0 V to 4.8 V (49 points). Figure 2.13a-d show the measured output characteristics of the device for different pulse durations. This device exhibits a negative dependence of the current gain with temperature. The results clearly show the reduction of self-heating effects in the device with the pulse width.

2.4.3 SiGe HBT devices

The measurement of the I-V characteristics of a QUBiC4plus SiGe bipolar transistor [39] with an area of 99 μm^2 has been performed using DC pulse durations of 0.5, 1 and 3 μs. In this example, both the base-emitter and

collector-emitter voltages are pulsed with a pulse repetition period of 1 ms, from 0.77 to 0.91 V (0.01 V steps) and from 0.1 to 4.7 V (0.1 V steps), respectively. The results, which are shown in Fig. 2.14, clearly show increased self-heating effects, which eventually result in thermal runaway [40] at higher currents and longer pulse widths.

To conclude, a measurement under pulsed-bias, pulsed-RF conditions is reported for a pulse width of 1 μs and a pulse repetition period of 1 ms. The base-emitter and collector-emitter voltages are pulsed from 0.7 to 0.9 V (0.02 V steps) and from 0 to 3.5 V (0.1 V steps), respectively. The base-collector capacitance and the cut-off frequency of the transistor are then extracted from the pulsed S-parameter measurements, and are shown in Fig. 2.15.

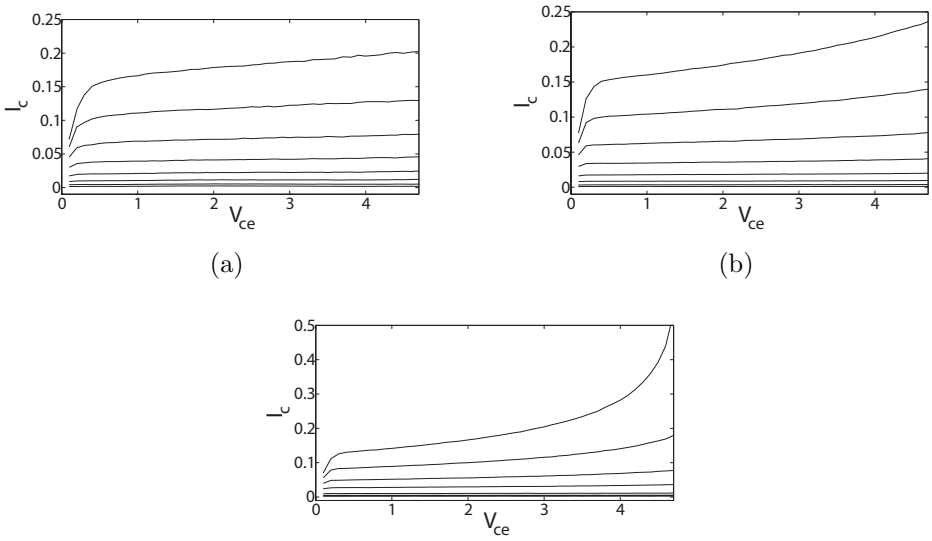

Figure 2.14: Measured output characteristic for a QUBiC4plus SiGe HBT device for a pulse width of (a) 500 ns, (b) 1 μs, and (c) 3 μs, with a pulse period = 1 ms.

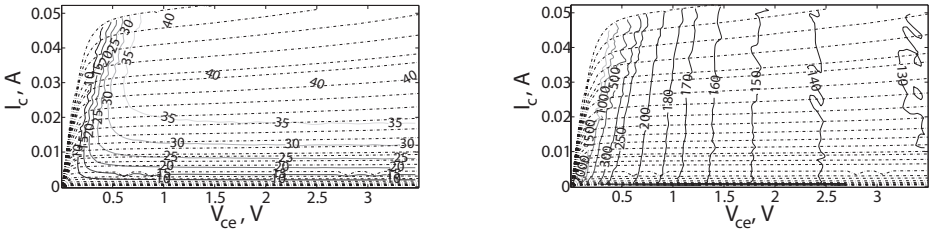

(a) (b)

Figure 2.15: Measured contours of (a) constant f_T(GHz) and (b) constant C_{bc}(fF) for a QUBiC4plus SiGe HBT device plotted in the Ic(Vce) plane using a pulse width of 1 μs (pulse period = 1 ms).

2.5 Conclusions

A new, low-cost, very flexible isothermal measurement setup has been proposed which facilitates fast and accurate isothermal device characterization. Measurements of different types of active devices have been performed, showing that the setup is capable of measuring pulses as short as 200 ns for a wide range of bias and power conditions, with good accuracy and measurement speed.

The system is based on a custom pulsed network analyzer that achieves a significantly higher dynamic range and measurement speed than currently available commercial solutions for isothermal measurements, when a low duty cycle is required. Moreover, the new setup does not suffer from the pulse desensitization issue typical of a narrowband detection technique, allowing the measurement of RF pulse widths down to 100 ns without any degradation in the dynamic range, facilitating true isothermal measurements conditions.

Chapter 3

Source and Load-pull Architectures

When designing an RF / microwave amplifier, it is important to properly integrate the transistor with the rest of the circuit. It is simply not enough to place the transistor in the circuit and expect it to perform optimally, since the input and output impedances of the transistor deviate strongly from the characteristic system impedance (typically 50 Ω). Improper integration of the transistor in the system degrades gain, output power and efficiency, among other considerations. In order to maximize these parameters, it is essential to use matching networks at the input and output of the device. Assuming an unconditionally stable device in a linear system, using the complex conjugate of the small-signal input impedance as the source matching network, and the complex conjugate of the small-signal output impedance as the load matching network is sufficient [37]. Unfortunately, this is only applicable to small-signal systems, and is of no assistance to the designers of power amplifiers, where the device is driven into large-signal operation [15]. In these situations, the technique used to determine the ideal matching impedances is referred to as load-pull [15].

The goal of load-pull is to measure the response of a device as function of the source and load impedances, input power, bias, temperature and other relevant parameters. Simply stated, a load-pull system presents a set of controlled impedances to the device under test (DUT), while measuring a list of performance parameters at each impedance point. By varying the impedance offered to the DUT, we can characterize the performance of the device and select the best set of impedance settings for optimum large-signal operation.

Harmonic load-pull is an extension of basic fundamental load-pull, where the loads presented to the DUT at multiple frequencies must be considered

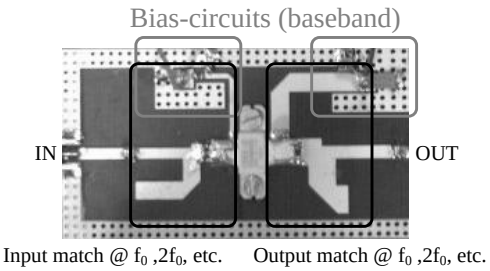

(a)

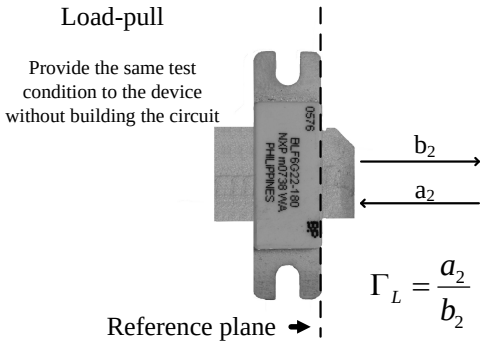

(b)

Figure 3.1: (a) Typical microwave power amplifier, including matching networks, using a packaged power transistor. (b) The physical matching network is emulated by controlling the ratio between a_2 and b_2 power waves. Load-pull techniques provide the same matching conditions to the active device without the need for building a physical matching circuit.

simultaneously. Each parameter is then measured at various combinations of load impedance for fundamental and harmonic frequencies. Harmonic load-pull is often used as a method to increase efficiency [15], or to improve the amplifier linearity when operating with modulated signals [41].

The actual load impedance (Z_L) presented to the DUT in the microwave domain is represented by the reflection coefficient related to this load, namely Γ_L. It represents the ratio between the reflected wave from the load (a_2) and the forward traveling wave (b_2). The generalized formula for Γ_L at all

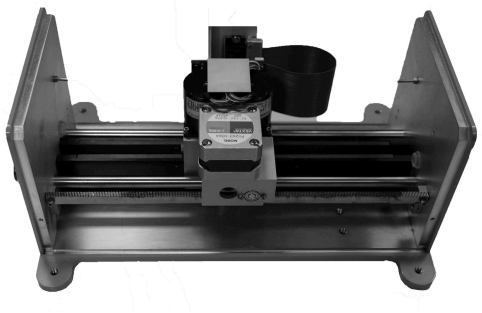

Figure 3.2: A conventional passive tuner, with moving probe and slab line.

frequency components of interest can be written as,

$$\Gamma_{L,n}(f_x) = \frac{a_{2,n}(f_x)}{b_{2,n}(f_x)} \ , \tag{3.1}$$

in which $a_{2,n}$ is the wave reflected from the load, $b_{2,n}$ is the forward traveling wave, n the harmonic index and f_x a frequency in the band of interest. This notation allows us to describe all the relevant circuit properties of the output matching network and of the bias circuitry (Fig. 3.1a), while we can use a similar formalism for the input matching. In a source or load-pull measurement we control the reflection coefficients offered to the active device in an artificial way and imitate the complete circuit without actually building it (Fig. 3.1b). This yields major advantages in reducing the development time of new transistor technologies and their application in power amplifiers, while providing a significantly better understanding of the behavior of the active device.

In the following sections the traditional load-pull architectures, along with their strengths and weaknesses, will be described in detail.

3.1 Passive load-pull

Passive mechanical tuners [42, 43] (e.g., see Fig. 3.2), make use of sliding mechanical probes (or "slugs") to create a reflection, by interrupting the electric field of an airline. The probe is inserted into the airline at variable depth; the further the probe penetrates into the airline and interrupts the electric field, the greater the magnitude of reflection. The phase of this reflection is varied by sliding the probe along the length of the slab line. Therefore, any impedance inside the Smith chart can be presented to the DUT by selecting the appropriate vertical and horizontal positions of the probe with respect to

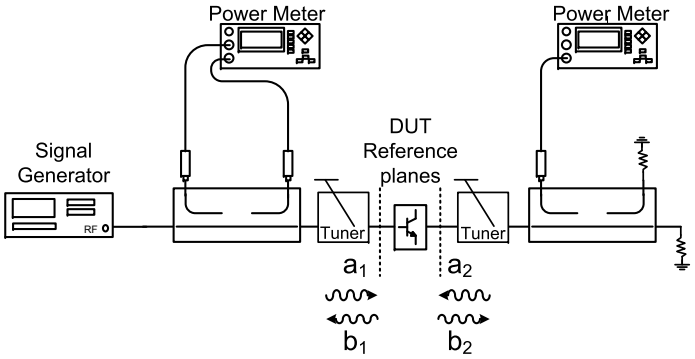

(a)

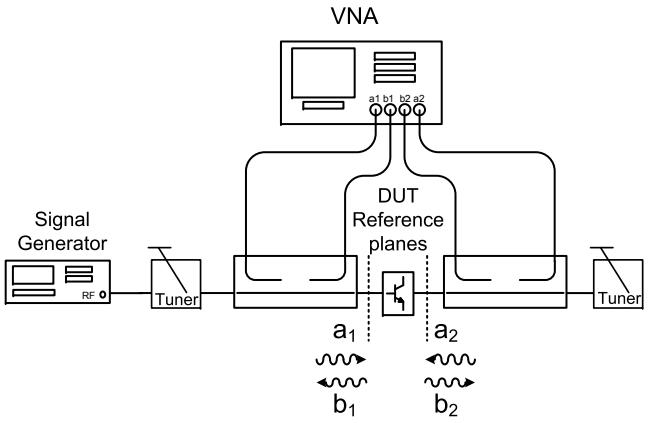

(b)

Figure 3.3: (a) Traditional tuner based load-pull measurement system. The tuners are placed between the DUT and the couplers. Power meters are commonly used to measure available, incident and output power. (b) Real-time system configuration where the couplers are placed between the tuners and the DUT. In this configuration a VNA can be used to measure all the scalar and vector quantities of the DUT.

the airline. Fundamental load-pull is typically achieved by using a single tuning probe. Harmonic load-pull is achieved using a combination of two, three or more probes in either cascaded or filtered configurations.

Tuner based systems are the preferred industry large-signal test bench choice today, due to their simplicity and high power handling capabilities (up to 500 W of power in CW). However, passive tuners are slow because of the time the probe takes to move from one position to another when changing reflection coefficient. More importantly, they are constrained by losses which limit the magnitude of the reflection coefficients that these systems can provide to the DUT. It is clear that the wave a_2, which returns to the DUT from the load tuner, will always be lower than b_2 due to tuner losses. Also the losses between the DUT and the tuner lower the amount of energy that can be reflected. Typical values range between $\Gamma_L = 0.8$ and $\Gamma_L = 0.92$ at the device reference plane.

For this reason, passive tuners are often placed as close as possible to the DUT, that is, before the reflectometers used to couple the a_1, b_1, a_2 and b_2 waves (Fig. 3.3a). In this case, to measure all the corrected scalar (P_{OUT}, P_{IN}, $Gain$, etc.) and vector (Γ_{IN}, Γ_S, Γ_L, etc.) quantities of the DUT, the two-port S-parameters of each tuner must be measured for each tuner position during a time consuming pre-characterization phase. The accuracy of the load-pull measurements will then rely on the tuner and connector repeatability. Alternatively, very low-loss RF couplers [44, 45] can be employed to reduce the losses and allow the use of a traditional two-port network analyzer system architecture (Fig. 3.3b). This configuration, typically referred to in literature as "real-time" load-pull, has all the advantages of high-speed, high-accuracy and fast calibration which are typical of a two-port network analyzer.

3.2 Active load-pull

Active load-pull systems can, thanks to the use of amplifiers, overcome the reflection magnitude restrictions due to losses. A close examination of equation 3.1 reveals that any arbitrary load reflection coefficient can be created by injecting an a_2 wave into the output port of the DUT. In an active load-pull system, the magnitude restrictions due to losses are overcome by magnifying a_2 through the use of amplifiers. In this case the injected a_2 wave can become equal or bigger than b_2, so that Γ_L can even exceed unity at the DUT reference plane.

There are several advantages to an active system over traditional mechanical load-pull, including gamma control and ease of integration. Since there are no mechanical moving parts, and the system relies on electrical tuning, the

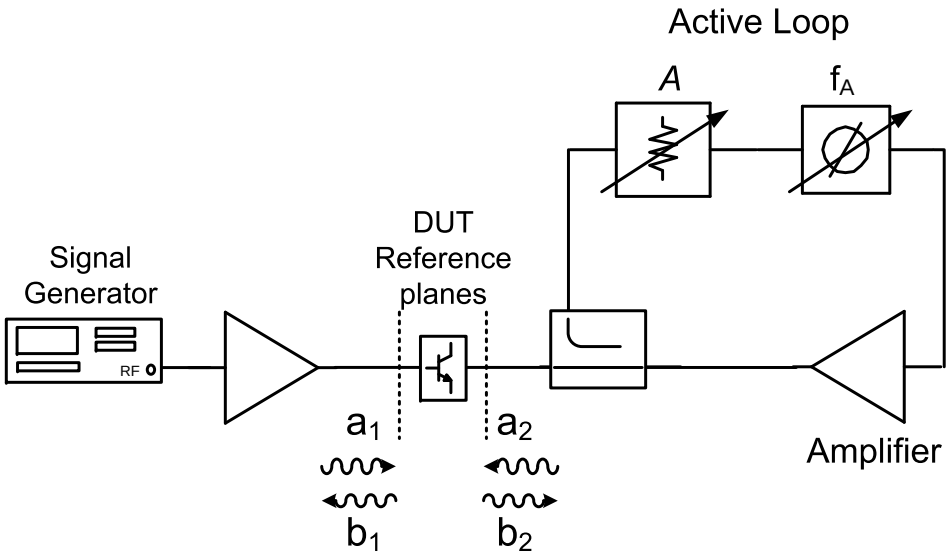

Figure 3.4: Closed-loop active load-pull configuration.

tuning itself can be fast. Harmonic load-pull, or tuning impedances at multiple frequencies simultaneously, becomes simple when using active load-pull techniques. A frequency multiplexer can be used to merge multiple active tuning paths, one per frequency, such that equation 3.1 is satisfied. Any losses inherent in the use of frequency multiplexers are easily overcome by the amplifiers added in each active tuning chain.

Over time, two basic concepts for active load-pull have been promoted, which we briefly discuss below.

3.2.1 Closed-loop active load-pull

Closed-loop active load-pull has been referenced in IEEE publications since the early 1980's [46]. In a "closed-loop" or "feedback" system, an amplified version of b_2 is used as the reflected signal, a_2. To accomplish this, a coupler or circulator is used to direct the signal from the DUT, b_2, through a variable amplification stage with control of both magnitude and phase, and re-inject the signal as a_2 back into the device. A block diagram showing a typical closed-loop system is shown in Fig. 3.4.

Since there are no moving parts and the system relies on electrical tuning, speed is a major advantage of this technique. In fact the injected signal is a direct function of the coupled wave, thus the loop gain and phase shift determine the reflection coefficient, independent of the power and spectral

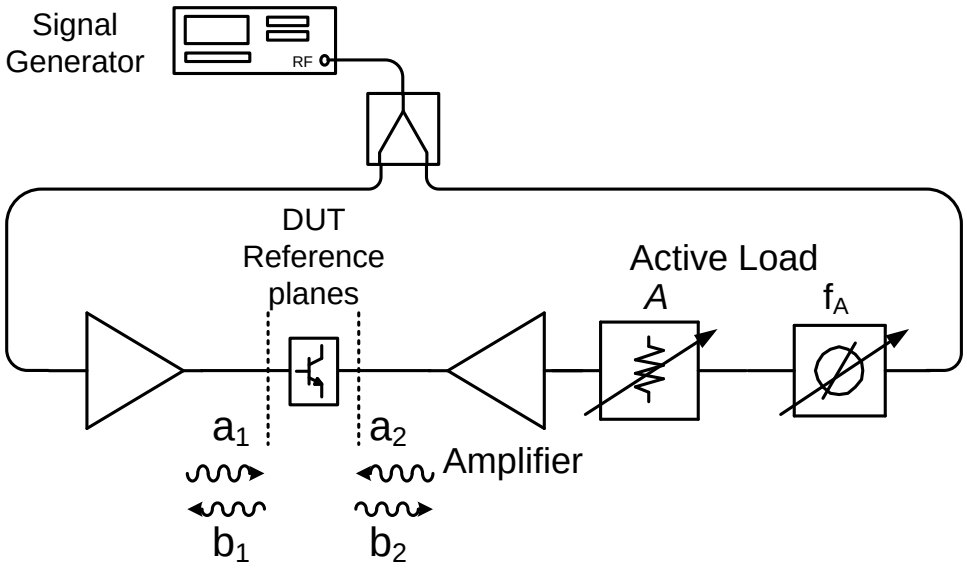

Figure 3.5: Open-loop active load-pull configuration.

content of the signal. This makes the closed-loop concept suitable for fast device characterization. On the other hand the use of a feedback topology can cause loop oscillations [47] when the forward gain of the feedback loop is bigger than unity, or if $|\Gamma_L| \cdot |\Gamma_{DUT}| > 1$ at any frequency. This is more likely to occur when employing wideband loop amplifiers. To avoid the risk of oscillation, most closed-loop systems include sophisticated filtering [48]. For this purpose, a recent publication proposes to control the reflection coefficient at baseband frequencies [49], where it is possible to implement better frequency selectivity.

A further disadvantage of this technique is that high-power and very linear injection amplifiers are needed in order to maintain the loop linearity, which can increase the overall system cost tremendously.

3.2.2 Open-loop active load-pull

The first appearance of active load-pull systems that can be found in the literature is by Takayama from the year 1976 [50]. In this topology, a part of the input signal to the DUT is split, adjusted in amplitude and phase, and injected into the output of the DUT to create a virtual load reflection coefficient (Fig. 3.5). This technique, commonly known in literature as “open-loop”, “two signal paths type” or “feedforward” load-pull, has been implemented, with several modifications over time, by many authors [51–55].

The basic active tuning chain consists of a signal source, a variable phase shifter and a variable gain stage. More advanced versions include in-phase / quadrature (IQ) modulators to control the amplitude and phase of the injected (a_2) wave [54]. Since the a_2 wave injected into the output of the DUT is no longer a direct function of b_2, the reflection coefficients realized are power and phase dependent. Therefore, iterations are needed during the measurements to find the optimal injection signals to offer the desired reflection coefficients to the DUT. This makes open-loop systems slower than the closed-loop ones. On the other hand, there is no feedback path and therefore no chance of tuning-loop oscillation compared to the closed-loop technique. Open-loop load-pull also requires high-power amplifiers to achieve the desired reflection coefficients when testing a high-power device. However, these amplifiers do not have to be linear, since the user specified reflection coefficient is reached by successive software iterations.

Furthermore, when extending the single-tone principle to wideband signals, determining the required content of the injection signals, at both the fundamental and harmonic frequencies, becomes difficult. To tackle the problem, the use of multipliers in the signal path has been proposed [55]. However, intermodulation distortion and memory effects will be present in practice, making it impractical to obtain the required injection signals by a separate analog multiplication process.

3.3 Electrical delay in load-pull systems

The introduction of wideband modulated signals as currently used in modern communication systems, poses a serious problem for the traditional load-pull system. Wideband signals are by definition not fixed to a discrete frequency, rather they have some bandwidth, ranging from several MHz to tens of MHz [56].

When working with modulated signals, the reflection coefficients offered to the DUT should ideally be constant (not vary versus frequency) within the modulation bandwidth at the fundamental, for well-controlled linearity behavior of the DUT, as well as in all related frequency bands at baseband and harmonic frequencies [41, 57]. This situation is approximated in real circuit implementations, when the matching networks are placed directly at the reference planes of the active device. In any conventional load-pull setup, however, the actual physical impedance is always located at some distance from the DUT (Fig. 3.6a), which is much larger than for any practical matching network. This distance, as well as any physical length within the tuning element itself (e.g., the length of the active feedback loop, or the position of the

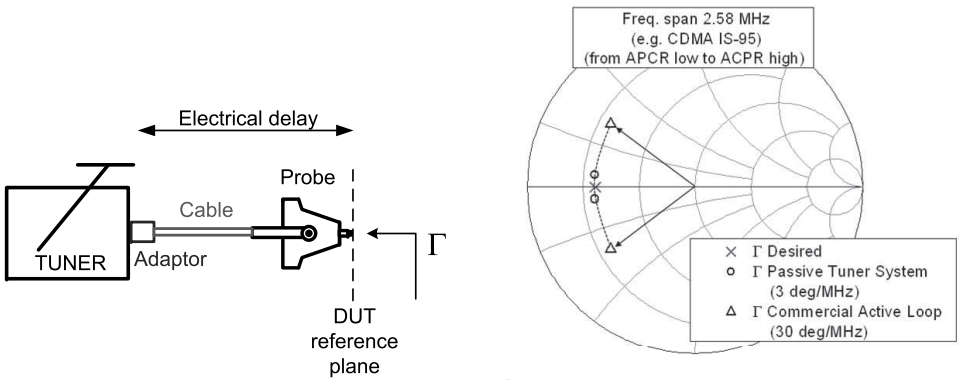

(a) (b)

Figure 3.6: (a) Phase delay caused by electrical lengths of the tuning element plus cables, adapters and probe (b) Phase rotation of the reflection coefficient for a 2.58 MHz wideband signal for a typical load-pull system.

probe in mechanical tuners), yields very large electrical delays, causing rapid phase changes of the reflection coefficients versus frequency. Typical values for these phase fluctuations start from about 3°/MHz for a fundamental passive mechanical tuner. If high-Q resonators or impedance tuners are used to control the harmonic terminations, the phase change with frequency is even greater. When considering active systems, the phase rotation can reach values of 30°/MHz or more for conventional closed-loop systems (Fig. 3.6b). Note that for a W-CDMA signal with adjacent and alternate channels (total bandwidth of 25 MHz), the reflection coefficient offered by a passive tuner based on these values would vary 75° in phase over this bandwidth, while in a conventional active closed-loop the phase change of the offered reflection coefficient would amount to 750°.

It is clear that these large phase deviations represent non-realistic circuit conditions, and will cause measurement errors such as IM_3 asymmetry, spectral re-growth, PAE and EVM degradation [58]. In general, maintaining the reflections coefficients constant over frequency is more and more difficult with the increasing modulation bandwidth of communication signals used in practical circuits and in load-pull measurement setups.

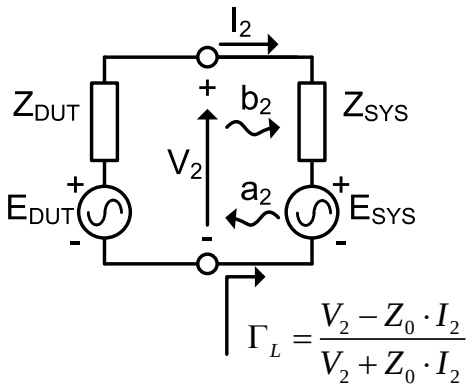

Figure 3.7: Thévenin equivalent schematic of an active load-pull configuration. The load impedance offered to the DUT at the reference plane is varied by adjusting the equivalent voltage source E_{SYS} in amplitude and phase. The related power needed to synthesize specific impedances depends strongly on the equivalent system impedance (Z_{SYS}).

3.4 Injection power and load amplifier linearity

As mentioned in Section 3.2 with respect to active load-pull configurations, it is necessary to inject a certain amount of power into the DUT to synthesize a specific Γ_L at the DUT reference plane. To better analyze the problem, the active load-pull topologies of Fig. 3.4 and of Fig. 3.5 can be described with their Thévenin equivalent as depicted in Fig. 3.7. E_{DUT} and Z_{DUT} and E_{SYS} and Z_{SYS} are the equivalent voltage sources and output impedances of the DUT and of the measurement system, respectively. The equivalent voltage sources can be expressed in terms of the transmitted and incident waves to the DUT as,

$$E_{DUT} = \frac{b_{DUT} \cdot (Z_{DUT} + Z_0)}{\sqrt{Z_0}} \qquad b_{DUT} = \sqrt{2 \cdot P_{b_2} \cdot (1 - |\Gamma_{DUT}|^2)} \tag{3.2}$$

$$E_{SYS} = \frac{b_{SYS} \cdot (Z_{SYS} + Z_0)}{\sqrt{Z_0}} \qquad b_{SYS} = \sqrt{2 \cdot P_{a_2} \cdot (1 - |\Gamma_{SYS}|^2)}\ . \tag{3.3}$$

With reference to the schematic of Fig. 3.7, the injected power required to achieve a certain Γ_L, or in other words a certain impedance $Z_L = V_2/I_2$

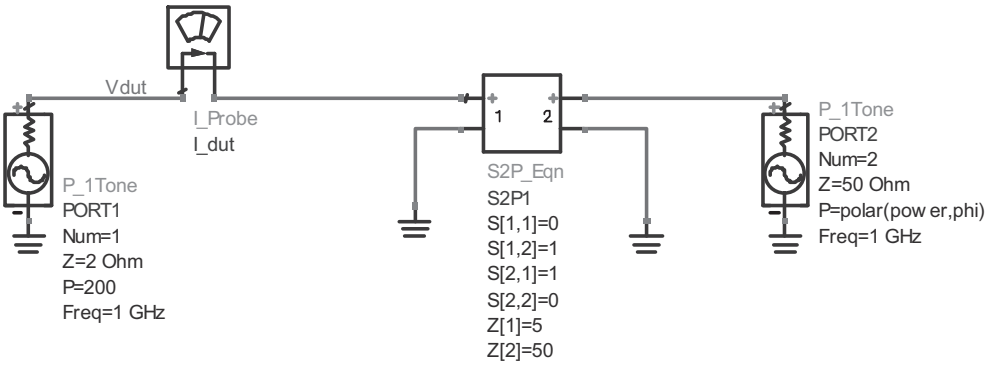

Figure 3.8: ADS$^{\mathrm{TM}}$ schematic testbench for the evaluation of the required injected power by active load-pull.

can be calculated as,

$$P_{a_2} = P_{b_2} \cdot \frac{(1 - |\Gamma_{DUT}|^2)}{(1 - |\Gamma_{SYS}|^2)} \cdot \frac{|Z_{DUT} + Z_0|^2}{|Z_{SYS} + Z_0|^2} \cdot \frac{|Z_L - Z_{SYS}|^2}{|Z_{DUT} + Z_L|^2} \tag{3.4}$$

It is clear from equation (3.4) that the injected power needed not only depends on the output power of the DUT and the desired Γ_L, but also on the output impedance of the device. When considering high-power devices, with output impedances in the order of a few ohms, the required injection power to cover the desired area of the Smith chart can be extremely high in a 50 Ω system (e.g., 2 to 10 times higher than the maximum output power of the DUT). To overcome this problem, pre-matching is typically used, which converts the 50 Ω impedance of the system to a value that is much closer to the output impedance of the DUT. This widely-used technique (also applied in passive load-pull) not only reduces the losses, but also lowers the power requirements of the load-injection amplifier [59]. As an example, consider a DUT with an output impedance of 2 Ω and an available output power of 200 W. To synthesize a load impedance of 1 Ω in a 50 Ω system, the required injection power would be more than 2 kW. Reducing the system impedance to 10 Ω with a lossless pre-match fixture lowers the required injection power for the same load condition to 360 W, while with a pre-match to 5 Ω the required injection power is only 142.2 W.

To provide a better understanding of the problem, a simulation using Agilent's Advanced Design Simulator (ADS), was performed using the simple schematic testbench illustrated in Fig. 3.8. The power source at port 1 represents a DUT with 200 W of output power and an output impedance of 2 Ω, while the power source at port 2 represents the injection amplifier in a 50 Ω

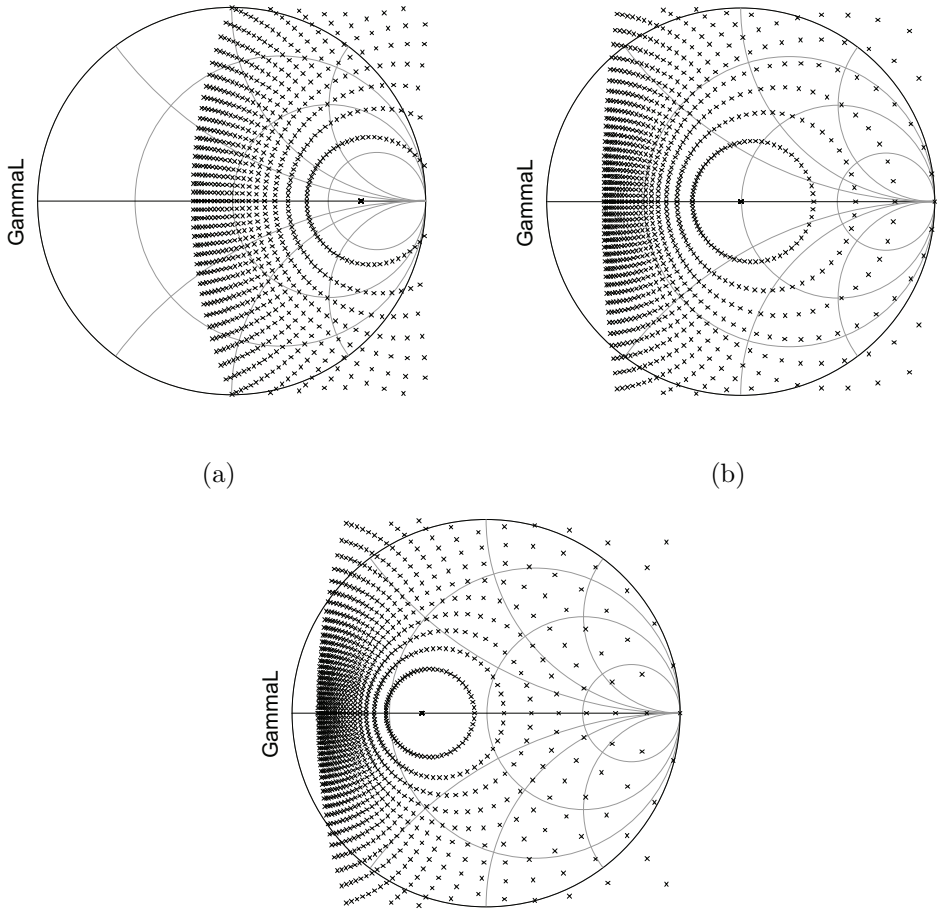

(a) (b)

(c)

Figure 3.9: Γ_L at the DUT reference plane in a Smith chart normalized to 10 Ω for a DUT delivering 200 W of output power and with an output impedance of 2 Ω. The injected power is swept from 0 to 200 W, and the Γ_L is plotted for: (a) no impedance transformation, (b) an impedance transformation to 10 Ω and (c) an impedance transformation to 5 Ω.

system. An impedance transformation from the 50 Ω system impedance to a lower impedance is implemented by using an ideal two-port S-parameter equation block. The injected power is swept from 0 to 200 W, with a phase sweep from 0 to 360 degrees. The results of the simulation are shown in Fig. 3.9, where the Γ_L that can be achieved at the DUT reference plane is shown on a Smith chart normalized to 10 Ω for three different cases: with no pre-match and with an impedance transformation to 10 Ω and to 5 Ω. From Fig. 3.9, it is clear that the Smith chart coverages benefits greatly from the use of a pre-matching circuit.

When considering multi-tone or modulated signals, the situation becomes more complicated as the linearity of the injection amplifier needs to be taken into account [41]. To study the linearity constraints on the injection amplifier we can consider a two-tone test signal. The power injected by the load amplifier at the third-order intermodulation frequency products of the two-tone test signal is given by,

$$\begin{aligned} P_{a_2,IM_3}\rfloor_{dBm} &= 3 \cdot P_{a_2,fund}\rfloor_{dBm} - 2 \cdot IP_{3,a_2} = \\ &= 30 \cdot \log \left[P_{b_2,fund}\rfloor_{mW} \cdot \frac{(1-|\Gamma_{DUT}|^2)}{(1-|\Gamma_{SYS}|^2)} \cdot \right. \\ &\cdot \left. \frac{|Z_{DUT}+Z_0|^2}{|Z_{SYS}+Z_0|^2} \cdot \frac{|Z_L - Z_{SYS}|^2}{|Z_{DUT}+Z_L|^2} \right] + \\ &- 2 \cdot IP_{3,a_2} \ , \end{aligned} \tag{3.5}$$

where $P_{b_2,fund}$ is the available power coming from the DUT at the fundamental tones, and $P_{a_2,fund}$ and IP_{3,a_2} are the power injected by the load amplifier at the fundamental tones and its output third-order intercept point, respectively.

Another harmonic balance simulation with Agilent ADS is performed using the simple schematic illustrated in Fig. 3.10. In this schematic, an amplifier component based on a polynomial model is used to simulate the DUT and the injection amplifier linearity. The same DUT is used as for the single-tone considerations, with a maximum output power of 200 W and an output impedance of 2 Ω. The output third-order intercept (OIP_3) is set in this simulation to 63 dBm. For this device, the output power is set equal to 50 W per tone in order to achieve the same peak voltage as in the single-tone case. These conditions yield an actual third-order intermodulation (IM_3) of the DUT of -30.35 dBc.

The results of the simulation are shown in Fig. 3.11, where the apparent IM_3 of the DUT is plotted as a function of the decreasing OIP_3 of the injection

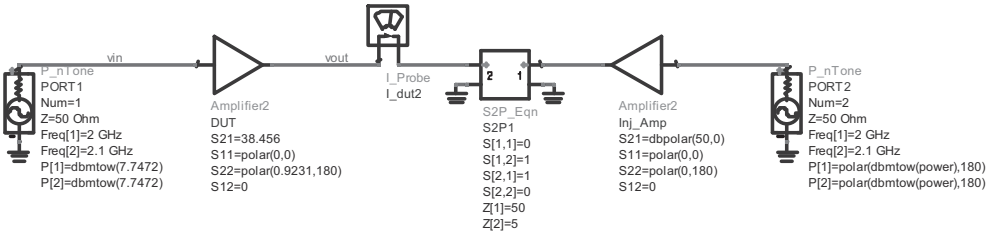

Figure 3.10: ADS^{TM} schematic testbench for the evaluation of the required injection amplifier linearity by active load-pull.

amplifier for different pre-matching conditions of the system impedance. The dotted line is the actual IM_3 level as would be achieved with a passive circuit. The dot-dash line represents the IM_3 level due to the P_{a2,IM_3} as approximated by equation 3.5. From Fig. 3.11 we can observe that the correct IM_3 level is only achieved when the injection amplifier OIP_3 is sufficiently high. When the injection amplifier is less linear, it will introduce significant IM_3 products that will cause an error in the measurements, such as IM_3 increase or cancellation effects.

Consequently, to have reliable linearity measurements in a conventional active load-pull setup, even when pre-matching is used, the injection amplifier linearity (and thus its peak power) needs to be at least 10 times higher than that of the DUT. It is obvious that at high power, these amplifiers, if available, will be extremely expensive. For this reason, active load-pull systems that can offer communication standard compliant device testing, for example, W-CDMA at base-station power levels (100 W and above), have not been demonstrated to date.

3.5 Conclusions

When looking at traditional load-pull topologies, it is clear that all of them have advantages and disadvantages. Mechanical tuners are simple, relatively inexpensive and can handle high power, but they are slow and limited by losses. Active load-pull systems can provide $\Gamma_L \geq 1$, are compact and therefore easily integrated for on-wafer measurements, but require expensive band-limited amplifiers for high-power devices.

By combining passive tuners and active topologies in the same "hybrid" system, it is possible to obtain many of the advantages of both systems while reducing the disadvantages [27]. Traditional passive mechanical tuners can be used to reflect high power at the fundamental frequency, thus pre-matching the

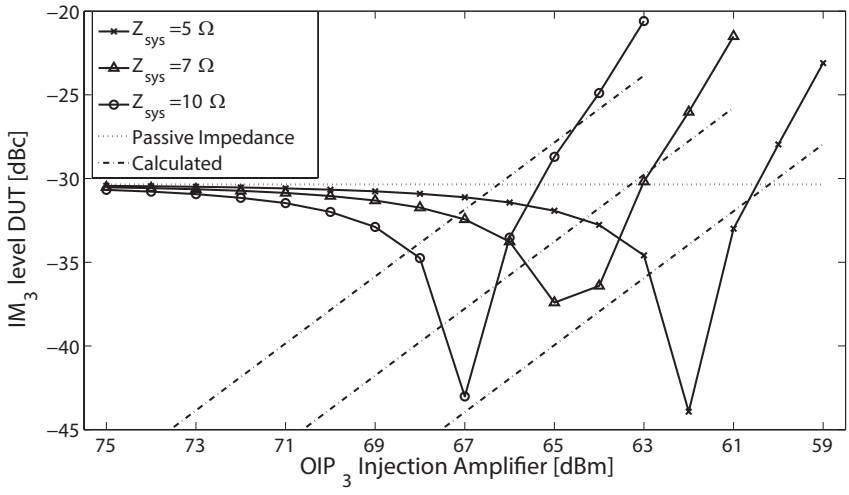

Figure 3.11: Harmonic balance simulated IM_3 level of the DUT vs. decreasing OIP_3 of the injection amplifier for different impedance pre-match values. The dotted line is the actual IM_3 level as would be achieved with passive matching techniques. The dot-dash line represents the IM_3 level only due to the P_{a_2,IM_3} as approximated by equation 3.5. A polynomial model was used for the amplifier linearity.

system impedance to a value closer to the optimum impedance of the DUT. In this case a much smaller power (and therefore a cheaper power amplifier) is required by an active load to overcome losses and achieve $\Gamma_L = 1$. Additionally, active tuning can be used at higher harmonics, where $\Gamma_L = 1$ is required for optimizing PA efficiency, and the power levels are often well below the power of the fundamental signal. In this case less-expensive wideband amplifiers may be used to accomplish active harmonic load-pull.

No matter which combination of techniques is used, electrical delay is something inherent to the analog nature of the measurement setup and can only be minimized, by reducing the physical distance between the DUT reference plane and the tuning element [41]. This problem is ultimately the main limitation that impairs the user from performing load-pull measurements using realistic wideband communication signals. For this purpose, the following chapters of this thesis propose a new load-pull measurement system based on mixed-signals techniques, which combines the traditional analog microwave and RF methodologies with the advantages of digital signal generation and acquisition. The system realized proves to have many advantages over existing techniques, such as high-speed single-tone device characterization, high Γ,

and wideband impedance control for realistic communication standard compliant modulated signals, resulting in a far more realistic characterization of the DUT.

Chapter 4

Mixed-Signal Active Load-Pull with Realistic Wideband Modulated Signals

The previous chapter has introduced the traditional load-pull topologies along with their strengths and weaknesses, and has highlighted several areas where major improvements are required in order to meet the demands of today's power amplifier design. The following chapters describe a novel active harmonic load and source-pull system, which was developed at the Electronics Research Laboratory of the Delft University of Technology during this thesis work, to overcome the limitations of conventional load-pull configurations outlined previously. The proposed solution couples traditional analog and microwave techniques with low-frequency signal acquisition and generation and the related digital signal processing, and will be referred to as "mixed-signal" active load-pull.

This chapter describes the principles of this approach, the specific hardware and software requirements and the ability of this load-pull setup to work with realistic wideband communication signals. Measurement examples are provided that illustrate the realized system functionality.

4.1 The wideband, open-loop load-pull approach

When testing a non-linear device with modulated signals, the measured waveforms will include not only the fundamental frequency band, but also the

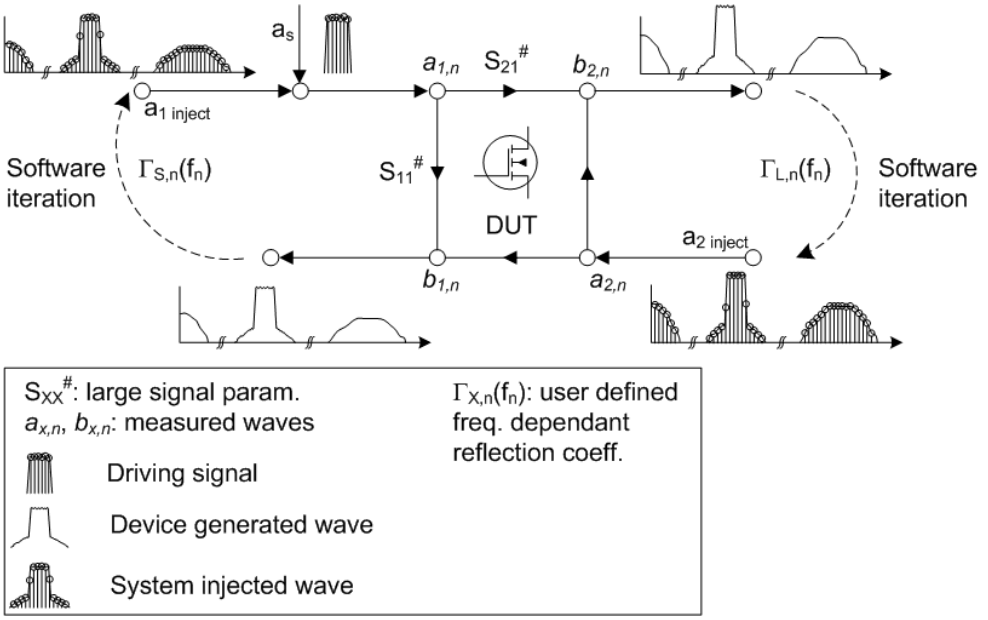

Figure 4.1: Principle of the proposed wideband, open-loop active load-pull approach. When the nonlinear DUT is excited with a user-defined modulated signal a_s, it generates signals in the baseband, fundamental and higher harmonic frequency bands. By measuring the device generated waves ($b_{1,n}$ and $b_{2,n}$), as well as the incident waves, the signals to be injected are estimated by successive iterations.

baseband, higher-order harmonics, and intermodulation distortion products (Fig. 4.1). Since the reflection coefficient is defined as the ratio of two traveling waves, the effective control of the impedances over the entire modulation bandwidth offered to the DUT can be enforced by establishing the desired linear ratios of the incident and device generated waves on the DUT versus frequency. In other words, we need to inject a signal at all of the frequency components of interest according to the linear relation

$$a_{x,n}(f_n) = b_{x,n}(f_n) \cdot \Gamma_{x,n}(f_n) \ , \tag{4.1}$$

in which $a_{x,n}$ and $b_{x,n}$ are the incident and reflected waves at port x and harmonic index n, while $\Gamma_{x,n}$ represent the user-defined reflection coefficients versus frequency for port x and harmonic index n.

As in the classical open-loop approach, only the content of the driving waveform (a_s) is known prior to the acquisition. All other injection signals ($a_{1inject,n}$ and $a_{2inject,n}$) containing all the frequency components of the signal

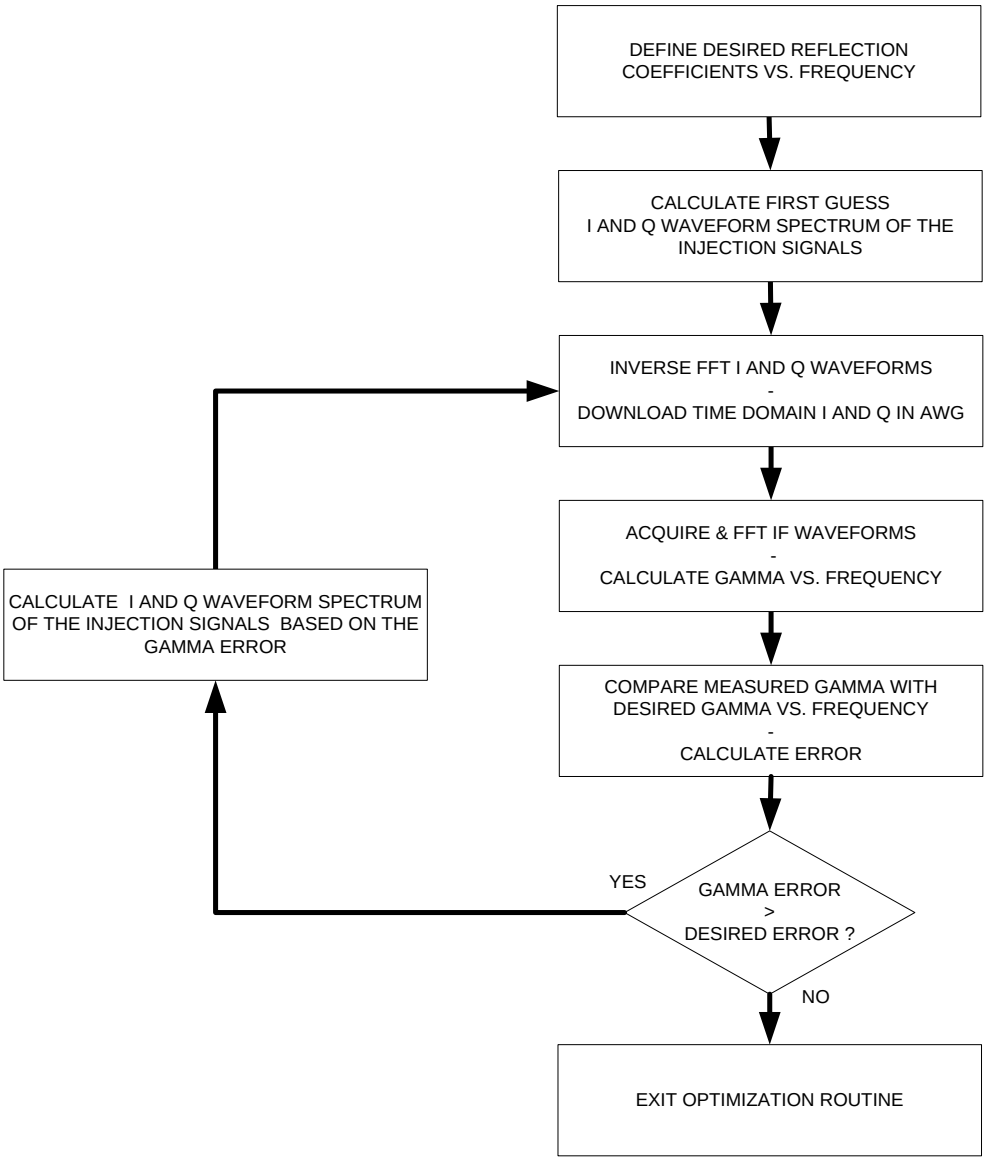

Figure 4.2: Flow diagram for the optimization of the reflection coefficients.

of interest can be created from scratch. Any desired reflection coefficient behavior vs. frequency can be created by iteratively adjusting amplitude and phase of the injected waveforms independently at each frequency component of interest. By monitoring the deviation of the measured reflection coefficient with the desired one at each frequency, the spectrum of the injected wave is optimized and found by iteration, as shown in Fig. 4.2. The error checking and optimization are done in the frequency domain, while the actual injection signals are loaded and acquired in the time domain. The open-loop approach guarantees that no sustained oscillations can occur. In practice when the user-defined, target reflection coefficients (at its input or output) force the device to operate in an unstable region, the system will simply fail to converge to its end solution. In all other situations normal convergence of the optimization algorithm will occur.

Although conceptually simple, this method requires wideband, highly linear data acquisition with high dynamic range to measure the reflection coefficients at every spectral component of the complex modulated signals with its related distortion products. Secondly, the a-waves need to be generated with a high dynamic range. Thirdly, the signal injection at the various ports need to be phase coherent at both RF as well as at the baseband frequencies. To enable operation with realistic wideband signals as currently used in modern wireless communication systems, these requirements demand a dedicated hardware and software system implementation, which we discuss in the following sections.

4.2 System configuration

A simplified block diagram of the proposed measurement setup is shown in Fig. 4.3. The test-set is based on the traditional four-coupler configuration as used in most conventional network analyzers. This configuration allows the simultaneous measurements of the source, input and load reflection coefficients at the DUT reference planes. The coupled a and b waves of the DUT are down-converted to an intermediate frequency (IF) and then sampled with wideband A/D converters (100 MS/s sampling frequency). This architecture enables the direct measurement of the device reflection coefficients over a bandwidth of 40 MHz in a single data acquisition. With this hardware, wider bandwidths (up to 120 MHz) and the frequency content in the harmonic bands can be measured by stepping the frequency of the local oscillator (LO) which drives the down-converting mixers. An open-loop architecture is used to tune the reflection coefficients at the source and load DUT reference planes, at the fundamental and harmonics. These reflection coeffi-

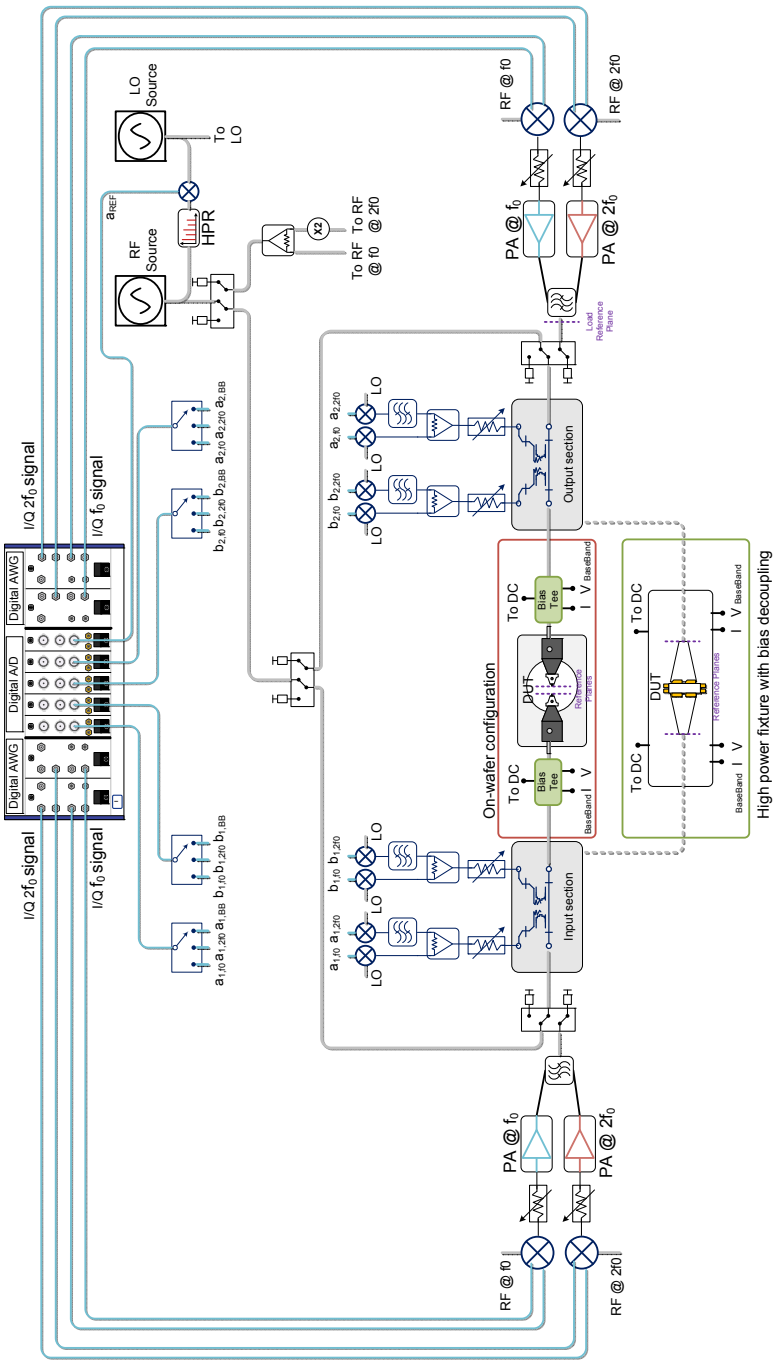

Figure 4.3: Simplified block diagram of the mixed-signal active harmonic load-pull system.

cients are synthesized by injecting signals into the DUT which are generated by baseband arbitrary waveform generators (AWG) and up-converted using in-phase/quadrature (IQ) modulators. All the AWGs and the A/D converters are integrated in a PXI express platform. They share the same time-base and are fully synchronized. Since data generation and data acquisition of both RF signals and DC parameters are handled through the PXI-based D/A and A/D instrumentation, no mechanical tuners, VNA or DC-parameter analyzer is needed, yielding a cost-effective, high-end characterization solution. Custom bias-Tees with low inductance are placed directly at the DUT reference planes in order to minimize the electrical delay of the baseband (BB) impedance, which is implemented for now as a passive impedance switch bank [41]. Low-frequency couplers for the baseband impedance measurement are also implemented on the baseband board. Note that in a more extended version, the baseband impedance can also be made active and controlled by an additional AWG (see Section 7.1.2).

4.2.1 Signal generation

The source and all injection signals needed to create the user-defined reflection coefficients at the DUT reference planes originate from fully-synchronized (400 MS/s) arbitrary waveform generators. When using the open-loop load-pull concept to control the reflection coefficient provided to the DUT, it is important that the source and all the injected signals at fundamental and harmonics are phase coherent, or in other words, are perfectly locked in phase and exhibit no phase drift among each other. To guarantee phase coherency, IQ up-conversion is preferred over digital IF techniques [60]. By employing IQ up-conversion, a single RF source can be used to drive the local oscillator port of the IQ mixers that up-convert the baseband signals. In this setup, frequency multipliers are used to obtain the LO signals which drive the IQ mixers used for generating the higher harmonics (e.g., a x2 multiplier is used for generating the 2^{nd} harmonic). This approach guarantees that the active loads and the driving signal are fully phase coherent.

Finally, computer-controlled attenuators and high-power amplifiers are placed after the IQ up-converters, in the signal path, in order to level the power of the injection signals. This approach allows us to make full use of the maximum dynamic range of the arbitrary waveform generators at all times, something that will prove essential for meeting the spectral requirements of modern wideband communication signals.

Another advantage of the IQ approach, compared to other known signal generation techniques, is the relatively limited length of the data records needed to fulfill the standard model requirements of complex modulated sig-

nals, yielding a significant speed advantage in practical measurement situations.

4.2.2 Data acquisition

To obtain an accurate representation of the spectral content of the RF waves at fundamental and harmonic frequencies, the measured power waves need to be down-converted to a lower frequency prior to data acquisition. This is a common technique used in super-heterodyne receivers, and yields the highest possible dynamic range. However, to do this correctly for modulated signals, it is very important that the detection path is free from nonlinear errors that cannot be corrected by linear calibration techniques. To maximize the detection dynamic range of the harmonic frequency components, power splitters and high-pass filters are used at the detection ports of the couplers in the input and output sections, as shown in Fig. 4.3 [61]. By high-pass filtering the higher harmonic components, the mixer used for the down-conversion in this signal path is protected from the (high) power of the fundamental signal. This drastically relaxes the mixer linearity requirements for the second and higher harmonics, improving the quality of the acquired signals. By stepping the LO frequency, the frequency band centered around the harmonic of interest is down-converted to its low IF representation for data acquisition. The detection dynamic range of the system in the fundamental frequency band is maximized by using variable attenuators in the RF path and high-power, high-linearity mixers. Note that DUT nonlinearities also give rise to baseband signals, which do not need frequency conversion prior to the data acquisition. The resulting low IF signals and the baseband signals from the DUT are fed to high-speed multiplexing switches in order to reduce the number of wideband A/D converters needed.

4.2.3 System operating frequency and bandwidth

The system operating frequency has in principle no strict limitation, since it is only bounded by the frequency handling capabilities of the IQ modulators, test amplifiers and multipliers, which are widely available up to K band commercially. The standard test-set implementation allows measurement and control of the DUT reflection coefficients from 400 MHz to 18 GHz. The only band-limiting components of the system are the frequency multiplexers and the high-pass filters for the harmonic mixers, which cover one octave bandwidth (e.g., 1.5 GHz to 3 GHz). These components are external to the test-set and can be easily replaced to change the frequency of operation.

When considering the modulation bandwidth, two different bandwidths should be considered, namely the signal generation bandwidth and the signal detection bandwidth. The maximum analog frequency of the arbitrary waveform generators sets the upper limit for the input signal as well as the bandwidth over which the reflection coefficients can be controlled. In the proposed setup, the arbitrary waveform generators have a sampling rate of 400 MS/s and can produce signals up to 160 MHz, which in IQ up-conversion results in a maximum controllable bandwidth of 320 MHz. The A/D converters were selected for maximum dynamic range and therefore have a slightly lower analog bandwidth of about 40 MHz. However since the only information needed for the optimization process is the reflection coefficients versus frequency at the DUT reference planes, no phase coherence is required between the data acquisition and the signal generation. Therefore the LO frequency used for down-conversion can be stepped to cover larger bandwidths, just like in a traditional network analyzer. In this way, different parts of the frequency spectrum are brought into the range of the A/D converter. However, to avoid mixer down-conversion of the undesired sidebands, the maximum signal bandwidth is limited to 120 MHz, due to the 40 MHz bandwidth of the A/D converters used.

4.2.4 System calibration

The system calibration is relatively straightforward and is a combination of the techniques described in [62–64]. A traditional two-port calibration (SOLT, LRM, TRL, etc.) [62] is performed at the DUT reference planes to measure the device reflection coefficients. Afterwards, an absolute power calibration is done by connecting a power meter at either one of the DUT reference planes. An additional calibration step can be performed at the load reference plane to allow on-wafer measurements. During this step “short”, “open” and “load” standards are connected in turn to the load reference plane, when a “thru” is used as a DUT. In this case, since the power meter cannot be directly connected to the wafer probes, the power calibration is also performed at the load reference plane [63]. An additional calibration step is necessary for measuring the baseband impedance and is performed by use of “short”, “open” and “load” standards at the DUT input and output reference planes [64]. Finally, an optional calibration step can be performed to correct for IQ modulator imperfections. During this step the IQ modulator’s leakage is minimized by adjusting DC offsets, while balance and quadrature errors are corrected through digital pre-compensation [65].

4.3 Signal processing for modulated signal measurements

The following sections describe the signal processing required to generate and measure the waves which are used during modulated signal measurements.

4.3.1 Signal generation

When working with complex modulated signals, a good place to start is the modulation test standard [9, 66]. According to the standard, a test signal is created which consists of a finite sequence of IQ data samples specified in the time domain. In conventional lab instrumentation such as vector-signal generators, this sequence for a given standard (e.g., W-CDMA) is typically embedded in the instrument. During testing these signals are uploaded in the internal arbitrary waveform generators (AWG) and up-converted with IQ mixers yielding the modulated RF signal. In practice, these test records are repeated sequentially yielding a large but finite number of discrete spectral components in the frequency domain. More precisely, the number of samples, in combination with the sampling speed at which the signal is generated, result in an effective frequency bin size (Δf_{AWG}), or frequency resolution of the generated signal

$$\Delta f_{AWG} = \frac{fs_{AWG}}{N_{AWG}} = \frac{1}{T_{MOD}} \ , \tag{4.2}$$

where Δf_{AWG} represents the frequency bin size of the generated signals, and fs_{AWG} and N_{AWG} are (respectively) the sampling frequency and the number of samples used by the arbitrary waveform generators to construct the waveform. T_{MOD} is the minimum period of the source signal in the time domain, that is needed to comply with the specifications of the standard test model.

To provide the reader with an example, a W-CDMA signal has a channel bandwidth of 5 MHz, a chip rate of 3.84 Mcps, 2560 chips/slot and 15 slots/frame. When considering one frame, the complex waveform is 10 ms long, or in other words, it will have a frequency resolution of 100 Hz. If we then consider a single slot, the frequency resolution becomes 1.5 kHz. This frequency representation allows us to analyze modulated communication signals like "classical" multi-tone signals, but now with a very large number of frequency tones (e.g., more than 23,000 frequency tones when considering a bandwidth of 35 MHz).

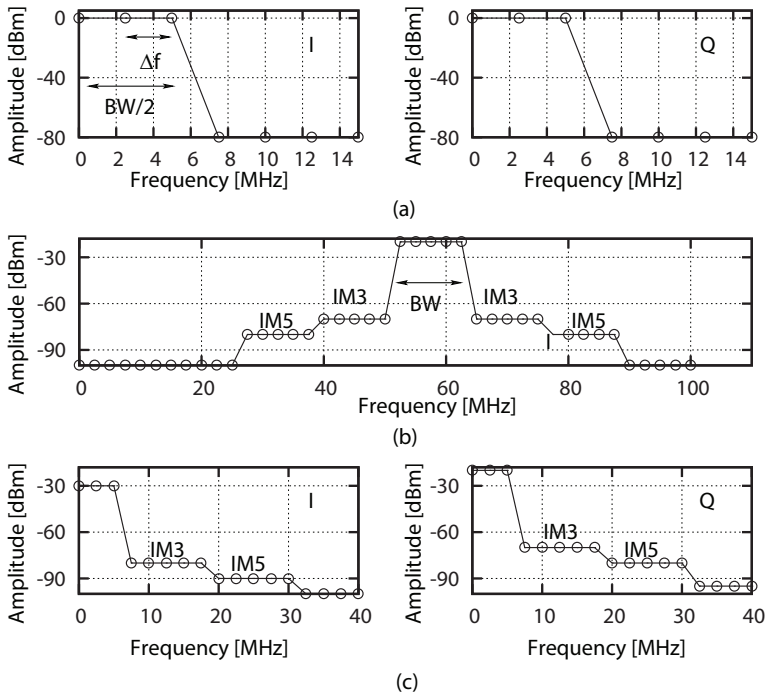

Figure 4.4: Illustration of the generated and acquired signals in the proposed load-pull system. Each circle corresponds to a frequency bin. (a) Frequency-binned spectral content of the I and Q waveforms for generating the drive signal of the DUT. (b) Down-converted low IF representation of the spectrum in the fundamental band at the output of the DUT. (c) Spectral content of the I and Q waveforms for generating the active load injection signal to achieve the user-defined reflection coefficient over the fundamental band.

4.3.2 Data acquisition

A fraction of the waves incident and reflected by the DUT is taken by the directional couplers and fed to high-linearity mixers that down-convert the signals for digitization, after which an FFT is applied to obtain their spectral content. The sampling speed of the A/D converter and the time span used for the data acquisition also set an effective frequency bin size here, which must be compatible with the original applied test signal, as described by the following expression

$$\Delta f_{A/D} = \frac{fs_{A/D}}{N_{A/D}} = \frac{\Delta f_{AWG}}{k} = \frac{1}{k \cdot T_{MOD}} \ , \tag{4.3}$$

where $\Delta f_{A/D}$ is the resulting frequency bin size of the acquired signals, $fs_{A/D}$ and $N_{A/D}$ are (respectively) the sampling frequency and the number of samples used by the A/D converters, and k is an integer.

The frequency bins of the acquisition and the generation should match for a correct measurement, thus the frequency resolution of the A/D converter should be set equal (k=1), or an integer factor larger (smaller frequency bin size) than that of the generated signals.

4.3.3 Working example

To provide the reader with some intuitive insight into how these spectra appear when operating with modulated signals, Fig. 4.4 depicts the frequency binned spectral content of the I and Q signals to be delivered to the IQ modulator (Fig. 4.4a). This block generates the RF source signal which drives the DUT with a given modulation (e.g., W-CDMA). Due to the always-present nonlinearities of the active device under test, the DUT generated waves ($b_{1,fund}$ and $b_{2,fund}$) will contain intermodulation sidebands besides the desired fundamental signal. Moreover, spectral content generated by nonlinearities will also be present in the baseband and harmonic frequency bands. When considering fundamental operation (same reasoning applies also for the harmonic frequency bands), the down-converted RF signal with intermodulation sidebands is given in Fig. 4.4b. In order to realize the desired reflection coefficients over the total bandwidth where spectral content is present, the I and Q injection signals must now include the third- and fifth-order intermodulation distortion (IM_3 and IM_5) sidebands (Fig. 4.4c). Failing to provide the proper signal at the IM_3 and IM_5 frequency bands would create an unrealistic 50 Ω termination for those DUT generated signals, invalidating any linearity performance measurement.

4.4 System performance

To demonstrate the functionality of the setup, a test signal composed of 161 sinusoidal tones in the bandwidth between 2060 MHz and 2220 MHz is fed to a "thru", while the output active load is set to provide an open condition over the whole 160 MHz bandwidth. Fig. 4.5 shows the measured reflection coefficient at the output reference plane of the "thru" as a function of frequency. It is clear from the plot that the desired reflection coefficient ($\Gamma_L = 1$) is achieved for all frequencies without any phase delay or amplitude unbalance.

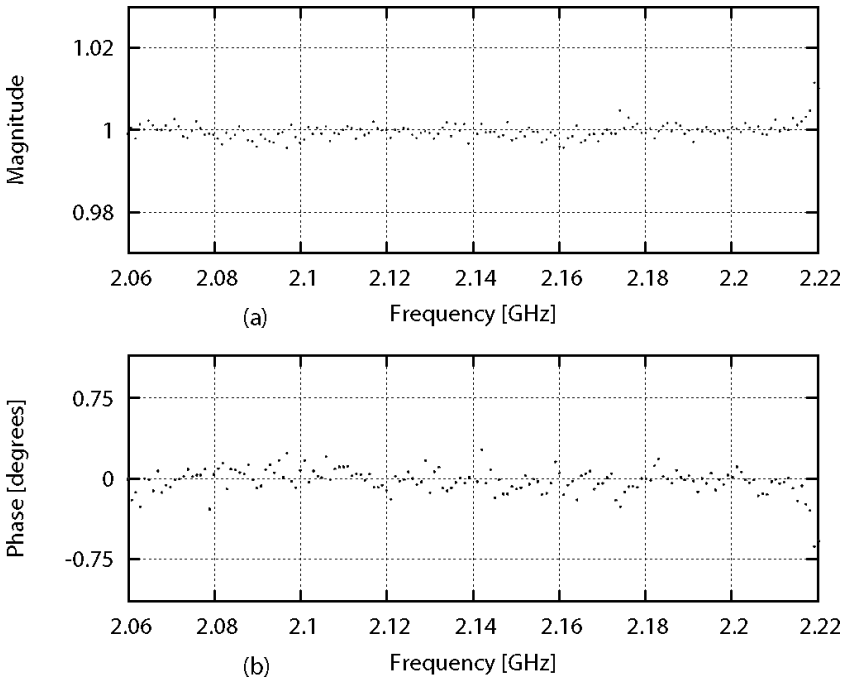

Figure 4.5: Measured reflection coefficient at the output reference plane of the DUT for a signal composed of 161 sinusoidal tones in a 160 MHz bandwidth.

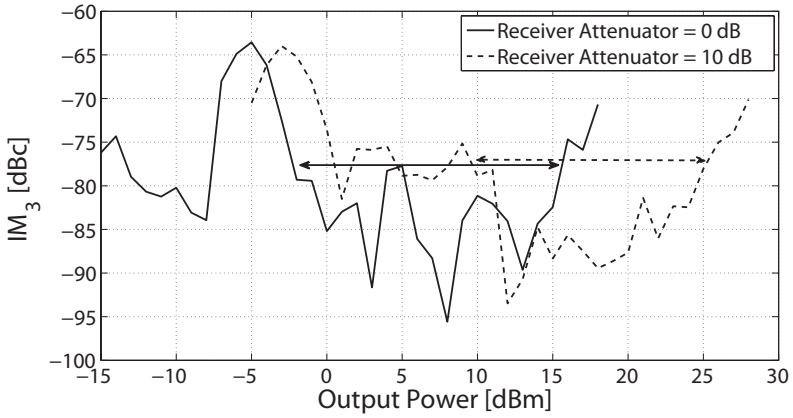

Figure 4.6: IM_3 measurements on a "thru" for different receiver attenuation settings. The results show the system measurement dynamic range.

4.4.1 Measurement linearity and dynamic range

Since mixer based down-conversion is used to measure the reflection coefficients at the reference planes of the DUT in a wideband fashion, the dynamic range of the signal detection will be limited by the system noise floor at lower powers and by the mixers nonlinearities at very high power levels.

Consequently, we have optimized our system for low noise and made use of high-linearity mixers in the signal detection path. Furthermore, stepped attenuators, controllable from 0 to 70 dB of attenuation in steps of 10 dB, are placed in the receiver path, just before the down-converting mixers.

Fig. 4.6 shows the IM_3 measured on a "thru" for a two-tone stimulus, and for different attenuation settings, versus output power. For each attenuation setting, the resulting dynamic range is about 75-80 dB in the signal detection, over a 15 dB span in output power.

4.4.2 Active load dynamic range

In order to control and optimize the reflection coefficient offered to the DUT for a particular frequency bin, it is necessary to measure the power waves for that frequency bin with high-accuracy and repeatability. For this reason, one should avoid the use of noisy data since this would make the optimization of the reflection coefficient unstable. Therefore, the reflection coefficient is controlled only for those frequency bins where the power exceeds a user-specified threshold level. The selection of these power levels sets the dynamic range over which the load reflection coefficient can be controlled. We will refer to this as the "active load dynamic range". As mentioned in Section 4.2.1, computer-controlled stepped attenuators are used to guarantee full use of the voltage swing produced by the arbitrary waveform generators at all times. Therefore, the active load dynamic range will be limited only by the measurement noise, the IQ mixer imperfections and the robustness of the optimization algorithm used.

To give the reader an estimate of the "active load dynamic range" that can currently be achieved, a W-CDMA input signal centered at 2.14 GHz is fed to a heterojunction bipolar transistor (HBT) with an emitter area of 528 μm^2. The power of the signal is chosen purposely high so that the active device clips and generates intermodulation sidebands. The active load at the DUT output for the fundamental is set to provide a constant reflection coefficient ($\Gamma_L = |0.283| \angle -135^o$) across the entire 20.4 MHz bandwidth. Fig. 4.7 shows the reflection coefficient and power spectrum measured at the DUT output. Note that the reflection coefficient can be controlled accurately over the whole (broadened) spectrum over a 60 dB power range, and the loss of fidelity at

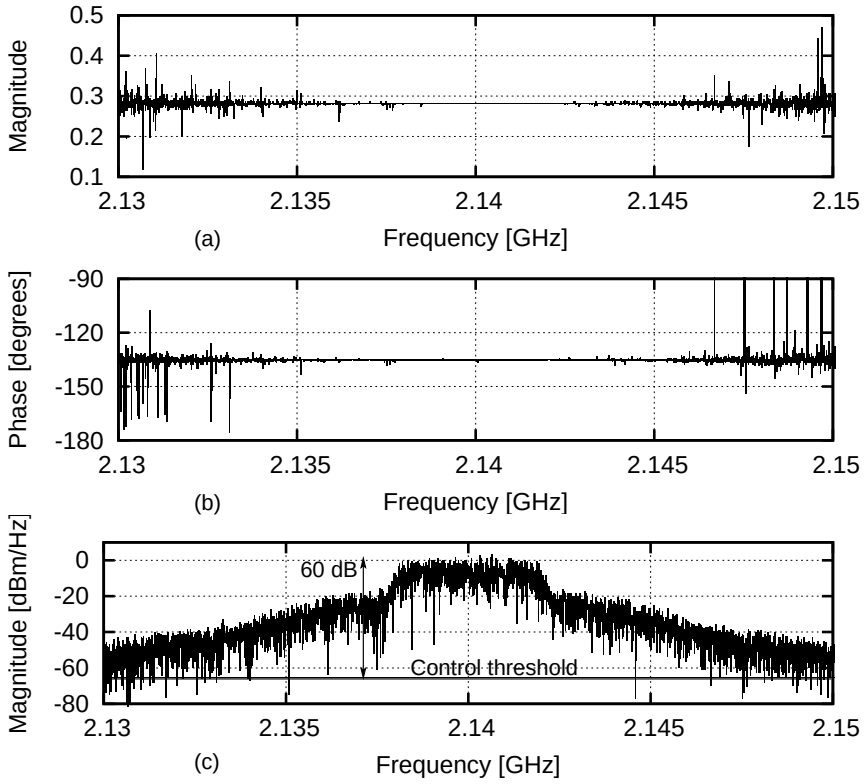

Figure 4.7: Measured load Γ in (a) magnitude and (b) phase, and (c) power spectrum (resolution bandwidth of 6 kHz) at the output reference plane of a HBT overdriven with a W-CDMA signal yielding spectrum broadening. The user-specified reflection coefficient is $\Gamma_L = |0.283| \angle -135^{\circ}$. The power threshold level for the load reflection coefficient is set to -65 dBm.

the edge of the band corresponds to those frequencies where the signal power falls below the user-specified threshold.

4.5 Measurement results

To demonstrate the unique capabilities of the active open-loop load-pull setup, a NXP GEN6 LDMOS device with a gate width of 1.8 mm is measured using wideband modulated signals in load-pull test conditions. In all of the experiments a drain current and voltage of 13 mA and 28 V respectively are used. For this device, the optimum fundamental load and source matching conditions are found using conventional single-tone load-pull measurements,

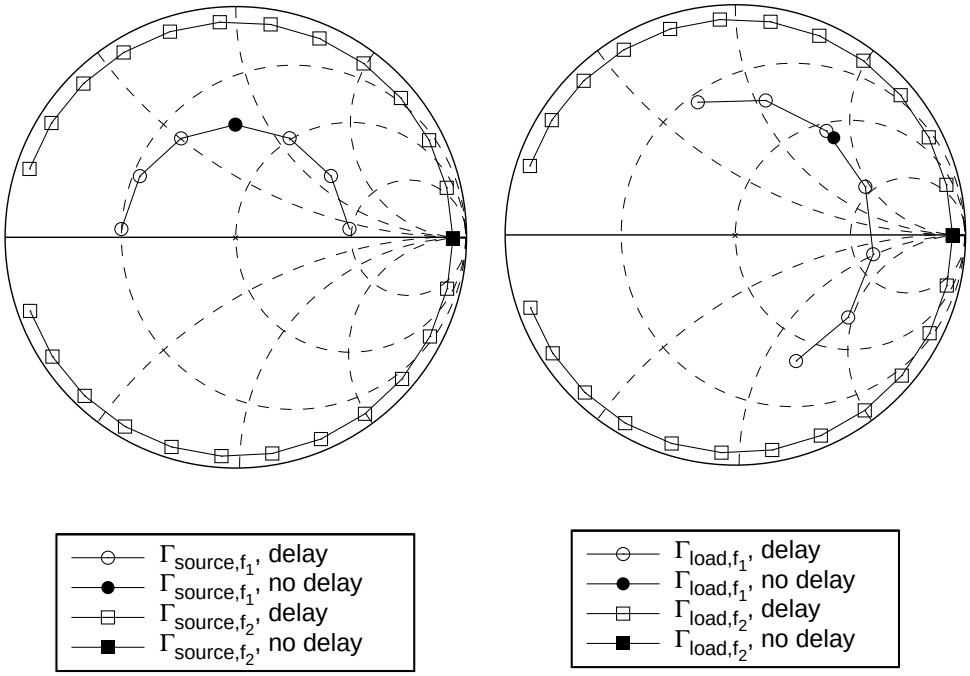

Figure 4.8: Source and load reflection coefficients at the device reference plane in the fundamental (2.1225 GHz - 2.1575 GHz) and harmonic (4.245 GHz - 4.315 GHz) frequency ranges, with electrical delay (open symbols) and without electrical delay (filled symbols).

namely: $\Gamma_{L,f1} = |0.6| \angle 45^{o}$ and $\Gamma_{S,f1} = |0.5| \angle 90^{o}$. The input and output baseband impedances enforce a short condition, and the input and output 2^{nd} harmonics are set to an open circuit condition ($\Gamma_{L,f2} = \Gamma_{S,f2} = |0.95|$) in order to optimize the efficiency [67]. To highlight the excellent wideband control and the delay-free electrical operation of the new measurement setup, a comparison is made with a previously developed state-of-the-art active harmonic load-pull system [41], which was optimized especially for minimum electrical delay. For this purpose, we use a two channel W-CDMA signal (centered at 2.135 GHz and 2.145 GHz) and set the input and output reflection coefficients in the newly developed setup to the following two cases:

1. Without electrical delay.

2. With an electrical delay of 4.85°/MHz for the fundamental source and load and 4.6°/MHz for the 2^{nd} harmonic source and load.

Fig. 4.8 illustrates the source and load matching conditions provided to the active device under test for the two different cases. Note that the filled markers represent the source and loading conditions for the two-carrier W-CDMA signal without any electrical delay, yielding completely overlapping points in the Smith chart. As shown in Fig. 4.8, the fundamental load trajectory has been shifted for the case with electrical delay such that the optimum matching condition is now centered at 2.135 GHz. This was required to avoid the unstable region of the active device.

It is important to note that this is a comparison to the "best known case" of a classical closed-loop active load-pull system, since closed-loops are subject to amplitude variations within the control frequency bands in practice. Moreover, oscillation conditions in closed-loop systems for these very large bandwidths are difficult to avoid due to the use of wideband loop filters. Passive load-pull systems with harmonic tuning will have a comparable or even worse phase variation of the reflection coefficients versus frequency than the closed-loop system used in the comparison.

The measurement results are summarized in Table 4.1. There is significant performance degradation for the active device when measured with electrical delay present in the reflection coefficients. This is also evident from Fig. 4.9a and 4.9b which show the power spectral density at the device output reference plane for the fundamental and 2^{nd} harmonic frequency bands. Note that a 5 dB output power drop and close to 8 % degradation of the power-added efficiency (PAE) can be observed when compared to the situation with no electrical delay. Furthermore, due to the electrical delay, the output power spectrum shows significant asimmetry both at fundamental and 2^{nd} harmonic frequency bands.

MEASUREMENT RESULTS		
	Without electrical delay	With electrical delay
PAE	24.2 %	16.3 %
P_{OUT} Ch. 1	20.3 dBm	20.5 dBm
P_{OUT} Ch. 2	20.6 dBm	15.4 dBm
ACLR1 Ch. 1	-43.9 dBc	-43.0 dBc
ACLR2 Ch. 1	-42.2 dBc	-41.6 dBc
ACLR1 Ch. 2	-42.1 dBc	-41.8 dBc
ACLR2 Ch. 2	-39.6 dBc	-39.2 dBc

Table 4.1: Comparison of measurement results with and without electrical delay.

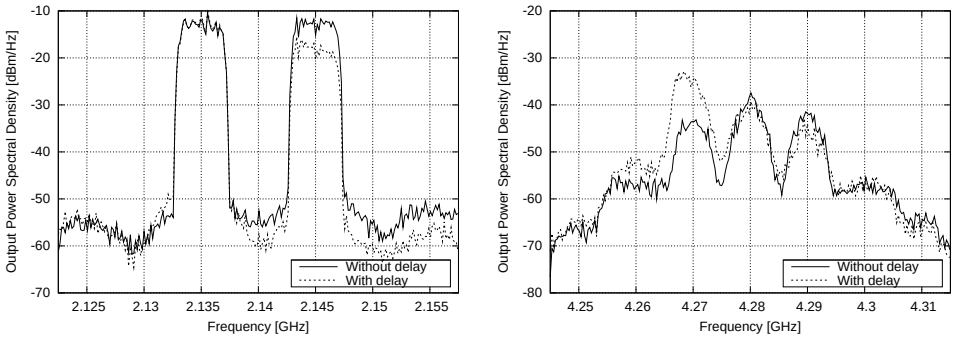

Figure 4.9: Measured output power spectral density [dBm/Hz] vs. frequency [GHz] of a NXP GEN6 LDMOS device (gate width 1.8 mm) in the proposed load-pull setup (a) at the fundamental frequency band using a 3 kHz resolution bandwidth. (b) at the 2^{nd} harmonic frequency band using a 6 kHz resolution bandwidth. The measurement is shown for the two cases with (dashed line) and without electrical delay (drawn line). The reflection coefficients offered to the device under test are given in Fig. 4.8.

4.6 Conclusions

In this chapter, a novel active harmonic load-pull setup has been presented which is suitable for large-signal device characterization under "real life" modulated signal stimulus. The new system is capable of synthesizing arbitrary source and loading conditions at the fundamental and harmonic frequencies over a frequency bandwidth of 120 MHz, and therefore permits testing of active devices under realistic (circuit-like) conditions. Furthermore, even user-defined reflection coefficients versus frequency can be downloaded to the measurement system in order to perform active device testing.

The IQ signal up-conversion and low IF down-conversion provide a very high dynamic range of about 80 dB in the signal detection and about 60 dB in the modulated active load impedance control. This proves to be sufficient for the communication standards used today in industry. Furthermore, this approach can be easily adjusted to any frequency band of interest (e.g., X-band) since all of the parts required are commercially available. The IQ-based open-loop approach in combination with the frequency binning technique described resolves all of the conventional drawbacks of current load-pull techniques, while

still being competitive in terms of measurement speed.

The unique system capabilities have been demonstrated by "load-pulling" a NXP GEN6 LDMOS device under a two carrier W-CDMA input stimulus. Note that up-to-date two-carrier W-CDMA testing, which is one of the most severe tests in industry for base-station amplifiers, is normally only performed at the circuit board level, since conventional load-pull systems fail to handle these extreme bandwidths. The advantage of controlling the electrical delay has been made evident by comparing the difference in output power and power-added efficiency of an LDMOS device with a state-of-the-art system.

Finally, the selected hardware configuration still leaves room for numerous improvements and innovations which will be discussed in the following chapters.

Chapter 5

High-Speed, High-Power, Fully-Controlled, Multi-dimensional Load-Pull Parameter Sweeps

Traditional load-pull measurement techniques are considered to be an essential tool in the large-signal characterization of high-frequency devices, since they facilitate direct determination of the optimal loading conditions of the device under test (DUT) for any give large-signal quantity (e.g., gain, output power, P_{OUT}, or power-added efficiency, PAE). Nevertheless, both passive and active techniques are highly demanding in terms of measurement time, especially when it is desired to monitor and control multiple parameters simultaneously (e.g., fundamental and harmonic terminations) at multiple input power levels. This is usually reflected in extremely long measurement times that slow down the PA design/optimization process. Recently, there have been several reports in literature proposing "real-time" (high-speed) load-pull measurements by synthesizing load reflection conditions through analog modulation techniques [68–70]. Although very good results have been achieved with these techniques, their analog nature still imposes limitations on the number, and how well these parameters (including the non swept ones) can be controlled for their value and/or sweeping range.

In this chapter, a simple mixed-signal approach to perform fully-controlled, multi-dimensional parameter sweeps, is presented. This approach enables sweeping multiple parameters at the same time (e.g., input power, fundamental and 2^{nd} harmonic load impedances), while being able to control all other non-

swept parameters (e.g., fundamental and 2^{nd} harmonic source impedances) to their user-defined values. For this purpose, the system capability to coherently synthesize any arbitrary signal at the fundamental, as well as at the harmonics, is used to generate multiple input power levels and source and load conditions in one single-shot measurement, as explained in detail in the following sections. Such functionalities result in an extremely fast large-signal device characterization tool that can dramatically speed up the PA design process.

5.1 Generation and measurement of load and source terminations

In an open-loop active load-pull system (Fig. 3.5), a signal with controlled phase and amplitude is injected to present to the DUT with a synthetic, user-specified, reflection coefficient. Since in our fully coherent system it is possible to generate any arbitrary signal, we can define the waveforms to be injected into the DUT at the fundamental and harmonics frequencies, such that they contain multiple sinusoidal time-segments with different amplitude and phase information. This approach allows the generation of any arbitrary succession of synthesized load and source terminations, both at the fundamental and at harmonic frequencies. Also, the test signal driving the DUT is generated in the same way (i.e., with multiple wave segments) in order to provide the DUT with different power levels. Fig. 5.1 shows an example of a time-segmented RF wave, where four different loads are presented to the DUT at two different power levels.

The entire ensemble of injected and device-reflected time-domain waveforms are then acquired, while the different time-segments are processed separately. In this way, it is possible to measure the entire set of loading conditions that are generated, and all of the large-signal device parameters of interest relative to each time segment in a single shot.

The major advantage of this method is that multi-dimensional parameter sweeps can be executed within a single measurement, while the coherency of the system and the measurement software allow tracking the information embedded in each wave segment. This approach eliminates the overhead of instruments settling times completely, which (in general) dominate the total measurement time in conventional load-pull setups, while providing a greater control than what is possible with analog load modulation methods.

Although a single measurement execution of such parameter sweeps takes only a fraction of a second, practical situations quite often require accurately-

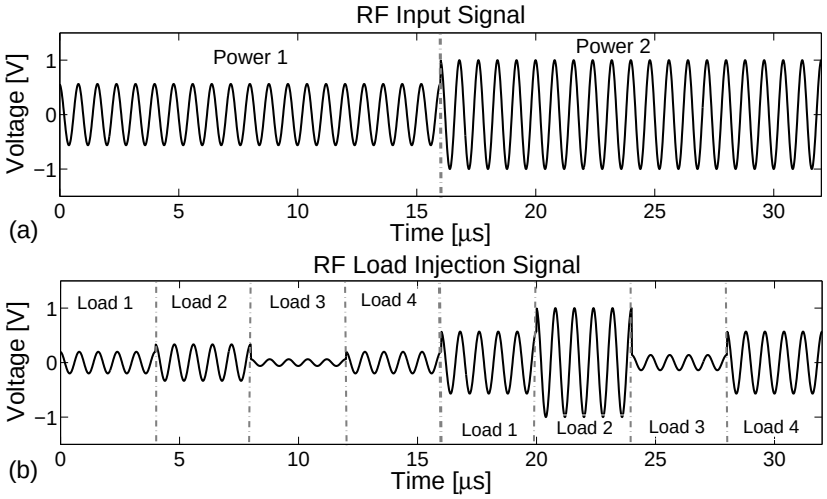

Figure 5.1: Time-segmented RF waves for (a) multiple input power levels and (b) load termination control. In this example four different loads over a range of two power levels are presented to the DUT.

controlled power and loading conditions, which in an open-loop system can only be achieved through successive iterations. In view of this, the coherent mixed-signal IQ generation in our system is exploited to optimize the individual time-segments of the IQ waveforms independently, offering full control of the applied loading and power conditions. This feature can, for example, be used to target any given area in the Smith plane, while at the same time support sweeping of the input power. These "real-time" multi-dimensional parameter sweeps are at least two orders of magnitude faster than the conventional approach of using measurement of only one signal condition at a time to construct a parameter sweep.

The total number of different measurement points is only limited by the size of the AWG's memory, and it is higher than 40,000 points with the current system configuration. The DC voltage and current waveforms needed for power efficiency calculation are also measured for each time-segment, using the same A/D converters as for the reflection coefficient measurements. In particular, the DUT current is sensed by a current probe, or across an external resistor inserted in the ground path just before the bias-tee. The resistor method requires a simple additional calibration step to accurately pre-characterize the sense resistor, as described in [71].

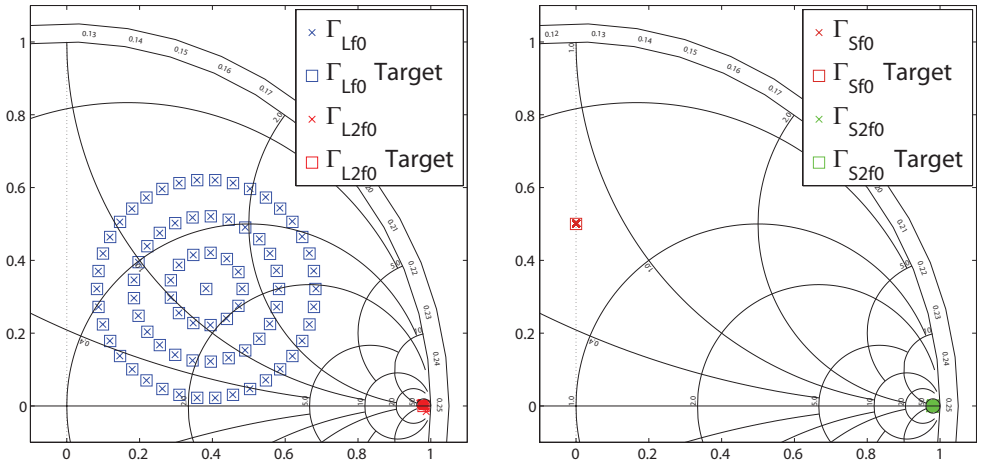

(a) (b)

Figure 5.2: Load-pull example with controlled fundamental and harmonic terminations. The user-specified targets for the reflection coefficients are represented with squares, while the actual measured ones are depicted by a cross. (a) load plane (b) source plane.

5.1.1 Measurement examples and results

To demonstrate the functionality of the new measurement methodology, a NXP GEN6 LDMOS device with a gate width of 1.8 mm has been measured. In these experiments the device has been biased at a drain current (I_D) of 13 mA and a drain voltage (V_{DS}) of 28 V, while the fundamental frequency of the RF stimulus is 2.14 GHz.

A first measurement example is given in Fig. 5.2, which shows the capability of the system to obtain, with excellent precision, any arbitrary source and load impedance state at the fundamental and harmonic frequencies. In this example the fundamental load termination provided to the DUT is swept, covering a circle centered at $\Gamma_L = |0.5| \angle 40^o$ with a radius of 0.3. The source fundamental is kept constant at the value $\Gamma_S = |0.5| \angle 90^o$, while the 2^{nd} harmonic source and load terminations are kept constant in an open circuit condition.

The ability to select any arbitrary range of reflection coefficients is particularly useful when it is desired to characterize only selected areas of the device source or load terminations in the Smith chart, for example, when one wants to avoid regions where the device is potentially instable, or loading conditions

that can yield device failure (voltage or thermal breakdown); something that is far from trivial when using analog load-modulation methods. An example is given in Fig. 5.3, showing the constant PAE contours for a given P_{AVS} as measured with the proposed technique.

In this example, the output stability circle was first obtained from the (previously measured) device small-signal S parameters [37], then only the stable region was addressed in the actual measurement by a fundamental load sweep at various (much higher) power levels. In this measurement the output power of the device has been obtained for 90 different load terminations, keeping Γ_S fixed to the previously specified value, while at the same time sweeping the source and load harmonic terminations between open and short conditions, and the power available from the source from 1 to 16 dBm. The total time for this measurement, which consists of more than 5,000 controlled measurement points, is below 5 minutes.

Given the importance of second harmonic source and load termination control in PA design, which has been addressed several times in literature [72, 73], the capability of the presented system to simultaneously sweep the 2^{nd} harmonic impedances presented to the DUT can prove to be very useful when investigating the optimal device terminations for high-efficiency / high-linearity operation. The constant PAE contours plotted in Fig. 5.3 show that the highest PAE values are obtained with the 2^{nd} harmonic load impedance set to an open, and the 2^{nd} harmonic source impedance set to a short. For this latter case, the measured PAE as a function of P_{OUT} and the measured transducer power gain (G_T) as a function of P_{AVS} are plotted for all the different fundamental loading conditions in Fig. 5.4a and Fig. 5.4b, respectively.

Finally, the constant PAE contours shown in Fig. 5.5a and 5.5b allow the reader to compare the results obtained using the proposed "real-time" technique and a traditional open-loop load-pull technique under the same P_{AVS} and loading conditions. The excellent agreement between the two methods indicates that the much higher measurement speed of the new approach does not affect accuracy.

5.2 High-power, real-time pulsed-RF measurements

For single-tone CW signal conditions, the system configuration described is able to generate and measure thousands of source and load conditions at different power levels in a single acquisition. This feature provides ultra-fast load-pull device characterization. However, for high-power devices, the use

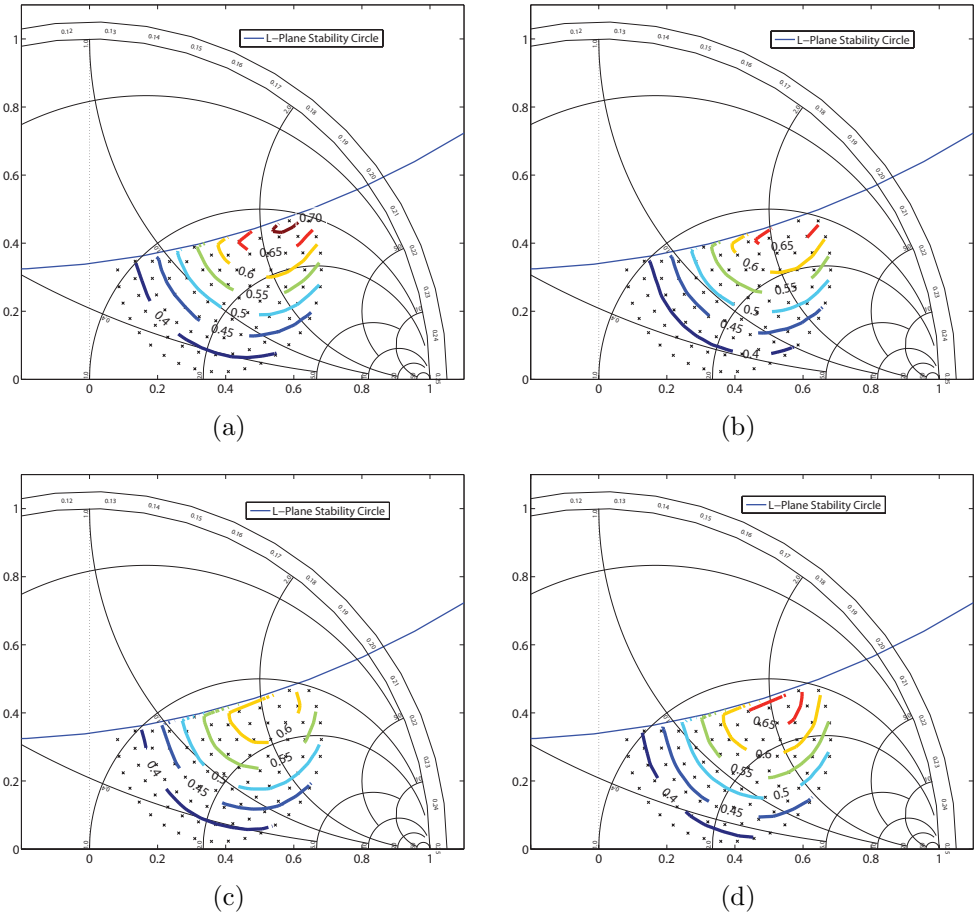

Figure 5.3: Constant PAE load-pull contours for a NXP GEN6 LDMOS device ($P_{AVS} = 14\ dBm$). In this measurement the power available from the source is swept from 1 to 16 dBm for 90 different load terminations. The source fundamental termination is set to $\Gamma_S = |0.5|\ \angle 90^o$, while load and source 2^{nd} harmonic terminations are swept to: (a) open - short (b) open - open (c) short - open (d) short - short using the proposed technique. Note that the unstable area for the DUT is avoided directly during the measurement (i.e., no measurement points taken in the potentially unstable region).

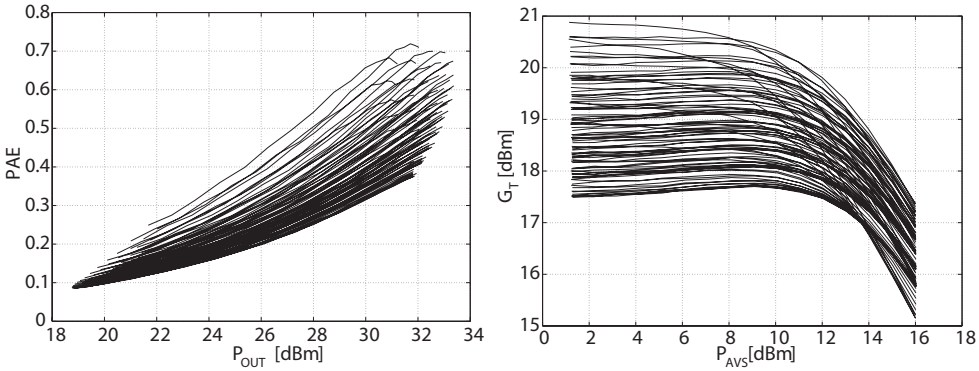

(a) (b)

Figure 5.4: (a) PAE as a function of P_{OUT}, (b) G_T as function of P_{AVS}, plotted for 90 different load terminations. The source fundamental termination is set to $\Gamma_S = |0.5|\ \angle 90^{o}$. The 2^{nd} harmonic load and source are set to an open and a short, respectively.

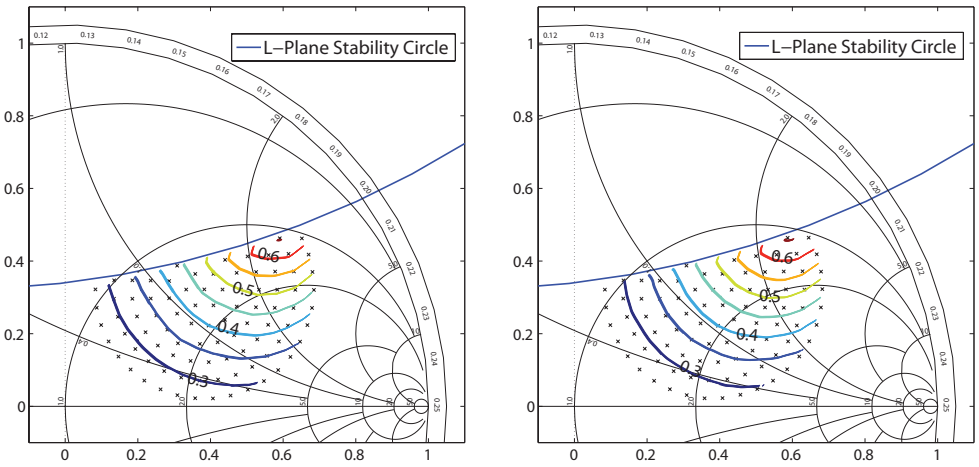

(a) (b)

Figure 5.5: Comparison of load-pull PAE contours with swept fundamental load terminations ($P_{AVS} = 11\ dBm$). The source fundamental termination is set to $\Gamma_S = |0.5|\ \angle 90^{o}$, 2^{nd} harmonic terminations are set to open circuit with (a) the proposed technique, (b) the traditional technique.

of CW conditions needs to be omitted to avoid self-heating, which in extreme conditions can even yield device failure. This is especially true for base-station devices which are optimized for operation with complex modulated signals. These signals reach their peak values only occasionally. As a result the active device operates most of the time in power back-off. Consequently, pulsed-RF operation is required in order to create realistic load-pull testing conditions. For this reason we extend the original concepts described in Section 5.1 to pulsed operation at much higher peak power levels (above 100 W). These additional features allow the user to perform accurate high-power, ultra-fast device characterization, while providing full control over the maximum operating conditions of the active device, thus avoiding voltage and thermal breakdown conditions.

All of the waveforms to be injected into the input and output ports of the DUT are defined such that they contain multiple sinusoidal time-segments with different amplitude and phase information. As a result, the device will experience a sequence of time segments with different input powers and loading conditions. When working under pulsed-RF conditions, the desired duty cycle is achieved by adding a sufficient "idle time" after the stimulus representing the different power and load states. An example is shown in Fig. 5.6, where the input waveform to the DUT and the load injected waveforms are depicted. In this simplified case the DUT will "experience" two input power levels, and three different load impedances.

The desired injection signals are then optimized independently for each segment to synthesize the desired impedances seen by the DUT. Note that the use of iterations to optimize the injection signals opens up the possibility to introduce several features that ensure safe device operation during the measurement, something that is extremely useful, especially at high power levels. For example, it is possible to exclude from the measurement a range of impedances that might cause device instability [74]. Furthermore, it is possible to check the gain compression of the device for every impedance during each iteration, thus limiting the input power at impedances where the DUT gain reduces by more than a user-specified amount.

5.2.1 High-power measurement examples

As application example of the proposed active load-pull concept, a complete load-pull and power sweep for a NXP BLF7G22LS-130 device was carried out at a frequency of 2.14 GHz under pulsed-RF conditions. In this example, a pulse width of 10 μs and 10 % duty cycle were used. The power gain compression was limited during this measurement to 4 dB to avoid device degradation due to extreme gain compression, e.g., in higher load line regions.

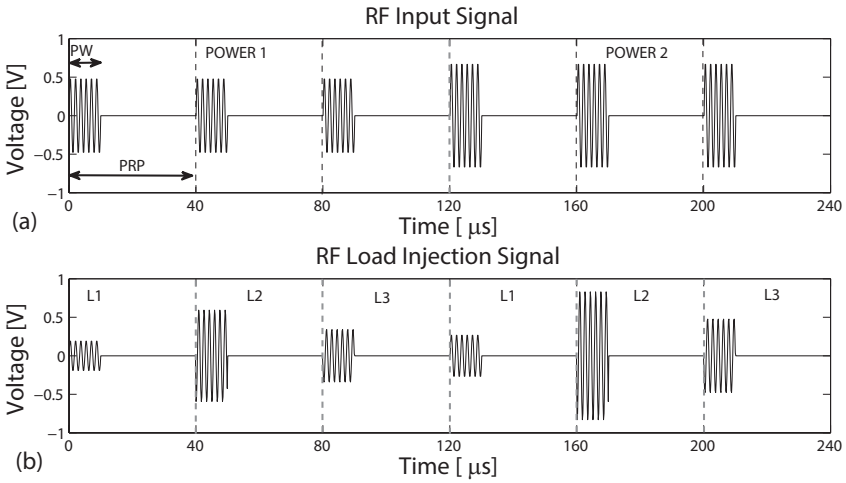

Figure 5.6: Time-segmented pulsed-RF waves for (a) multiple input power levels and (b) load termination control with pulsed-RF. In this simplified example, three different loads for two input power levels are presented to the DUT.

The results are shown in Fig. 5.7, where the maximum output power contour and the PAE at 3 dB of gain compression are plotted. Also in Fig. 5.8, the PAE versus output power calculated at a gain compression level of 3 dB is shown. Note that the complete device characterization with 25 power levels at each of the 50 load impedances takes less than 3 minutes.

5.3 High-power measurements with modulated signals

The mixed-signal active harmonic load-pull system is unique in that it can perform active load-pull device testing with communication-standard-compliant wideband modulated signals like W-CDMA. This feature has been described in detail in Chapter 4 and demonstrated for low-power levels. In this section the capability of the system to work with complex modulated signals is extended to the power levels that are typically in use for base-station applications (e.g., peak envelope power of 200 W).

As previously explained in Section 3.4, to synthesize a specific Γ_L at the DUT reference plane in an active load-pull system, it is necessary to inject a certain amount of power into the DUT. An extra complication when working

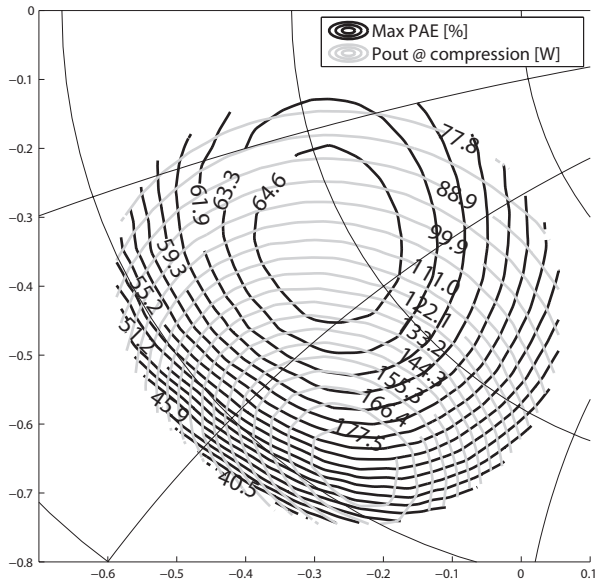

Figure 5.7: Load-pull contours of maximum power added efficiency and output power at 3 dB of gain compression for a NXP GEN7 LDMOS device at different load states and input powers, using pulsed single-tone conditions (10 μs pulse width and 10 % duty cycle).

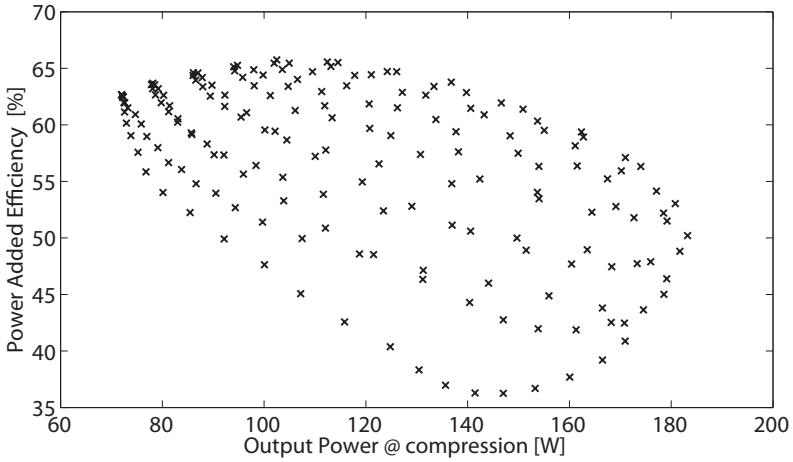

Figure 5.8: Measured PAE vs. output power at 3 dB power gain compression level for a NXP GEN7 LDMOS device at different load states and input powers, using pulsed single-tone conditions (10 μs pulse width and 10 % duty cycle).

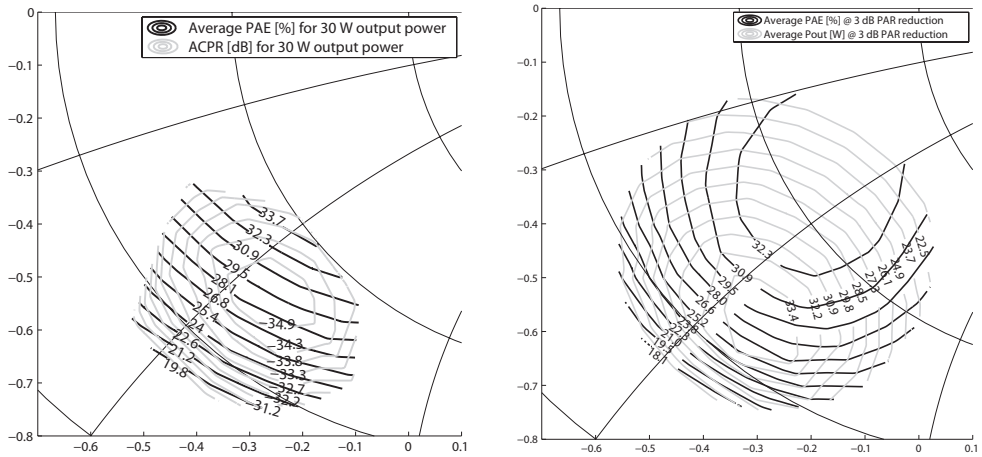

(a) (b)

Figure 5.9: (a) Load-pull contours of average power added efficiency and ACPR for an average output power of 30 W. (b) Load-pull contours of average power added efficiency and average output power at 3 dB of peak-to-average ratio reduction. The related peak-to-average power (PEP) is as high as 150 W.

at high powers with wideband signals arises because the linearity of the injection amplifier needs to be taken into account. When the injection amplifier is not sufficiently linear, it will introduce intermodulation products in a "conventional" active load-pull system, that will cause significant measurement errors, such as IM_3 increase or cancellation effects. To have reliable linearity measurements in a "conventional" active load-pull setup (even when pre-matching is used), the injection amplifier linearity (and thus its peak power) needs to be at least 10 times higher than that the of the DUT, as concluded from the simulation shown in Fig. 3.11. When working with devices designed for base-station applications where peak envelope powers are as high as 200 W, using such amplifiers becomes extremely expensive and impractical.

Instead, an iteration process is performed in the mixed-signal active load-pull system, to optimize the reflection coefficient of each individual frequency component of the wideband signal (e.g., 23,362 tones with 1.5 kHz spacing for a W-CDMA considering a total bandwidth of 35 MHz). Due to these iterations, the injection amplifier is pre-distorted for its own non-linearities. This allows the use of injection amplifiers with much lower linearity than what is typically required in conventional active load-pull systems.

As an example consider Fig. 5.9, which shows ACPR, average PAE and output power for a single-channel W-CDMA signal at 2.14 GHz with a peak-to-average ratio of 9.5 dB. It should be stressed that in these experiments the maximum saturated power rating of the injection amplifier is only 200 W, with an associated 60 dBm output IP_3. In these measurements, the non-linearity of the injection amplifier does not affect the measurement results because Γ_L is controlled to the user-defined value in and out-of-band.

5.4 Conclusions

In this chapter, the measurement principles that enable the mixed-signal active harmonic load-pull system to be compatible with the requirements of high-speed, high-power, high-linearity base-station applications have been presented. The system provides ultra-fast large-signal device characterization in both CW and pulsed conditions. For the latter, both the duty-cycle and the gain compression of the DUT during the measurement can be controlled. All of these features are crucial in guaranteeing the safe operating conditions for high-power DUTs ($>$ 100 W).

In addition, high-power device characterization with realistic W-CDMA signals has been demonstrated. It was shown that the realized system can compensate for nonlinearities of the injection amplifiers, which normally would obscure the linearity and ACPR measurements. This property allows the use of cheaper injection amplifiers, providing a lower P_{SAT} than required in conventional active load-pull systems. The ability to eliminate losses and electrical delay while being completely free to define the source and load reflection coefficients vs. frequency, allows perfect mimicking of in-circuit situations, making the system an extremely valuable tool for the RF power amplifier developer.

Chapter 6

Measurement of Time-Domain Waveforms

The measurement of time-domain voltage and current waveforms has proven to be of fundamental importance for the design and optimization of active devices operating under large-signal conditions. Engineers use time-domain waveform measurements for several purposes: amplifier design [53, 75], device model extraction [76, 77] and validation [78, 79], as well as for ruggedness evaluation [80] of active devices.

Time-domain waveform measurements are easily made using a conventional real-time oscilloscope at low frequency, while at RF and microwave frequencies the situation is more complicated. This is due to the fact that the parasitic effects of the measurement system can no longer be neglected or reduced to simple low-pass filtering effects, thus requiring extensive calibration procedures such as those commonly used in VNAs.

In the following sections, the fundamentals of time-domain waveform measurements are introduced. The performance of a commercially-available phase reference and a newly-realized phase reference prototype are examined. Their impact on the quality of the phase calibration is estimated. Finally, an approach for time-domain waveform analysis of multi-tone signals which are closely spaced in frequency is introduced.

6.1 Time-domain waveform measurement fundamentals

Due to their non-linear operation, power amplifiers generate harmonics at frequencies $N \times f_0$ at their output when driven by a CW signal at frequency,

f_0. When considering a periodic signal, the time-domain voltage and current waveforms can be reconstructed from the incident and reflected waves (i.e., a and b) measured in the frequency domain at the input and output of the non-linear DUT [81] as

$$v_i(t) = \sqrt{Z_0} \cdot [a_i(t) + b_i(t)] \tag{6.1}$$

$$i_i(t) = \frac{1}{\sqrt{Z_0}} \cdot [a_i(t) - b_i(t)] \ , \tag{6.2}$$

where i is the port number, and

$$a_i(t) = \sum_{n=0}^{N} a_{i,n} \cdot \cos(n\omega_0 t + \phi_{a_i,n}) \tag{6.3}$$

$$b_i(t) = \sum_{n=0}^{N} b_{i,n} \cdot \cos(n\omega_0 t + \phi_{b_i,n}) \ . \tag{6.4}$$

Variables $a_{i,n}$, $b_{i,n}$ and $\phi_{a_i,n}$, $\phi_{b_i,n}$ are the amplitude and phase coefficients of the power waves measured at the fundamental and harmonic frequencies, respectively.

The errors in a measurement system have to be removed by means of a system calibration when working at microwave frequencies. In VNAs, all of the error contributions of the measurement system are described by an error model [62, 82]. As an example, consider the flow graph in Fig. 6.1 which depicts the error model at the input port of the DUT. The four error terms e_{d1}, e_{s1}, i_{01} and i_{10} represent the error network between the DUT reference plane and the measurement plane. By measuring several electrical standards, the error terms of the model can be calculated and the measurement corrected up to the DUT reference plane.

Conventional network analysis, however, allows only the measurement of the ratio of power waves (e.g., b_1/a_1). In fact, only the product term $i_{01} \cdot i_{10}$ is derived when referring to the classical 12 term error model used for VNA calibration. This is better explained when considering the flow graph in Fig. 6.1. Equations 6.5 and 6.6 can be derived from the flow graph, which allow the calculation of the calibrated incident and reflected waves at the input port of the DUT from the measured quantities a_1^M and b_1^M. It is clear that the two terms i_{01} and i_{10} have to be known independently both in amplitude and phase in order to calculate a_1 and b_1 according to

$$a_1 = \frac{e_{s1} \cdot b_1^M - \Delta \cdot a_1^M}{i_{01}} \tag{6.5}$$

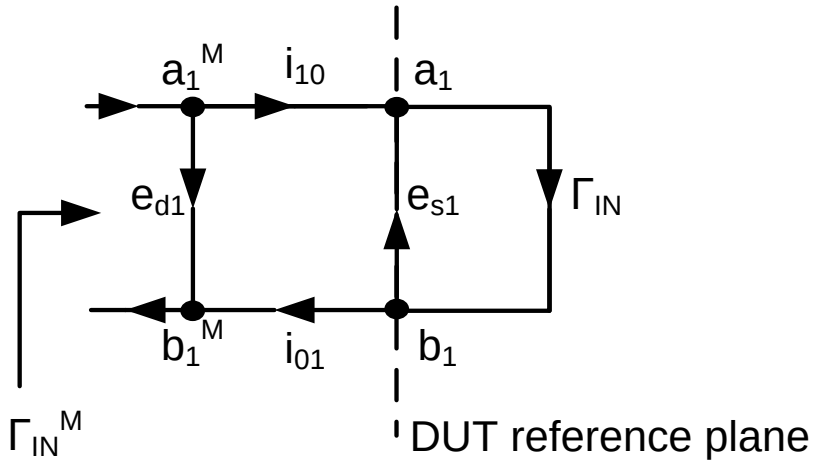

Figure 6.1: Error flow graph at the input port.

$$b_1 = \frac{b_1^M - e_{d1} \cdot a_1^M}{i_{01}} \ , \tag{6.6}$$

where $\Delta = e_{d1} \cdot e_{s1} - i_{01} \cdot i_{10}$.

The addition of an extra calibration step with a power meter [63] allows the calculation of the amplitude of the separate terms i_{01} and i_{10} from the product term $i_{01} \cdot i_{10}$, enabling the measurement of the absolute power of the a and b waves. Finally, when the phase information of the input and output signals are also required, an extra phase calibration step is needed to acquire the phase information of the i_{01} and i_{10} terms.

Traditionally two techniques can be employed to generate a signal to be used for a phase calibration:

- A comb generator (known as a phase reference) is stimulated with a low frequency tone (e.g., 10 MHz) to create a homogeneous multi-tone signal with known phase relationship between the tones [83, 84].

- An RF multi-sine is generated with known phase relations between the various sinusoids (e.g., by a wideband AWG or by means of up-conversion) and used as a reference signal [85].

In terms of hardware, the first systems capable of measuring time-domain waveforms started to appear in the late '80s. In the literature, mainly two techniques have been described:

- Measurement of the phases of different harmonic products of the periodic signal in the frequency domain with an extended VNA architecture.
- Sampling of the periodic waveform in the time-domain using sub-sampling techniques (e.g., sampling oscilloscope).

6.1.1 Waveform reconstruction with VNAs

As previously mentioned, a conventional VNA can only measure the ratio of power waves (i.e., reflection coefficients). This is not only related to calibration (only the product term $i_{01} \cdot i_{10}$ is known) as explained in the Section 6.1, but depends on the hardware capabilities of a network analyzer. When trying to extract the absolute phase information of the a and b waves, a conventional VNA is not capable of providing consistent values because the measured absolute phase at each frequency varies over time and over different acquisitions. This is due to the fact that the signal generated by the local oscillator synthesizer (LO), which is used to down-convert the measured signal, will have a different phase, in respect to a common reference, every time one of the different frequency components is measured. In order to understand this, a closer look must be given to the architecture of modern factional-N phased locked loops (PLL) which are employed in all commercial synthesizers. The output frequency (f_{VCO}) of a fractional-N PLL is a fractional portion of the reference frequency (f_R) and is given by $f_{VCO} = f_R \cdot (N + K/F)$, where N, K and F are integers [86]. Since the divider is changed in the loop dynamically, and multiple fractional solutions exist which yield the same output frequency, the phase of the output signal can change every time the same frequency is selected (i.e., returning to the same frequency after a sweep). Therefore, every time a signal at the same frequency is acquired, the local oscillator will have a different delay with respect to the RF signal to measure. As a consequence, the measured phase will vary at each acquisition, even if the phase of the signal has not changed.

In order to properly extract the phase information, it is necessary to modify the hardware to ratio all of the a and b waves (i.e., at fundamental and harmonics) against a reference signal (a_{ref}) containing all of the frequency components of interest (Fig. 6.2). This reference signal is created by feeding a low frequency component, coherent with the RF signal source used for the measurement, to a comb generator that creates all the harmonic products.

Finally, an additional phase calibration step has to be performed to calculate the phase of the i_{10} and i_{01} error terms in the error model.

A first implementation of this approach was proposed in 1989 [83]. Since then, several characterization setups have been developed based on this con-

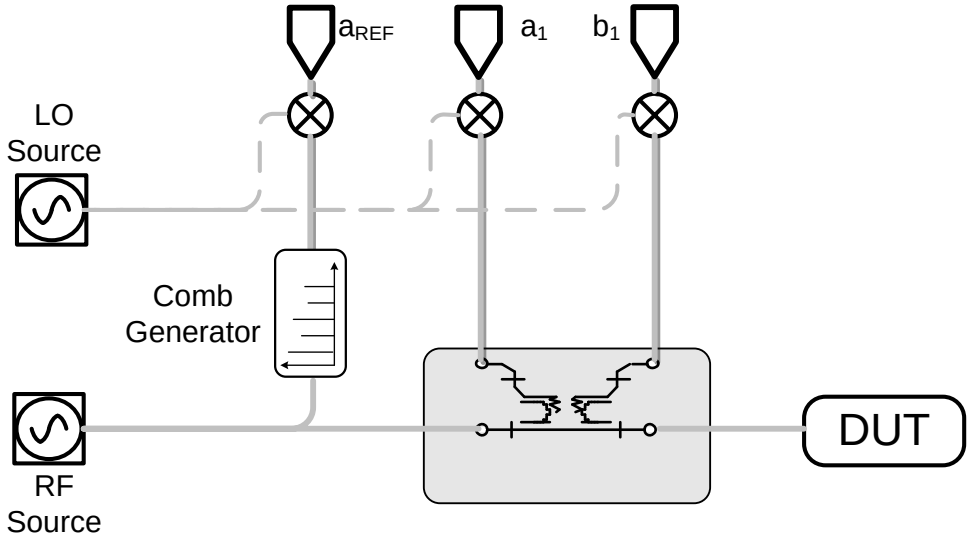

Figure 6.2: Simplified schematic of a VNA down-converting receiver. To measure the phase of a_1 and b_1, all spectral components must be ratioed against the reference signal a_{ref} created by the comb generator.

cept [81, 87, 88].

While this approach is relatively complex and requires stepping of the LO to measure all the harmonics of interest, it allows the use of high dynamic range receivers from conventional network analyzers (up to $\approx$ 120 - 130 dB).

6.1.2 Waveform reconstruction with sub-sampling techniques

In these systems a sampling oscilloscope or similar data acquisition instrument is used to acquire the time-domain traveling waves by sub-sampling the periodic waveform. The sub-sampling procedure creates a replica of the periodic waveforms at low frequency that can be acquired by A/D converters. The waves are first acquired in the time-domain, then transformed into the frequency domain where the additional phase calibration step is performed.

The first system to measure time-domain waveforms used a two channel sampling oscilloscope and was introduced in 1988 [89]. Successively more advanced systems [53, 90–93] based on commercial receivers such as the microwave transition analyzer (MTA) [94] and the large-signal network analyzer (LSNA) [95] appeared, coupling time-domain waveform analysis with load-pull capabilities.

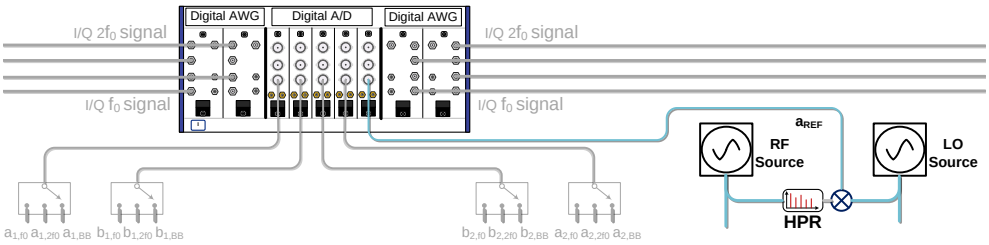

Figure 6.3: Simplified block diagram of the phase reference channel needed to enable waveform reconstruction in the mixed-signal load-pull system. Detail from Fig. 4.3.

In general, systems based on these kind of receivers are relatively simple since no reference channel is necessary. Furthermore, depending on the receiver used, they can be relatively fast since all the harmonics needed for the waveform reconstruction are acquired at once. However, their dynamic range is lower compared to the much more narrowband heterodyne architecture ($\approx$ 60 - 70 dB) due to the use of wideband samplers that also acquire a prominent amount of unwanted noise.

6.2 Waveform reconstruction on the mixed-signal load-pull system

The ability to measure time-domain waveforms combined with source and load-pull tuning capability is of the utmost importance when performing amplifier design or studying amplifier classes. In addition to the previously described features, the mixed-signal active load-pull system introduced in Chapters 4 and 5 also allows the extraction of time-domain waveform data. Since the system receiver is based on a super-heterodyne down-conversion scheme (similar to conventional VNAs) a reference channel is also required to keep track of the LO phase changes as described in Section 6.1.1. This is accomplished by driving a comb generator integrated inside the system with the CW RF source signal used in the IQ up-conversion block (Fig. 6.3).

In the following sections, the system phase measurement repeatability is presented. Then the phase reference specifications are discussed and the results for different comb generators are shown. Finally, an example of a class-B amplifier design on the mixed-signal load-pull system is provided as a working example of the setup's capabilities.

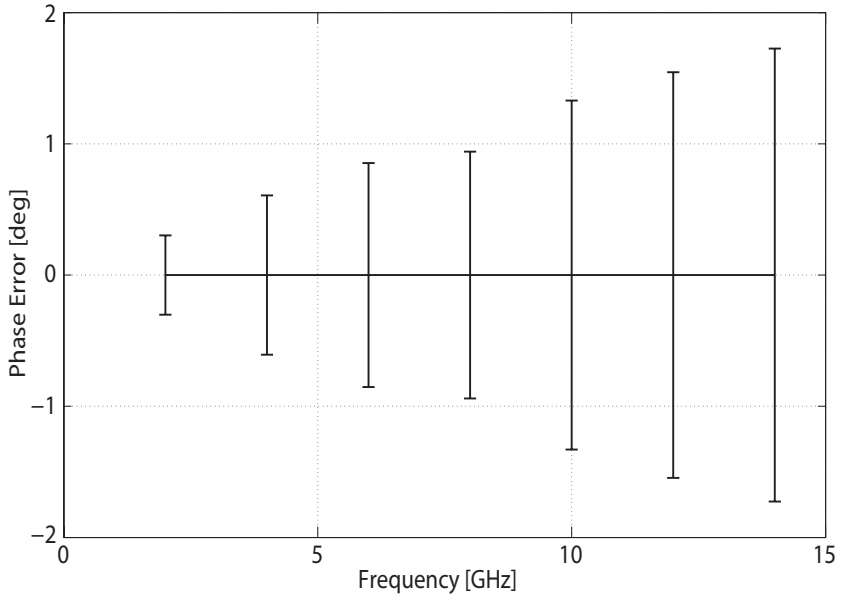

Figure 6.4: Standard deviation of the phase measurement of b_2 for the different measured harmonics.

6.2.1 System phase measurement repeatability

The phase measurement stability for the characterization system developed in this thesis is verified by performing 30 repeated measurements on a comb generator stimulated by a 2 GHz input signal, and by measuring the phase of the output traveling wave up to the 7^{th} harmonic. The measurements are performed with an acquisition time of 2 ms. The results are shown in Fig. 6.4, where the standard deviation of the phase measurement of b_2 is depicted for the different measured harmonics.

6.2.2 Phase reference specifications

As described in Section 6.1, a phase reference device with known phase relationship between the fundamental and harmonic components is required in order to calibrate the system for measuring time-domain waveforms. Such a device should work as a comb generator, or in other words, when stimulated with a sinusoidal signal at frequency f_0 it generates sufficient power at all of the harmonics of interest. The most common implementations of comb generators make use of high-speed diodes in shunt configurations [83] acting as

rectifiers, non-linear transmission lines [96, 97], or digital circuits generating very narrow pulses [98].

To use a comb generator as a phase calibration standard, the phase of the output wave of the comb generator is measured on a sampling scope calibrated with a nose-to-nose calibration [99], or by an electro-optical calibration [100]. This calibration is ideally done by a specialized institute (e.g., a national metrology institute). The resulting calibrated phase reference should be portable from one system to another. For this reason there is the requirement that it needs to be insensitive to a wide set of external conditions. In particular, it is essential that its behavior is independent of input power (in a sufficiently wide range), and source and loading conditions at the fundamental and harmonics, since these might change between the primary calibration of the unit and the one performed on the large-signal setup.

In this section, the performance of different commercially-available comb generators are evaluated as potential phase reference standards. The results of a new comb generator prototype developed during this thesis work are also presented for comparison. In particular, the phase stability of these devices versus power, and versus fundamental and second harmonic load is analyzed by measuring the phase of the b_2-wave while sweeping the input power and performing fundamental and second harmonic load-pull. In all of the following experiments a fundamental frequency of 2 GHz is used and 7 harmonics are measured.

Marki A-0030 square-wave amplifier

First, a Marki Microwave A-0030 saturated amplifier is evaluated s a phase reference standard. This particular model is an overdriven double-stage traveling wave amplifier working from 5 MHz to 30 GHz, which generates a square wave. The output spectrum of the amplifier is shown in Fig. 6.5, where it can be seen that the output power of each spectral tone is sufficiently high up to the 6^{th} harmonic.

Fig. 6.6 shows the phase variation of the b_2-wave versus input power. Due to the large phase variation of b_2 versus power, the use of this device as a phase calibration standard would require the knowledge of the absolute input power provided to the amplifier in both the characterization and calibration phases. Furthermore, Fig. 6.7 and Fig. 6.8 show the phase variation versus fundamental and 2^{nd} harmonic output impedance up to a $|\Gamma| = 0.3$. The very large variation versus load makes it impossible to transfer this amplifier together with its phase calibration information from one setup to the other without losing measurement accuracy. For these reasons such a device is clearly not suitable to be used as a phase standard.

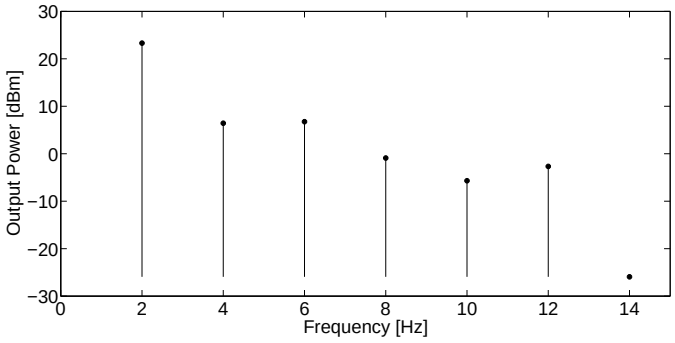

Figure 6.5: Output power spectrum of a Marki A-0030 amplifier.

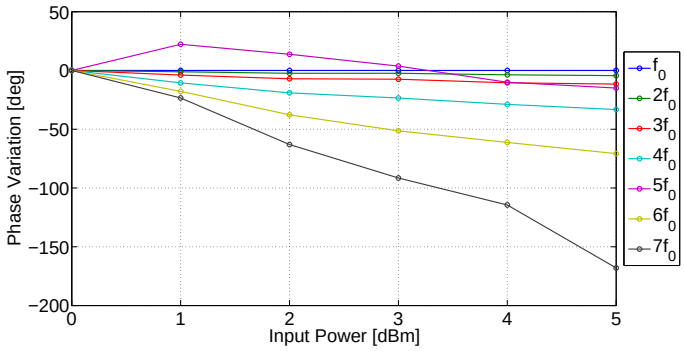

Figure 6.6: b_2 phase variation for the different harmonics versus input power for a Marki A-0030 amplifier.

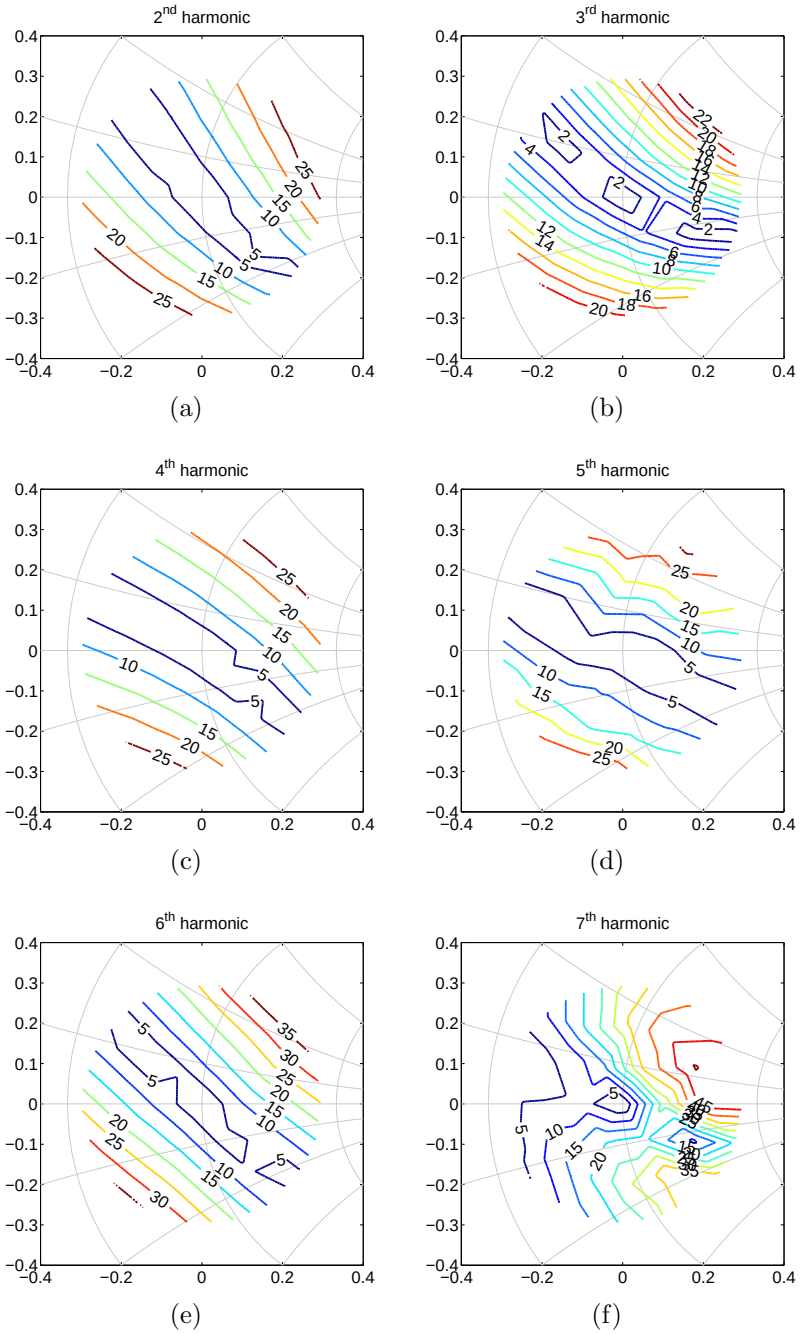

Figure 6.7: b_2 phase variation of a Marki A-0030 amplifier vs. fundamental output load Γ at: (a) 2^{nd} harmonic, (b) 3^{rd} harmonic, (c) 4^{th} harmonic, (d) 5^{th} harmonic, (e) 6^{th} harmonic, (f) 7^{th} harmonic.

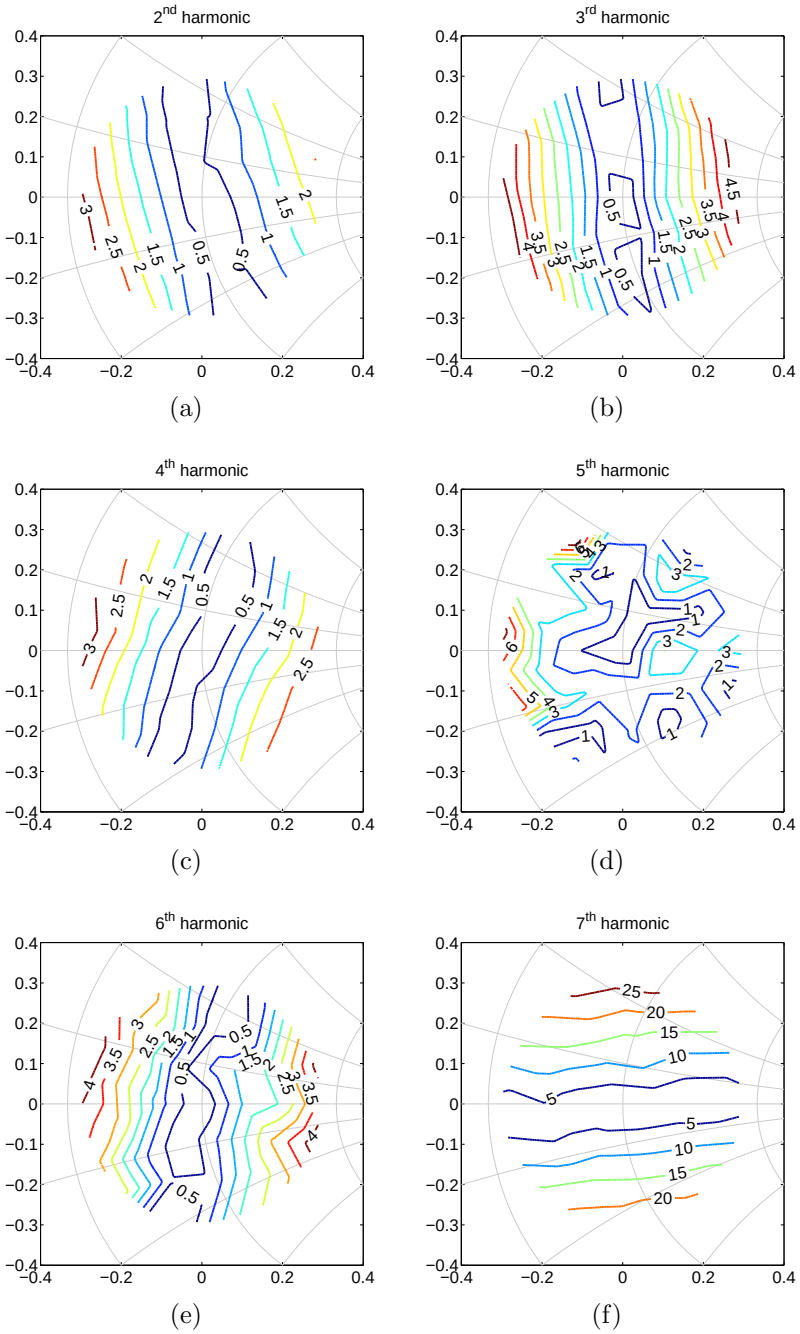

Figure 6.8: b_2 phase variation of a Marki A-0030 amplifier vs. 2^{nd} harmonic output load Γ at: (a) 2^{nd} harmonic, (b) 3^{rd} harmonic, (c) 4^{th} harmonic, (d) 5^{th} harmonic, (e) 6^{th} harmonic, (f) 7^{th} harmonic.

HHFT MD-CG1 comb generator

A commercial comb generator implemented with a digital circuit was also evaluated. The output spectrum for this component is shown in Fig. 6.9, which shows that the higher harmonic power levels of this module are sufficiently high. The b_2 phase variation versus input power (shown in Fig. 6.10) for this comb generator is much lower in comparison to the previously described nonlinear amplifier, although the higher harmonics phase variation versus power is still significant. Moreover, as shown in Fig. 6.11, the phase variation versus fundamental load impedance is still considerably large, and would result in a high phase measurement uncertainty when using such a device as calibration standard. The variation versus 2^{nd} harmonic load impedance (shown in Fig. 6.12) is much more contained in this case (below 5 to 6 degrees) and is acceptable.

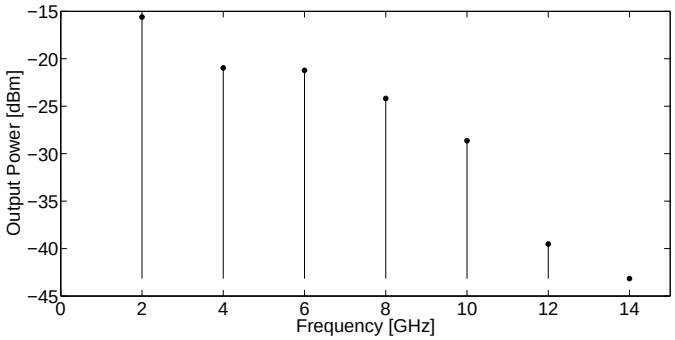

Figure 6.9: Output power spectrum of a HHFT MD-CG1 comb generator.

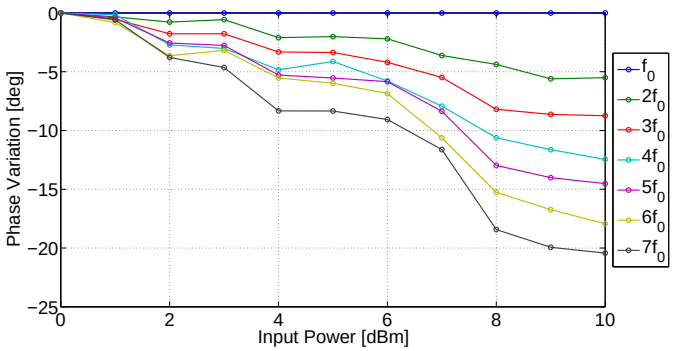

Figure 6.10: b_2 phase variation for the different harmonics versus power for a HHFT MD-CG1 comb generator.

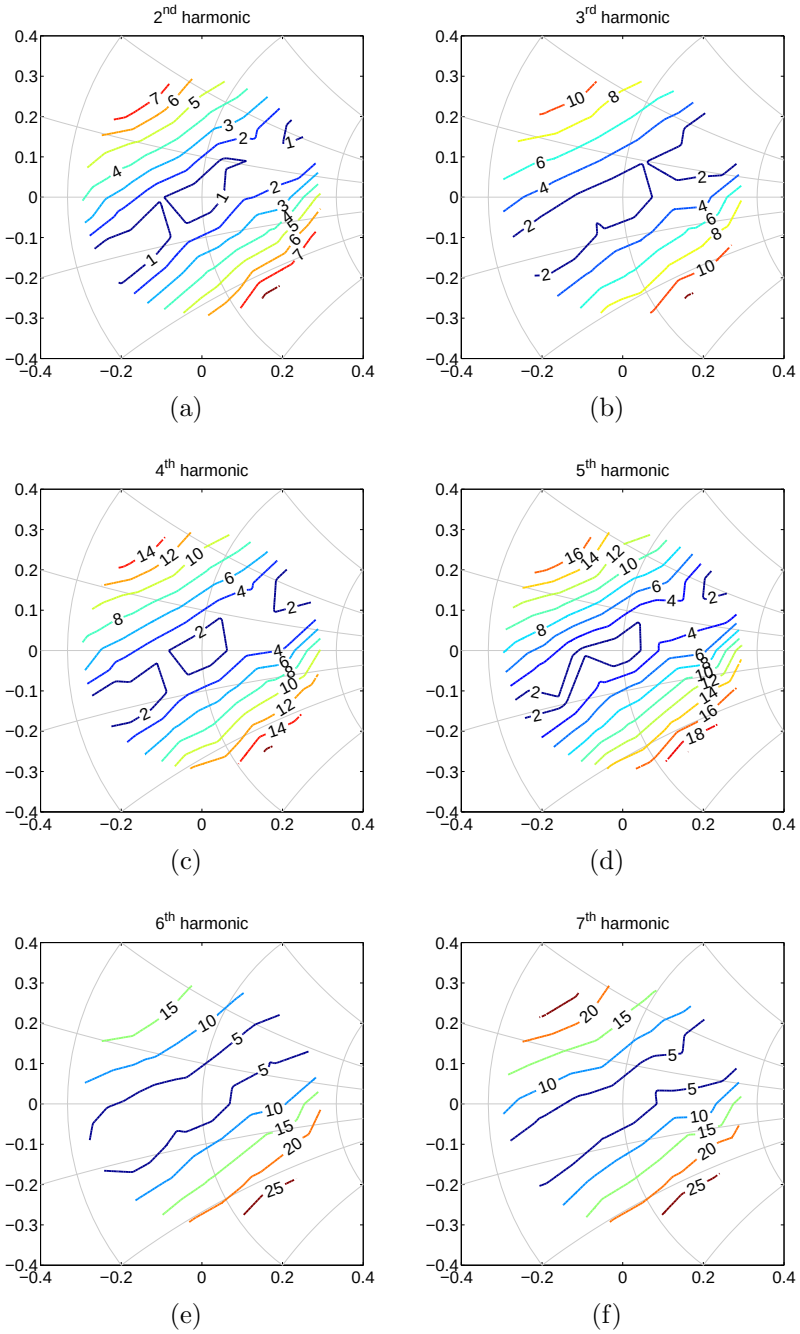

Figure 6.11: b_2 phase variation of a HHFT MD-CG1 comb generator vs. fundamental output load Γ at: (a) 2^{nd} harmonic, (b) 3^{rd} harmonic, (c) 4^{th} harmonic, (d) 5^{th} harmonic, (e) 6^{th} harmonic, (f) 7^{th} harmonic.

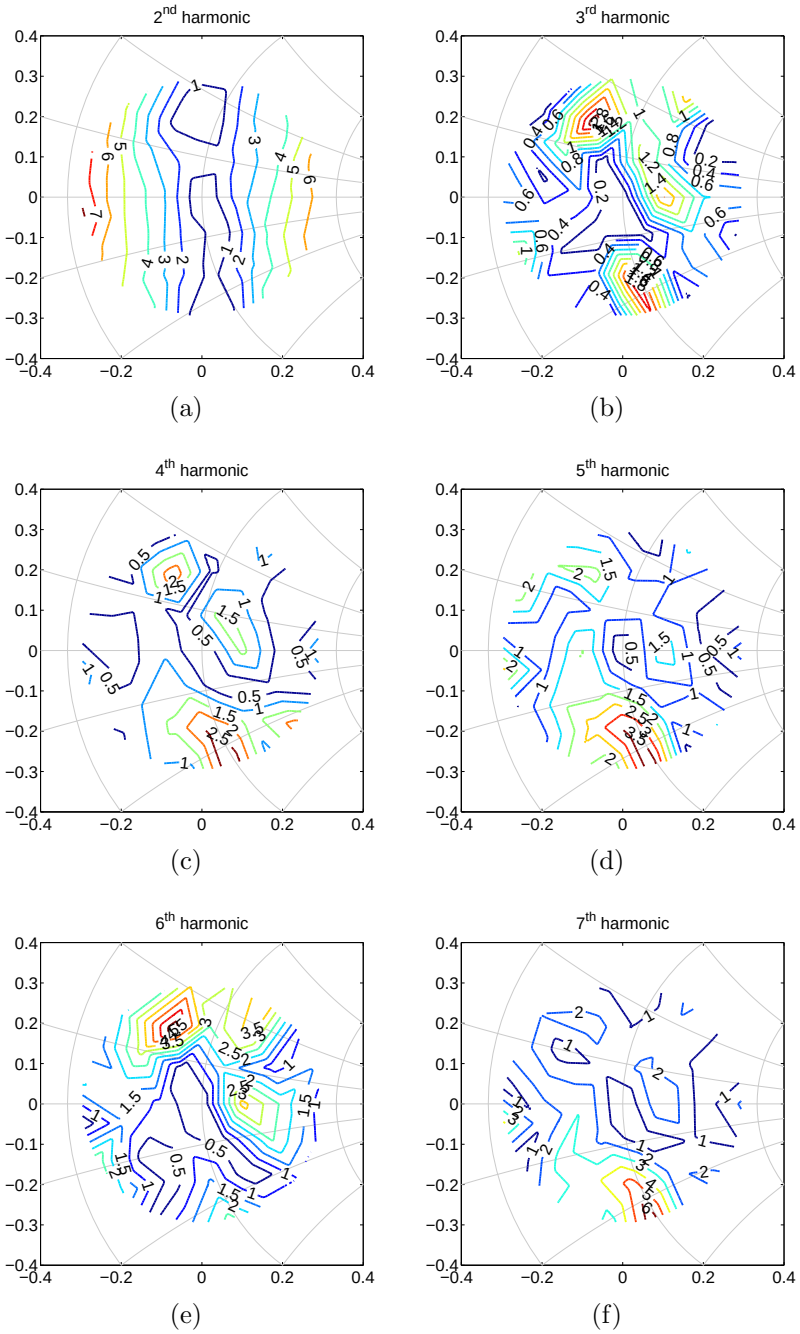

Figure 6.12: b_2 phase variation of a HHFT MD-CG1 comb generator vs. 2^{nd} harmonic output load Γ at: (a) 2^{nd} harmonic, (b) 3^{rd} harmonic, (c) 4^{th} harmonic, (d) 5^{th} harmonic, (e) 6^{th} harmonic, (f) 7^{th} harmonic.

New comb generator concept

A new comb generator concept has been realized during this thesis work by combining several commercially-available components in order to minimize the phase variation of the b_2 output wave versus input power and loading impedance terminations. The output spectrum of the implemented prototype is shown in Fig. 6.13. Fig. 6.14 shows the phase variation versus power of the implemented comb generator, while Fig. 6.15 and 6.16 show the b_2 phase variation versus fundamental and 2^{nd} harmonic load impedances, respectively. These results clearly show that the realized prototype is very insensitive to input power and changing loading conditions, making this new comb generator an excellent candidate for being used as a phase reference standard.

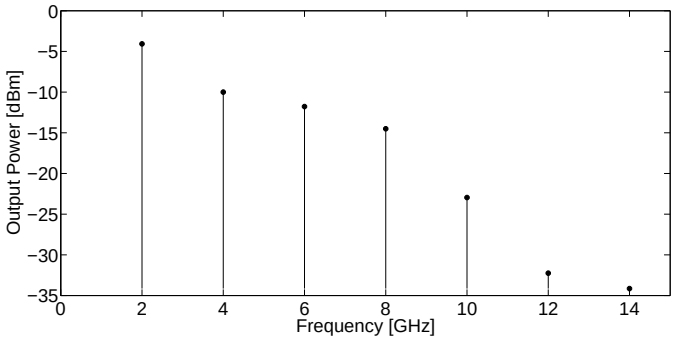

Figure 6.13: Output Power Spectrum of the new comb generator prototype.

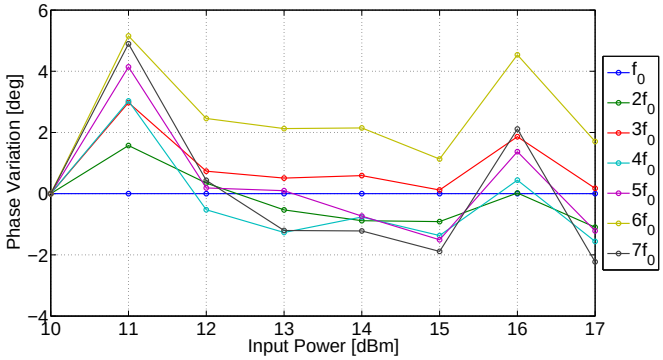

Figure 6.14: b_2 phase variation for the different harmonics versus power for the new comb generator prototype.

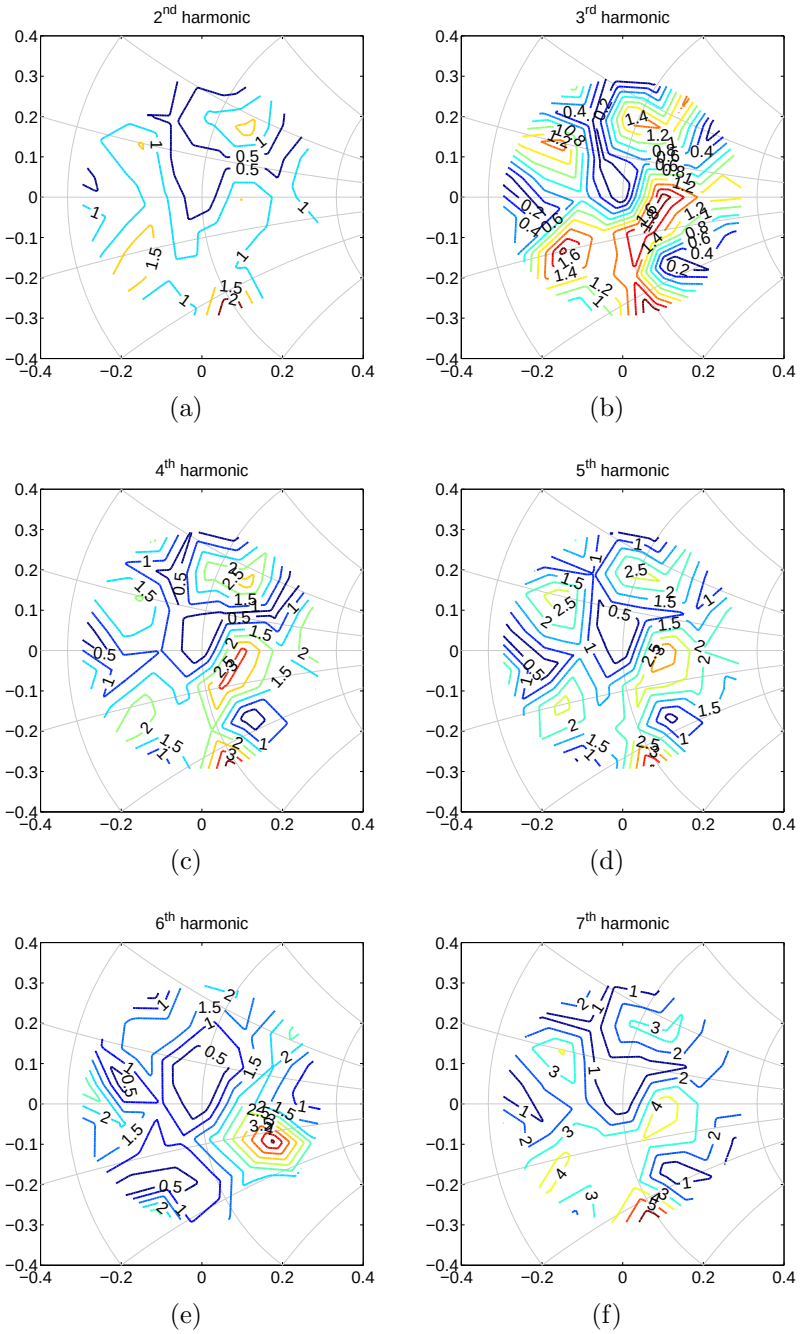

Figure 6.15: b_2 phase variation of the new comb generator prototype vs. fundamental output load Γ at: (a) 2^{nd} harmonic, (b) 3^{rd} harmonic, (c) 4^{th} harmonic, (d) 5^{th} harmonic, (e) 6^{th} harmonic, (f) 7^{th} harmonic.

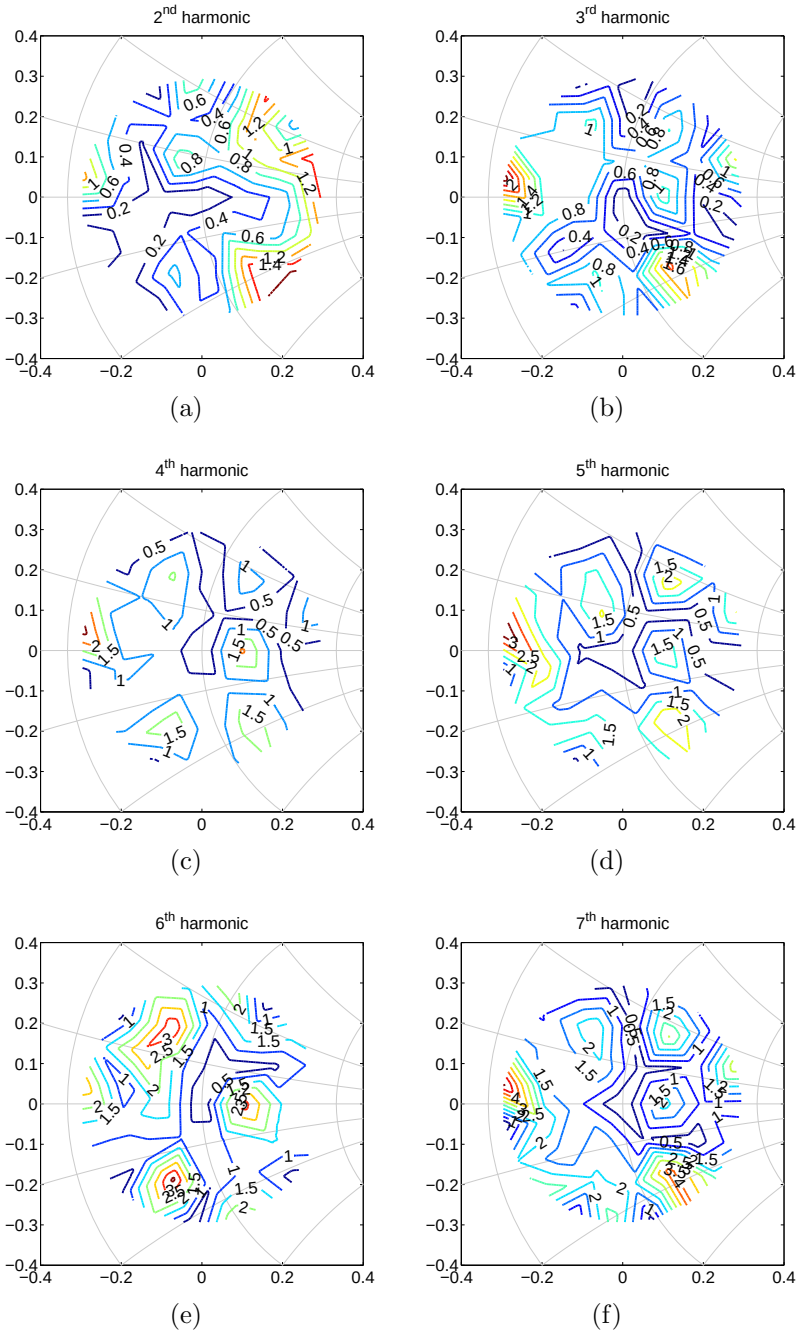

Figure 6.16: b_2 phase variation of the new comb generator vs. 2^{nd} harmonic output load Γ at: (a) 2^{nd} harmonic, (b) 3^{rd} harmonic, (c) 4^{th} harmonic, (d) 5^{th} harmonic, (e) 6^{th} harmonic, (f) 7^{th} harmonic.

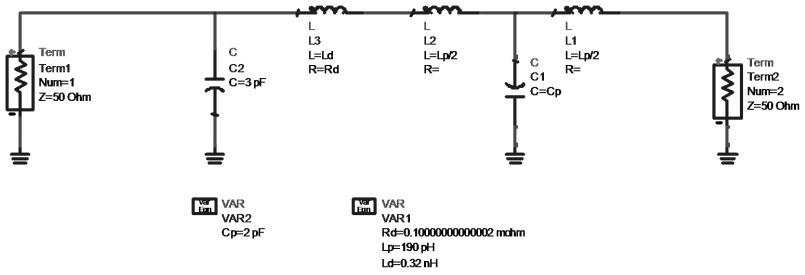

Figure 6.17: Package, bond wires and output capacitance de-embedding for the GaN HEMT with $W_g = 12$ mm.

6.2.3 Measurement example

The system capability to measure time-domain waveforms is demonstrated by the example of a 50 W-rated, packaged NXP GaN HEMT with a gate width of 12 mm measured under class-B operation at a frequency f_0 of 2 GHz.

In order to get insightful time-domain waveform data similar to what is commonly shown in textbook discussions of power amplifiers [15], it is necessary to monitor the voltage and current waveforms at the level of the device intrinsic current generator, that is the device internal drain node. For this reason, de-embedding of the package, bond wires, and the device output capacitance are needed. The simple model used for this de-embedding is shown in Fig. 6.17. Although the output capacitance is non-linear, and as such has a strong dependence on the output voltage, the de-embedding approach in this work is kept simple and assumes a 3 pF linear capacitor. More sophisticated approaches using non-linear de-embedding techniques [101] could also be implemented.

The device under test is biased at V_{DD} of 50 V with a quiescent current I_{DQ} of 150 mA. To load-pull the DUT into class-B operation, the fundamental load impedance termination is controlled over several values (ranging from 15 to 40 Ω, real), while the second harmonic input and output terminations are fixed at a short condition. The time-domain waveforms are reconstructed from the measurement of 5 harmonic waves in this particular case. The resulting waveforms are shown in Fig. 6.18, where the dynamic load-line for different resistive fundamental loading conditions are given at 6 dB input power back-off with respect to the 2 dB power-gain-compression point. The classical sinusoidal voltage waveform and the half-rectified sine-wave current waveform can be observed in Fig. 6.18a and 6.18c.

Finally, the voltage and current waveforms are plotted as a function of

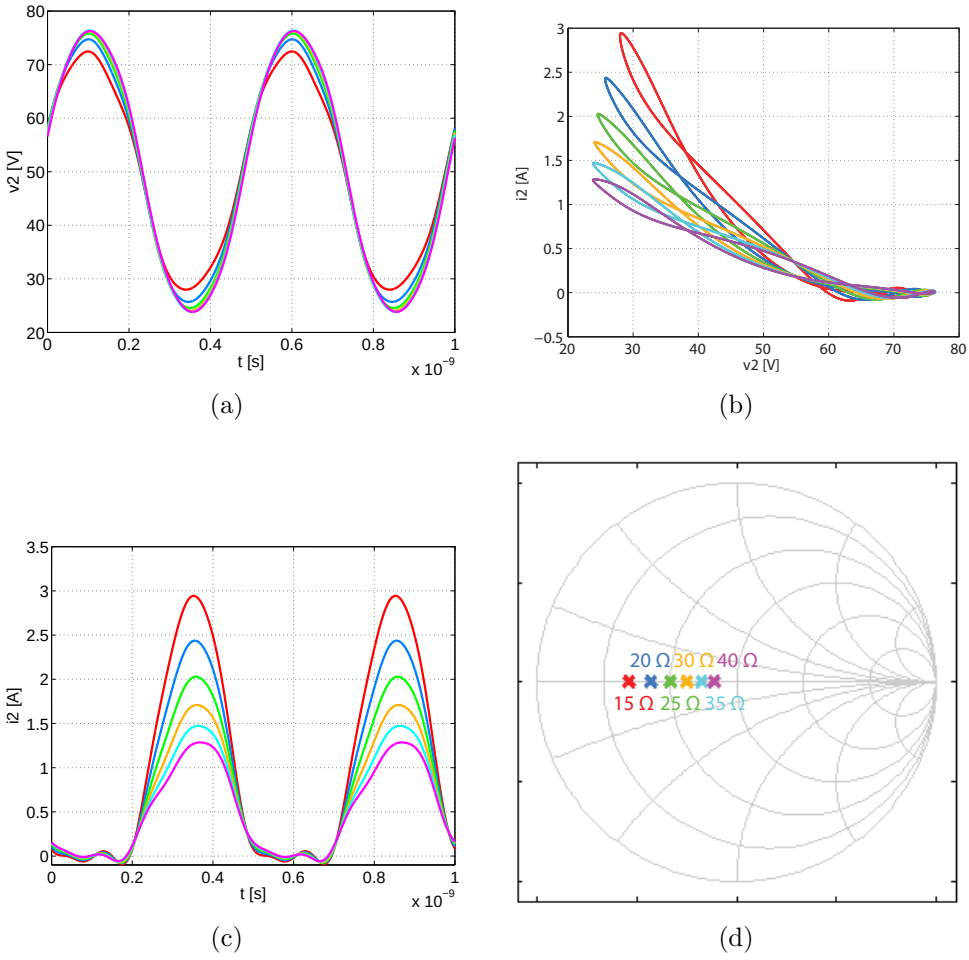

Figure 6.18: (a) Voltage (V_{DS}) time-domain waveform measured at the device internal drain node (current generator plane) without output capacitance and bond-wire connections of a 50 W GaN HEMT for different resistive fundamental loading terminations. Each color corresponds to a fundamental loading termination of Fig. 6.18d. (b) Dynamic load line plotted for different resistive fundamental loading terminations. (c) Current (I_D) time-domain waveform measured at the output current generator of the DUT for different resistive fundamental loading terminations. (d) Fundamental loading terminations provided to the DUT.

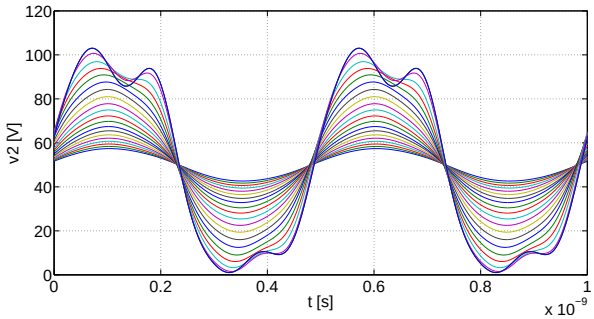

(a)

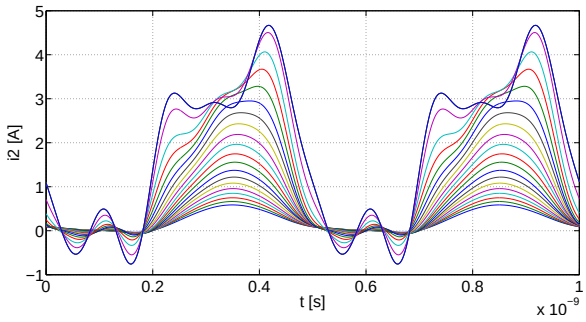

(b)

Figure 6.19: (a) Voltage (V_{DS}) and (b) current (I_D) time-domain waveforms measured as a function of power at the output current generator of the DUT for a fundamental loading termination of 25 Ω. The source available power (P_{AVS}) is swept from 15 dBm to 37 dBm in 1 dB steps.

power for a fundamental loading impedance of 25 Ω in Fig. 6.19. In this example it is easy to see how the peak voltage approaches $2 \cdot V_{DD}$ (the theoretical value for class B) before the DUT becomes overdriven. From these measurements we can also note that there are ripples in the current waveform which are reaching even negative values. Initial experiments using a simulator with a detailed compact model of the GaN device indicate that the use of non-linear de-embedding techniques can remove these effects.

6.3 Waveform reconstruction for closely–spaced multi-tone signals

In the characterization and optimization of non-linear devices, it is often required to excite the device with complex modulated signals (e.g., W-CDMA, IEEE 802.11, etc.). In practical test conditions these signals are represented using a large number of closely spaced sinusoids [102] with amplitude and phase set to mimic the cumulative distribution function (CDF) of the communication standard under consideration correctly.

As mentioned in Section 6.1, two methods are commonly used when performing a phase calibration, and both of them exhibit severe limitations when a large frequency range (e.g., from fundamental up to the 7^{th} harmonic) is required in combination with a narrow tone spacing (e.g., below 10 MHz). When using an AWG, the AWG bandwidth typically limits the number of harmonics covered, while its memory depth restricts the minimum tone spacing that it can provide. When considering the homogeneous grid method, the phase reference needs to be stimulated at a very low frequency in order to create a sufficiently dense frequency grid. Due to the limited output power capabilities of the phase reference and the large number of frequency tones generated, the power per tone will be significantly reduced at higher frequencies. Moreover, the phase error arising when measuring these tones (due to phase noise / jitter multiplication) increases.

In the following sections, a novel phase calibration procedure is proposed which facilitates wideband phase calibration of non-linear VNAs (NVNAs) when employing closely spaced tones. At the same time, the proposed method has the advantage that it reduces the maximum order of harmonic components generated by the phase reference, resulting in an increased power per tone and a reduced phase error.

6.3.1 System description

The hardware configuration used in this work is based on an Agilent N5242A PNA-X platform. However, the proposed solution is general and can be employed on any NVNA platform, including the one described in Chapters 4 and 5. A block diagram of the extended hardware configuration is given in Fig. 6.20. In the proposed approach, a Marki A-0030 square-wave amplifier is used to generate the static cross-frequency phase relations. These are needed to keep track of the phase changes when stepping the local oscillator (LO) of the PNA. The calibration harmonic phase reference (cHPR) is a calibrated Agilent U9391C unit [103], which is capable of providing the calibrated cross-

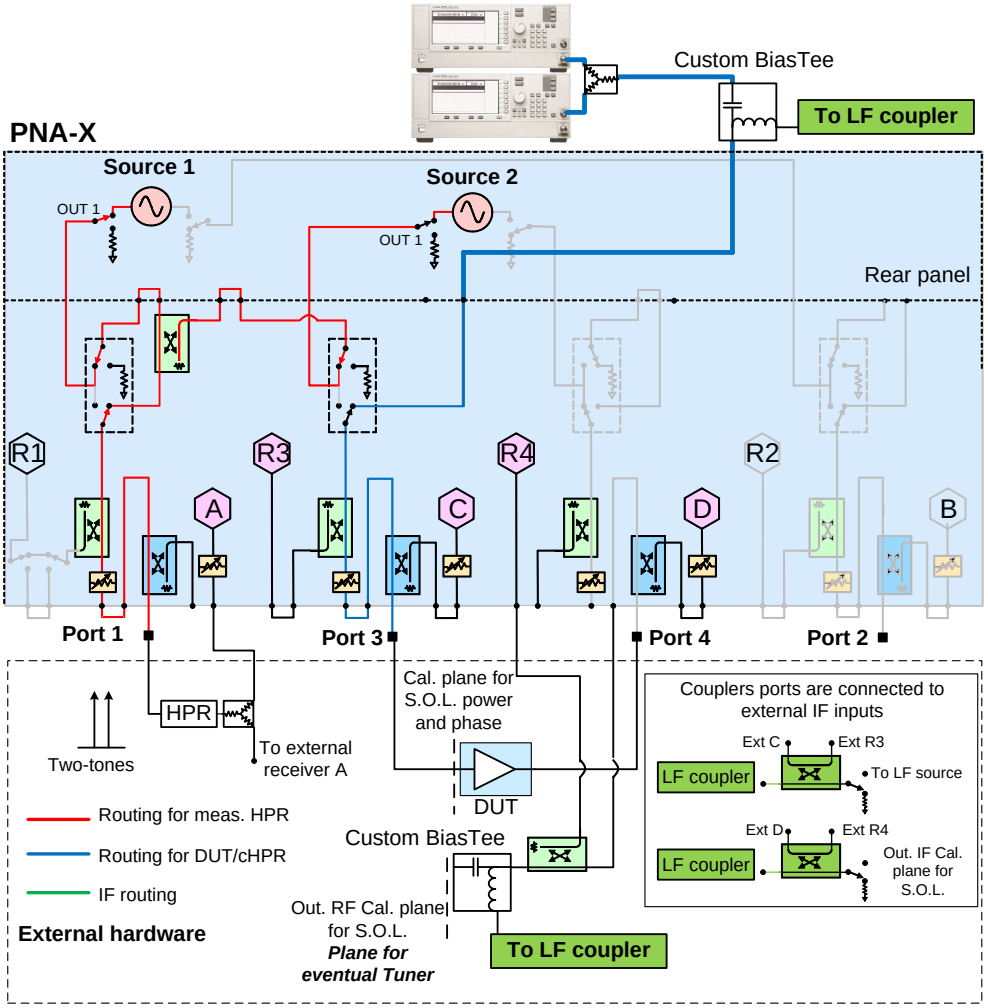

Figure 6.20: Simplified block diagram of the system, where HPR is the harmonic phase reference (e.g., square-wave amplifier), and cHPR is the calibration harmonic phase reference (e.g., Agilent U9391C).

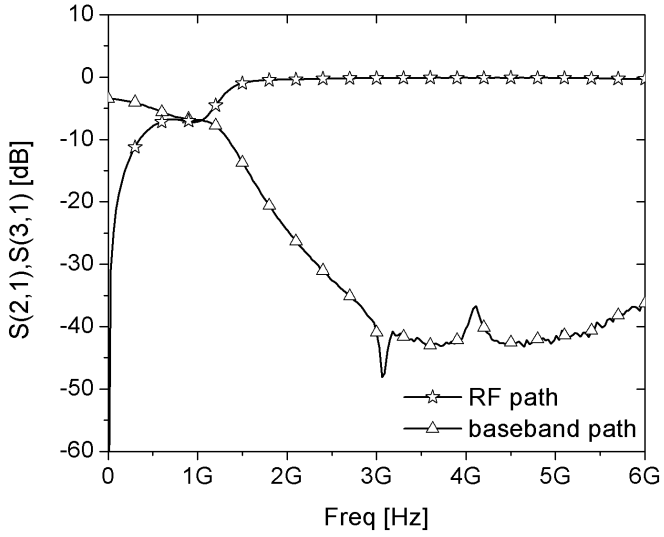

Figure 6.21: Measured S_{21} and S_{31} of the custom bias-Tee representing the RF path and baseband path, respectively.

frequency phase relations at the desired reference plane of the device under test (DUT).

The hardware of the PNA-X is designed to work in the frequency band ranging from 10 MHz to 26.5 GHz. When exciting a non-linear device with a multi-tone signal, intermodulation products will appear in the high frequency band (e.g., $2f_1$, $3f_1$, etc.) as well as in the baseband (e.g., $f_2 - f_1$, etc.). When the stimulus is composed of closely-spaced multi-tones, the baseband components will appear at frequencies below the PNA-X detection band. For this reason, external hardware is required to properly sample these waves in order to support correct waveform reconstruction for the overall signal. In the proposed setup the a and b baseband waves (e.g., below 10 MHz) are sensed using external low-frequency bridges (e.g., Minicircuits ZFDC-10-6).

The resulting coupled waves are then routed directly to the wideband A/D converter (e.g., 16 MHz) of the PNA-X. Custom designed bias-Tees are employed to separate the low-frequency components (e.g., below 100 MHz) from the high frequency components (e.g., above 1.5 GHz), because the low frequency bridges would present too high loss for the high frequency components above 10 MHz. Fig. 6.21 shows the measured transmission parameters for both the RF and baseband path of the bias-Tees.

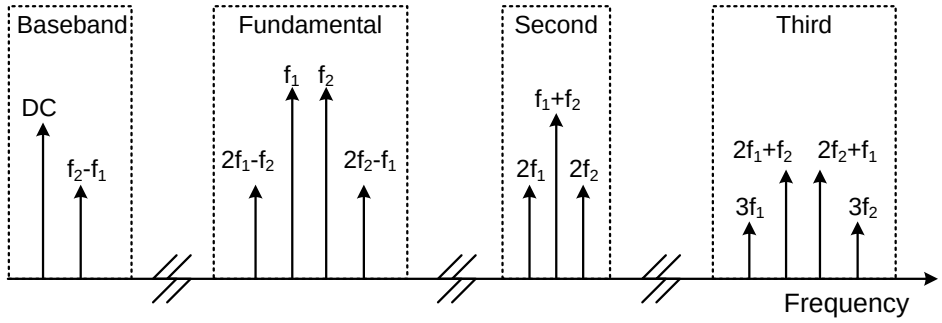

Figure 6.22: Frequency list selected by the user, based on harmonic order (H) and intermodulation order (M). In this figure H=3 and M=3.

6.3.2 Phase calibration

In the proposed approach, the measurement frequency grid (referred as intermodulation grid) is generated based on the desired tone spacing, the harmonic order and the intermodulation order, as shown in Fig. 6.22 (e.g., as in a harmonic balance simulator). The two-tones at frequencies f_1 and f_2 are applied simultaneously to the non-linear device used as the measurement HPR, which will generate all the intermodulation products needed for reference, as shown in Fig 6.20. Note that these tones will be constantly applied to the HPR during both calibration and measurements, and are used to "keep track" of the phase change when the local oscillator is stepped to measure the various frequency components. The same frequencies (e.g., f_1 and f_2) will also be applied to the DUT during measurements using external sources (e.g., E8257D PSG, see Fig. 6.20). The phase calibration procedure is then divided in two main steps, as outlined in the following two subsections.

1. First step

A single-tone at baseband frequency $f_{in} = f_2 - f_1$ is applied to the calibration harmonic phase reference (cHPR), generating a homogeneous grid at the output of the cHPR (Fig. 6.23). The first step of the phase calibration (e.g., the extraction of the phase component of the i_{10} error term [63]) is performed up to the highest tone in the fundamental band of the selected frequency grid (e.g., $2f_2 - f_1$ in Fig. 6.22). Note that the phase calibration will give correct results only for the frequency components which are also generated by the measurement harmonic phase reference generator (e.g., spectral components of Fig. 6.22). For all of the other frequency components, the data are discarded.

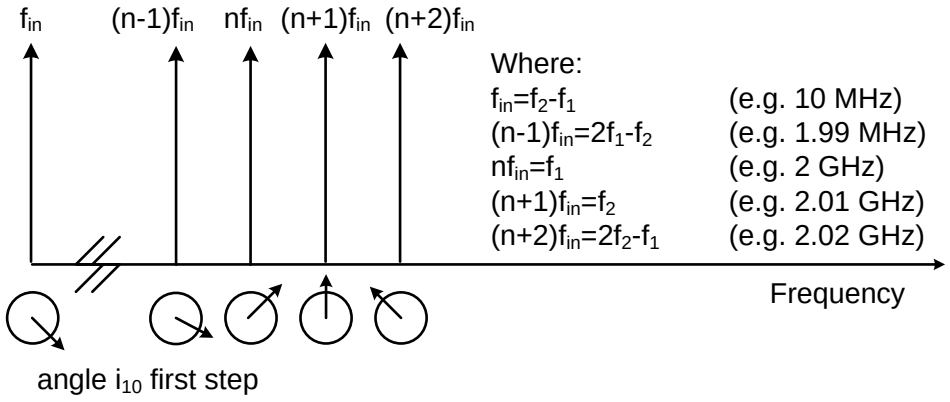

Figure 6.23: Frequency grid generated by the calibration HPR during the first step of the calibration procedure.

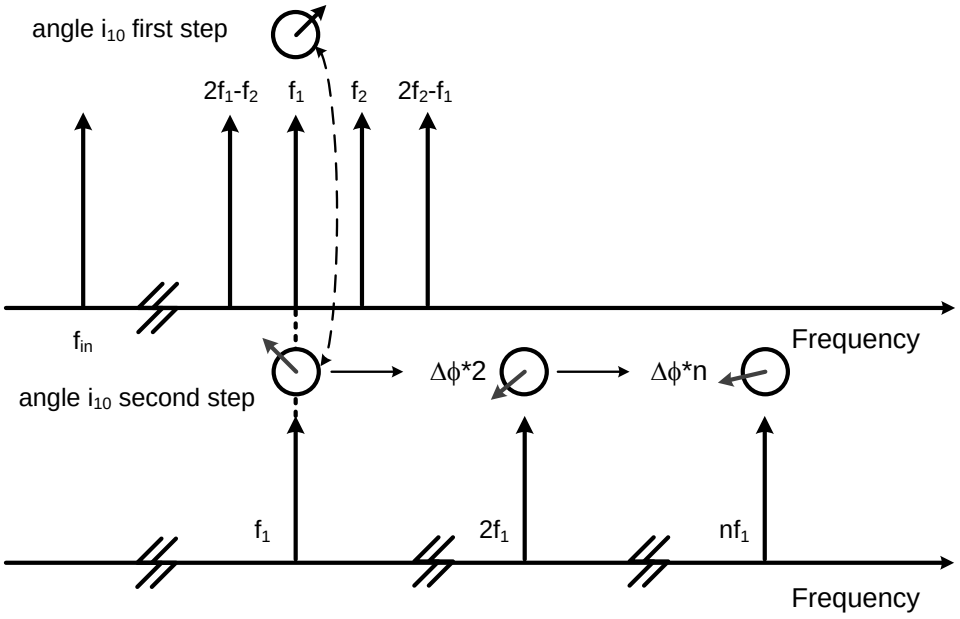

Figure 6.24: Alignment of the error terms measured in the second step to the correspondent frequency components measured during the first step of the phase calibration procedure.

2. Second step

During the second step, a single-tone is applied to the input of the cHPR at frequency f_1 in the fundamental frequency band. At this stage, the phase of the error terms (e.g., i_{10}) is acquired for all of the harmonic components of f_1, up to the highest frequency selected in the user-defined frequency grid (e.g., 3^{rd} harmonic in Fig. 6.22), with the upper limit being the bandwidth of the instrument.

The phase of the error terms acquired during this second step will not be consistent with the result of the first step (Fig. 6.24), since a new tone is now applied to the phase reference that is not coherent with the stimulus of the first step (e.g., $f_2 - f_1$). By comparing the phase of the i_{10} error term obtained in the second step with the one measured in the first step, the phase offset to be applied to all the error terms measured in the second step can be calculated, as shown in Fig. 6.24.

This procedure is repeated when applying a new tone at f_2. In this way, the phases of the error terms measured in the successive steps can be "aligned" with the ones measured during the first calibration step. The result is a consistent set of error terms for all the frequency components of interest. Note that the phases of the error terms for the frequency components that cannot be generated as an integer multiple of the tones present in the fundamental frequency band (e.g., f_1+f_2), are obtained via interpolation to the neighboring components. This completes the calibration procedure, allowing the measurement of corrected power waves at the input and output of the DUT for the entire (user-defined) frequency grid, including the baseband components.

6.3.3 Phase stability results

The proposed calibration procedure achieves better measurement phase accuracy for the following reasons:

1. Higher tone power for the higher-order harmonics.

2. Lower phase noise and jitter of the spectral components generated, due to the lower multiplication order.

To illustrate the improved phase measurement accuracy, a direct phase comparison of raw waves is made between the proposed method and the traditional homogeneous grid method.

The proposed method uses the two internal PNA-X signal sources to drive both the measurement HPR as well as the DUT (e.g., a Minicircuits 2x multiplier, ZX90-2-50-S+) via a power divider. This avoids the use of external

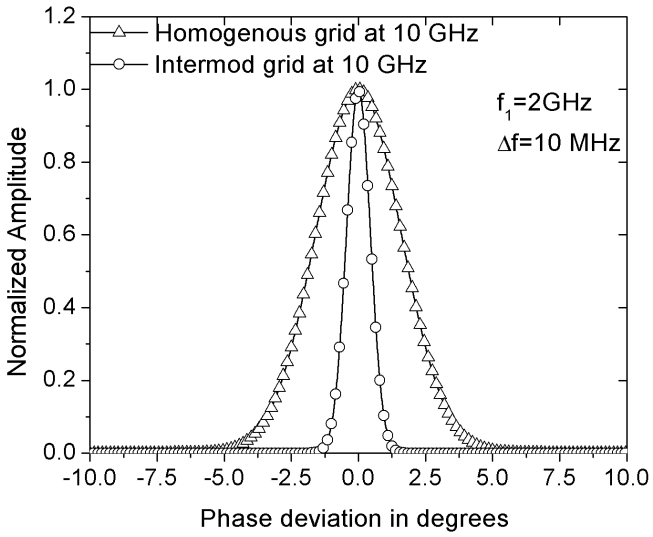

(a)

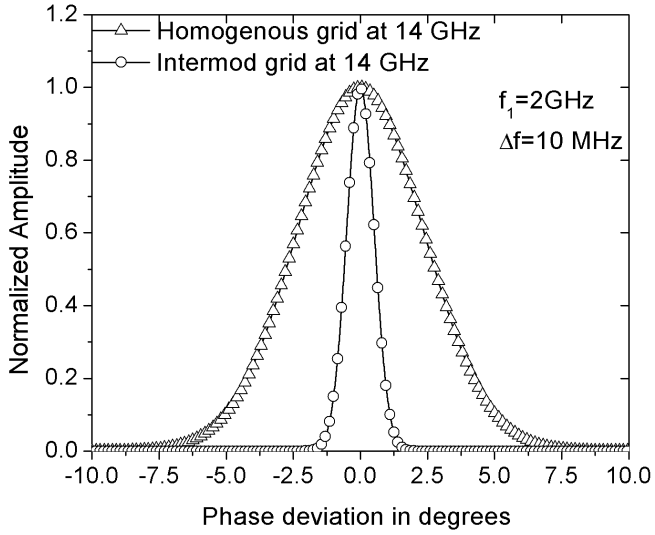

(b)

Figure 6.25: Comparison of normalized amplitude and mean Gaussian distribution based on the measured standard deviation of the phase of the b_2 wave using the two methods: a) measurement at 10 GHz (5^{th} harmonic), b) measurement at 14 GHz (7^{th} harmonic).

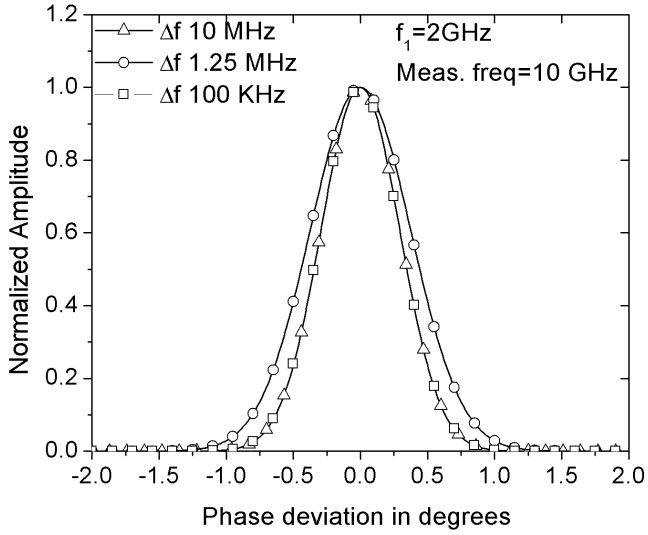

Figure 6.26: Comparison of normalized amplitude and mean Gaussian distribution based on the measured standard deviation of the b_2 phase using the new method for different Δf tones: 10 MHz, 1.25 MHz and 100 KHz.

sources which phase drift over time. In the homogeneous grid measurement setup, the 10 MHz reference of the PNA-X is used to drive the Agilent U9391C phase reference, while the two internal sources of the PNA-X drive the DUT. Note that the 10 MHz reference is phase locked with the internal signal sources and has very low phase noise, providing maximum output power for all of the harmonics generated by the U9391C phase reference.

By measuring the phase of the input/output waves (e.g., b_1/b_2) 100 times, the standard deviation is computed and a Gaussian distribution (with normalized mean and amplitude) is used to compare the data. Fig. 6.25 shows the results of the two methods, assuming a Δf of 10 MHz and the f_1 tone at 2 GHz in both cases. In Fig. 6.25a, the measured phase variation is shown at the 5^{th} harmonic (10 GHz), while Fig 6.25b shows the measured results for the 7^{th} harmonic (14 GHz). As shown in these figures, the phase variation of the homogeneous grid method rises with increasing harmonic order, while the proposed method provides a constant phase deviation. Finally, the phase deviation is shown in Fig. 6.26 for the new method when measuring the 5^{th} harmonic of a two-tone signal with f_1 equal to 2 GHz when the applied tone

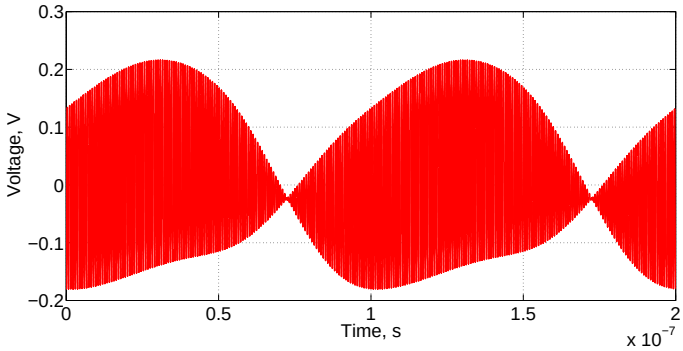

(a)

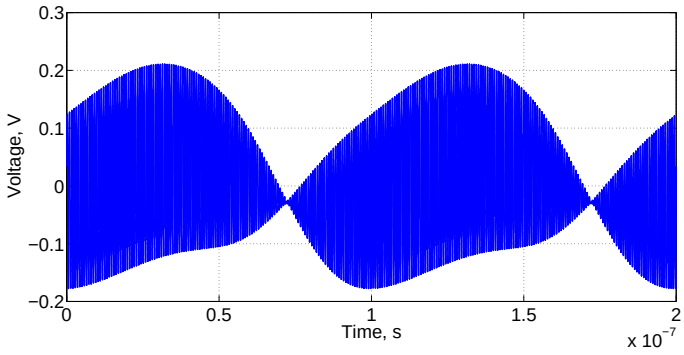

(b)

Figure 6.27: time-domain waveform of the b_2 wave measured for the square wave LO amplifier, a) multi-step calibration procedure b) PNA-X hardware and conventional calibration.

spacing is 10 MHz, 1.25 MHz and 100 kHz. As expected, the accuracy of the phase measurement does not reduce at narrower tone spacings, as would happen for the homogeneous grid method.

6.3.4 Waveform reconstruction

To validate the multi-step phase calibration procedure, the waveform of a square-wave amplifier (e.g., Marki Microwave A-0010) was measured and compared with the data obtained using the PNA-X NVNA software employing the homogeneous grid approach, Fig. 6.27.

As can be seen clearly, there is good agreement between the two results. In this experiment the frequency of the two carriers is 1.34 GHz and 1.35 GHz (the 10 MHz frequency grid is required for comparison with the PNA-X software and hardware). This proves that the proposed calibration procedure provides results consistent with the conventional, well-established, homogeneous grid phase calibration procedure.

6.4 Conclusions

In this chapter extensions to the mixed-signal active load-pull system that allow time-domain waveform measurements have been discussed. The requirements and the performance of commercially-available phase references and of a newly-developed prototype have been presented. Finally, an approach for time-domain waveform analysis dedicated to multi-tone signals closely spaced in frequency has been introduced.

Chapter 7

Application Examples

In the previous chapters of this thesis, an innovative load-pull system has been proposed. In this chapter, several examples of applications that highlight the most unique capabilities of the system are presented.

7.1 Out-of-band linearity optimization

The demand for higher data rates in communication systems has led to the introduction of 3G and 4G communication standards over the past decade, which make use of higher bandwidths and greater peak-to-average ratios. At the same time, there is an increased need, based on cost and logistic considerations, to handle multiple communication channels over a single transmit / receive chain. These trends require that the underlying hardware must be very linear over a large frequency span and power range to avoid channel-to-channel interference and EVM degradation. Combined with the ever-present need for higher efficiencies, these demands have driven the optimization of power devices.

From theory based on Volterra series analysis [104], it can be seen that two kinds of third-order mixing products are present in an active circuit. They are the direct 3^{rd} order product, and the indirect IM_3 mixing product resulting from secondary mixing between the fundamental signal and the IM_2 products at baseband and 2^{nd} harmonic. These two components can add constructively or cancel, determining the device linearity.

This effect is illustrated in Fig. 7.1 for the case of a complex modulated signal. Since this secondary mixing process is influenced by the baseband and 2^{nd} harmonic impedances, control at the device terminals is not only required in the fundamental band, but also in the baseband and in the 2^{nd} harmonic

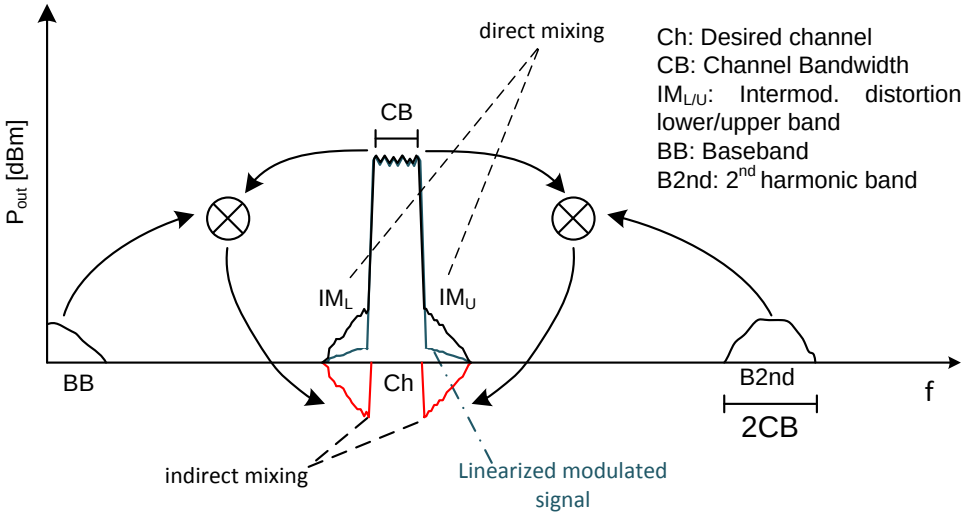

Figure 7.1: Basic principle of the out-of-band linearization technique. By controlling the out-of-band impedances at the baseband and 2^{nd} harmonic frequencies, the indirect third-order intermodulation products are used to cancel out the direct ones.

band. Providing a short circuit condition in the baseband or 2^{nd} harmonic band blocks secondary mixing, while the use of high impedances (e.g., a poorly decoupled bias circuit) tends to enforce the impact of secondary mixing.

7.1.1 HBT device linearity optimization

Experimental proof of this theory is given in [105], where the active harmonic load-pull system described in this thesis work is used to measure the linearity of SiGe and GaAs heterojunction bipolar transistors (HBT) under two-tone stimulus. The fundamental and 2^{nd} harmonic source and load impedances are actively controlled, and the baseband source and load impedance are controlled passively using real impedances ranging from 0.5 to 2,048 Ω with a resistive switch bank [64], as illustrated in Fig. 7.2.

Four different HBT devices are measured, as shown in table 7.1.

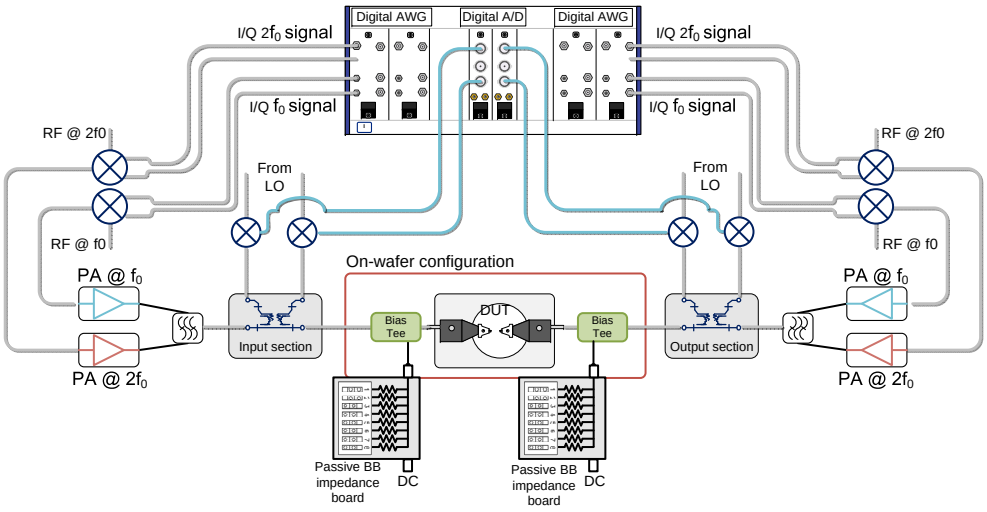

Figure 7.2: The mixed-signal based active load-pull setup with passive baseband control extension.

Measured HBT devices			
	Technology	Size (μm^2)	Measured Peak ft (GHz)
A	SiGe (C)	99	45
B	GaAs (AlGaAs)	48.4	43
C	GaAs (AlGaAs)	48.4	35
D	GaAs (InGaP)	44	100

Table 7.1: Overview of measured HBT devices.

Firstly, the fundamental source and load impedances are optimized for PAE under single-tone excitation. From two-tone measurements, the baseband impedance, second harmonic impedance and base-emitter voltage were swept, and the optimal combination of $Z_{s,bb}$, $Z_{s,2f}$ and collector current were found. Finally, $Z_{s,bb}$, and $Z_{s,2f}$ are fixed to their optimal values, and the input power and V_{be} are swept. The output third-order intercept point (OIP_3) contours are plotted in Fig. 7.3 on the output power and quiescent current plane. The practical application of this method becomes apparent if the bias point for achieving optimum linearity is found from these plots. The resulting IM_3 level versus PAE is shown in Fig. 7.4. In particular, Fig. 7.4a shows the IM_3 vs. the two-tone PAE for the collector quiescent currents that result in the highest OIP_3 value. Fig. 7.4b depicts the IM_3 vs. the two-tone PAE for the

quiescent current that provides the highest two-tone linearity near the 1-dB compression point, which was close to 3 mA for all devices shown.

Note that to guarantee low uncertainties in the linearity measurement, the harmonic distortion products generated by the system should be at least 18 dB below the harmonic distortion level of the DUT. For this reason, the measurements reported are only possible thanks to the high dynamic range of the system, and the capability to control the impedance for a wideband signal in and out-of-band.

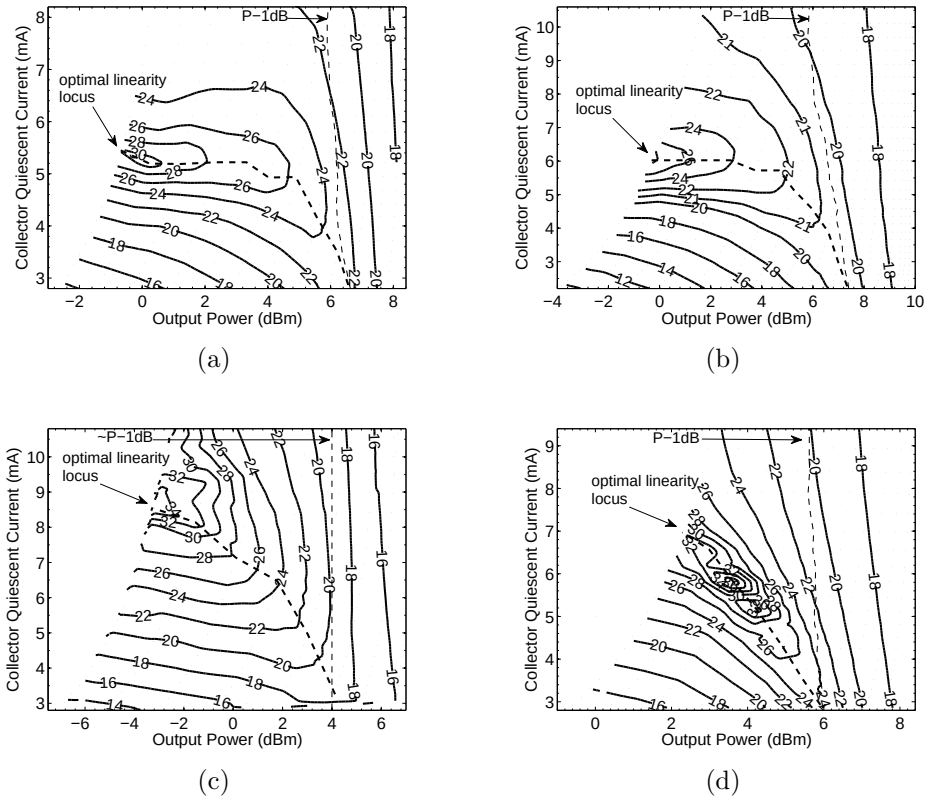

Figure 7.3: Measured OIP_3hi (dBm) contours on the output power and quiescent current plane for: (a) device A, (b) device B, (c) device C and (d) device D from Table 7.1. The 1-dB compression points and optimal linearity loci are indicated. Courtesy of K. Buisman [105].

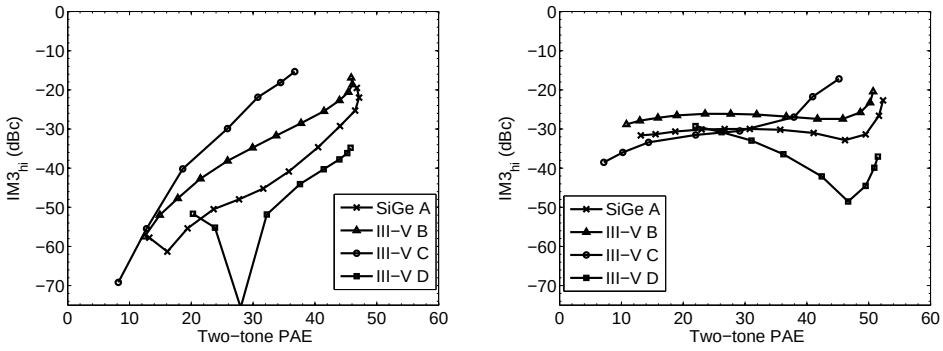

Figure 7.4: IM_3 (dBc) versus two-tone PAE (%) for: (a) the bias current for which the highest OIP_3 was measured, and (b) the bias current for which the highest two-tone linearity was measured near the 1 dB compression point, which was 3 mA for all devices measured. Courtesy of K. Buisman [105].

7.1.2 Device characterization for LTE applications with baseband, fundamental and harmonic wideband impedance control

In the previous section, baseband impedance control is offered by using a resistor switch bank. When a passive baseband impedance control is placed very close to the RF probe or test fixture, the minimum electrical delays are too large, and it is therefore only useful in the characterization of low-power devices for relatively narrow modulation bandwidths (e.g., BW $<$ 10 MHz). When moving to higher power levels (which demand lower impedance levels) or to higher bandwidths, the use of passive baseband terminations will impair the linearity characterization. In fact, under these conditions passive baseband terminations cannot provide sufficiently low impedance levels across the whole frequency range to avoid electrically-induced memory effects. In addition, it is not possible to mimic realistic baseband impedances vs. frequency which are present in real power circuits. An example here could be the notorious resonances in the impedance behavior of the bias network, which can severely violate the desired baseband decoupling, and cause severe problems for the digital predistorters presently used in base-station applications. Consequently, the ability to control and define the baseband impedance vs. frequency arbitrarily is highly desirable in the linearity characterization of

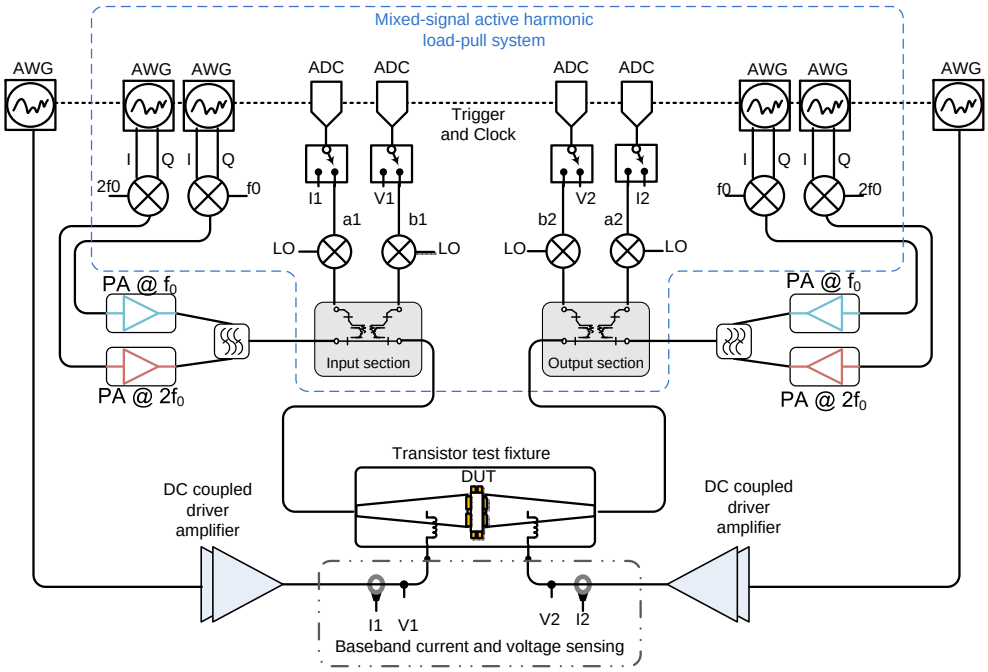

Figure 7.5: The mixed-signal-based active load-pull setup with active baseband control extension.

devices for wireless applications.

The mixed-signal active load-pull system described in Chapter 4 has been extended to provide arbitrary control of the baseband impedance termination vs. frequency for a wideband modulated signal by means of active injection. In this setup, depicted in Fig. 7.5, a two-channel arbitrary waveform generator is used to control both the source and the load impedance at baseband to the DUT. The signal is then amplified by two DC-DC converters / baseband drivers that are used to provide the active bias to the DUT. These active loops are directly connected to the bias paths of a dedicated wideband test fixture, which is optimized for the characterization of packaged high-power devices, and supports both direct and indirect water cooling to control the operating temperature of the active DUT. Note that in contrast to many other works that focus on device linearity, the controlled baseband impedance is truly DC-coupled. These baseband loops act like DC supplies with an internal impedance that can be user-defined in software. Failing to do so yields non-realistic discontinuous behavior in the baseband impedance vs. frequency, while phenomena that occur in almost any power amplifier, such as self-biasing and memory effects induced by the baseband impedance, cannot be mimicked

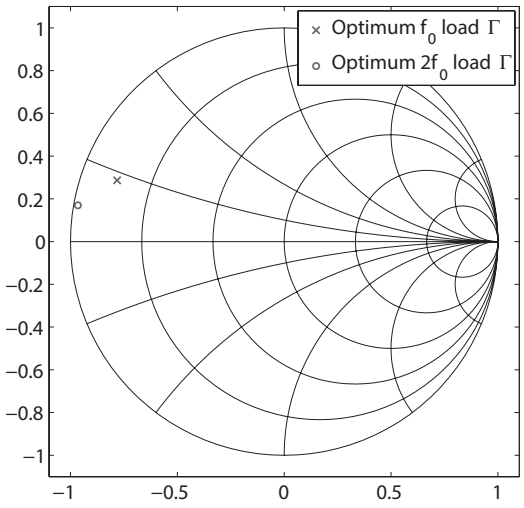

Figure 7.6: Optimum load fundamental and 2^{nd} harmonic reflection coefficients providing maximum PAE under pulsed-RF single-tone excitation.

correctly.

The measurement of the baseband impedance seen at the DUT reference plane is obtained by acquiring the voltage and the current from DC to 48 MHz using a current and voltage probe and analog-to-digital converters with a sampling speed of 100 MS/s. To obtain a calibrated measurement of the source and load baseband impedances seen by the DUT at the reference plane, a conventional SOL calibration is performed. For this purpose, short, open and load calibration standards compatible with the device test fixture have been designed, implemented and modelled.

To illustrate the importance of controlling the baseband impedance properly when characterizing active devices with realistic communication signals, a NXP GEN7 LDMOS device with $W_g = 10$ mm is measured with a 20 MHz wide LTE signal using a peak-to-average ratio of 9.8 dB. Initially, the fundamental and 2^{nd} harmonic load impedances yielding maximum PAE are found by performing harmonic load-pull measurements under pulsed-RF, single-tone excitation. The optimum values for the load reflection coefficients are depicted in Fig. 7.6. Afterwards, the DUT is measured with an LTE input signal for the (previously found) fundamental and harmonic conditions, and its ACPR and EVM performance are evaluated as a function of the baseband load impedance.

Three different cases are evaluated in the following experiments, which

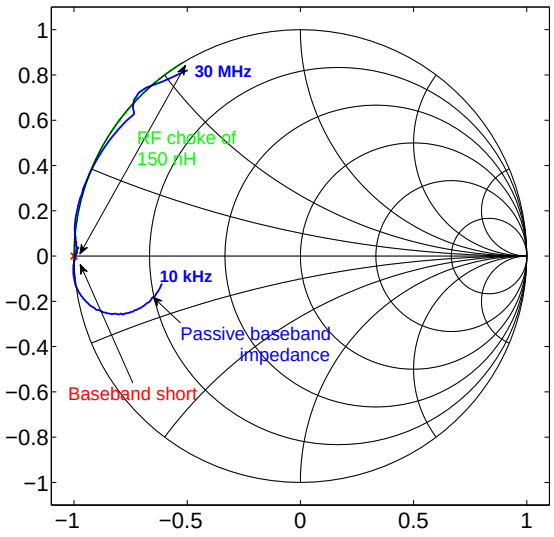

Figure 7.7: Measured impedance at the DUT reference plane for three different cases.

yield different baseband load impedances:

- Passive baseband impedance as provided by the test fixture (no BB impedance control).
- Baseband injection signal set to mimic a baseband short at the load side.
- Baseband injection signal at load side set such that it mimics a feed inductance of 150 nH in the DUT bias line.

The baseband impedance provided to the load plane at the DUT measured up to the 30 MHz controlled bandwidth is illustrated in Fig. 7.7. The results reported in Fig. 7.8 clearly highlight that proper termination of the baseband load impedance to a short condition improves both the out-of-band (ACPR) and the in-band (EVM) linearity of the active device. In particular an improvement of 10 dBc in the ACPR and 5 % in EVM is observed for an average output power of 35 dBm. Note that the system is capable of providing any arbitrary, user-defined impedance vs. frequency in the fundamental, 2^{nd} harmonic and baseband frequency bands. In these experiments, a bandwidth of 60 MHz is controlled at f_0 to include the 20 MHz signal span and its adjacent

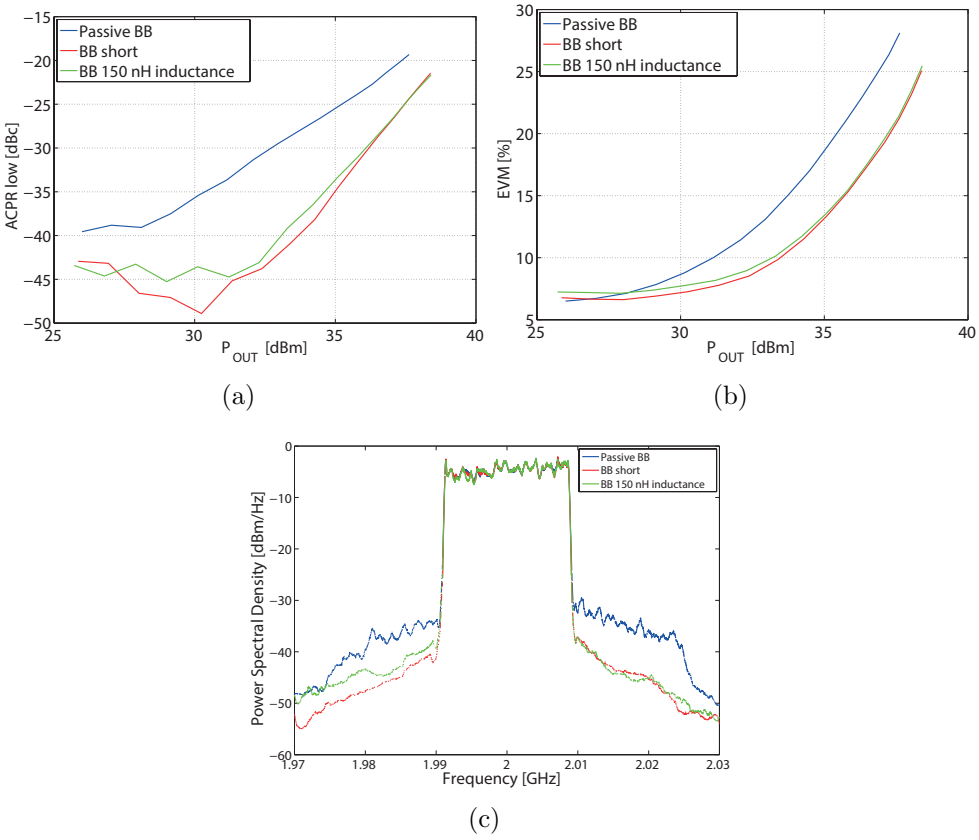

Figure 7.8: Measured: (a) ACPR (dBc) low, (b) EVM (%), and (c) power spectral density (dBm/Hz) at 30 dBm P_{OUT} for three different baseband load impedance terminations.

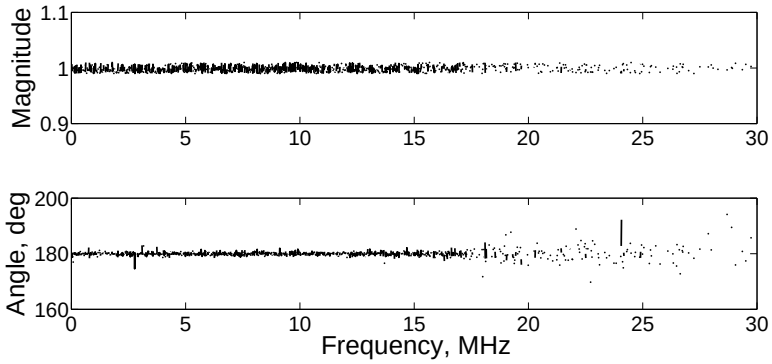

Figure 7.9: Magnitude and phase (deg) of the controlled baseband load reflection coefficient vs. frequency (MHz) at the DUT reference plane.

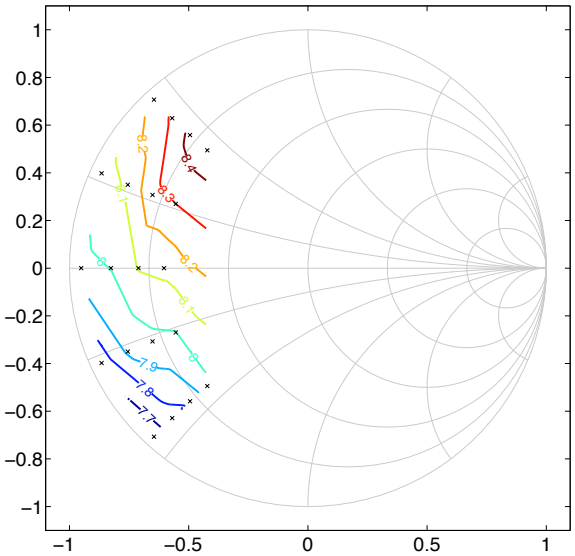

Figure 7.10: EVM (%) contour at a fixed output power of 31 dBm as function of baseband impedance termination. The contours are plotted on a Smith chart (20 Ω reference impedance).

channels. This will result in a 120 MHz bandwidth controlled at the 2^{nd} harmonic, while the baseband impedance is controlled over a 30 MHz frequency span. An example is shown in Fig. 7.9, where the magnitude and angle of the baseband load reflection coefficient vs. frequency is plotted. It can be seen that an excellent control can be achieved throughout the measurement bandwidth.

Finally, Fig. 7.10 shows contours of EVM for a 20 MHz LTE signal at a constant average output power of 31 dBm as a function of the baseband load impedance, plotted in a Smith chart with a reference impedance of 20 Ω. It is clear that both the imaginary as well as the real parts of the baseband impedance at the DUT reference plane affect the linearity of the active device, and therefore require careful attention in both circuit implementation and characterization.

7.2 High-power device measurements for base-station applications

The transistor device size used in modern macro base-stations has been increasing drastically, and recently powers of several hundred Watts have been reached. When looking at load-pull measurements of such devices, the limitation in active load-pull lies in the amount of power required to provide the optimum reflection coefficient to the DUT at these power levels. For this reason, high-power device testing in a non-50 Ω environment has been limited to passive load-pull topologies.

The power requirements of active load-pull have already been discussed in Section 3.4, while in Section 5.3 it has been highlighted that high linearity in the injection amplifier is not required for the active load-pull system described in this thesis work.

In this section, load-pull measurement results are presented for two extremely high-power devices, proving the validity of the load-pull characterization system for base-station applications.

In a first test case, an NXP 7^{th} generation LDMOS 200 W-rated transistor was measured at 2.14 GHz in a pulsed-CW condition with pulse width of 50 μS, duty cycle of 10 %, and using a prematch to 7 Ω via a transformer test fixture. The power amplifier used to drive this DUT up to a P_{OUT} of 360 W and down to 0.5 Ω was a NXP Doherty amplifier demo board with a saturated output power of 500 W. Fig. 7.11a shows the measured PAE vs. output power for this test case. Fig. 7.11b shows the measured PAE vs. output power, evaluated at 3 dB of gain (G_p) compression for all of the load impedances provided.

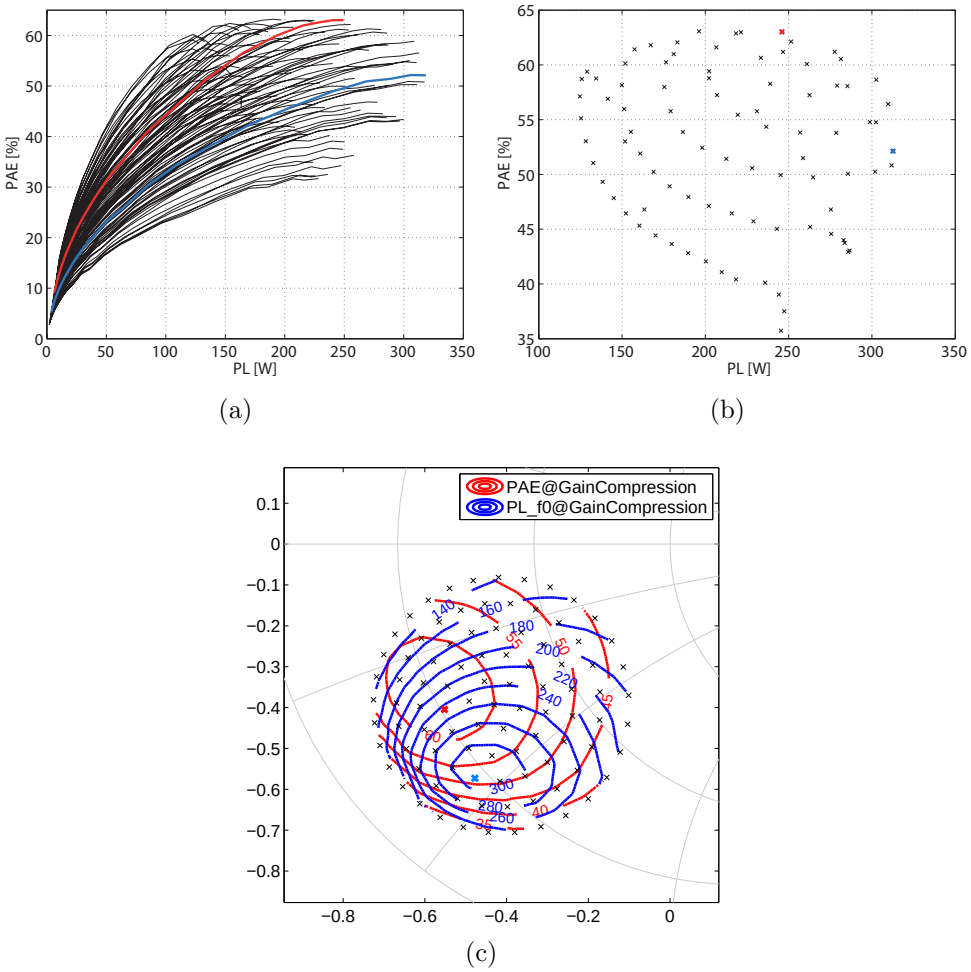

Figure 7.11: (a) Power-added efficiency (%) versus output power (W), (b) power-added efficiency (%) versus output power (W) at 3 dB of gain compression, and (c) P_{OUT} (W) and power added efficiency (%) contours at 3 dB of gain compression for an NXP 7^{th} generation LDMOS 200 W-rated transistor.

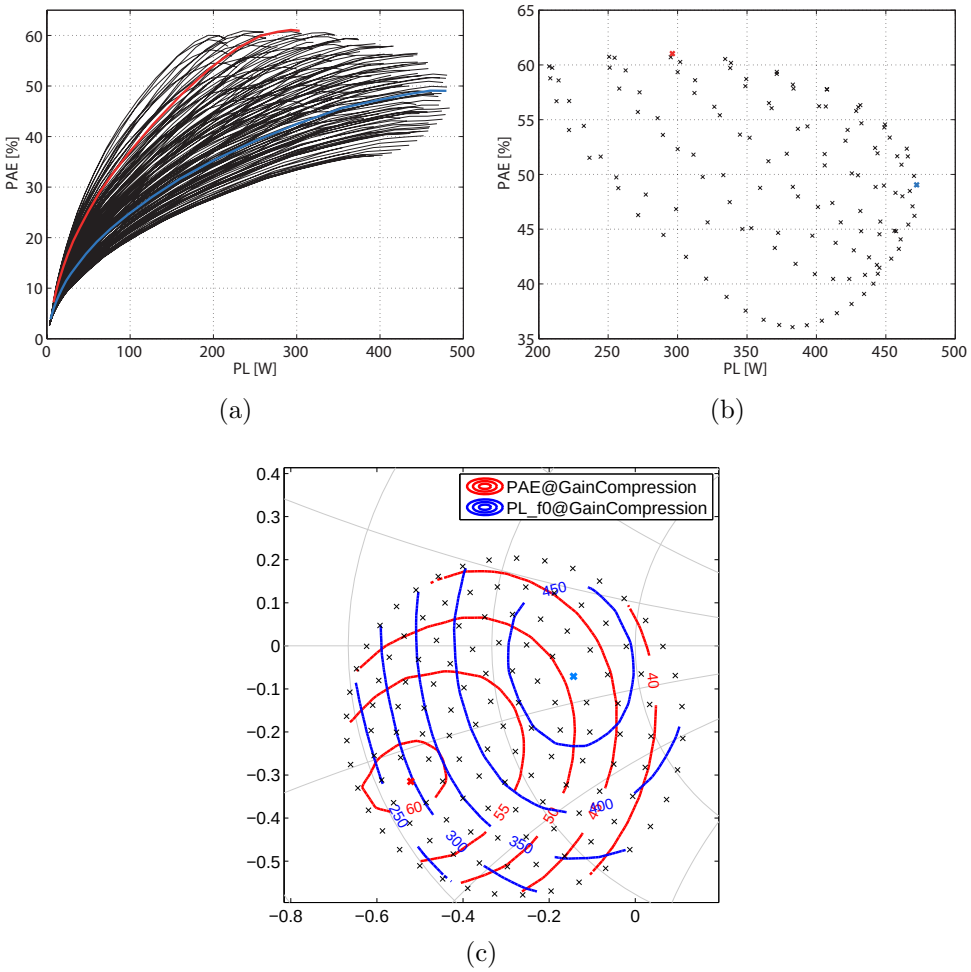

Figure 7.12: (a) Power-added efficiency (%) versus output power (W), (b) power-added efficiency (%) versus output power (W) at 3 dB of gain compression, and (c) P_{OUT} (W) and power-added efficiency (%) contours at 3 dB of gain compression for an NXP 8^{th} generation LDMOS 360 W-rated transistor.

This particular device reaches a maximum output power of over 320 W at 3 dB compression (highlighted in red) and a maximum efficiency of over 64 % at 3 dB compression (highlighted in blue). Fig. 7.11c shows P_{OUT} and PAE contours at 3 dB gain compression using the 7 Ω pre-match fixture (center of Smith chart is 7 Ω). Note that impedances as low as 0.5 Ω (or $\Gamma = 0.98$ or $VSWR = 100:1$ with imaginary component) were presented to the DUT (in the DUT reference plane) and measured.

In a second measurement example, an NXP 8^{th} generation LDMOS 320 W-rated transistor was measured with the same measurement settings. The same 500 W Doherty amplifier demo board as in the previous example was used as the injection amplifier to drive the DUT up to a P_{OUT} of 500 W and down to 1.5 Ω fundamental output loading. Fig. 7.12a shows the measured PAE vs. output power for this test case, with maximum power and maximum efficiency curves highlighted in red and blue, respectively. Fig. 7.12b shows the measured PAE vs. output power evaluated at 3 dB of gain compression, with a maximum power of over 470 W (red) and a maximum efficiency of over 62 % (blue) at 3 dB compression (not concurrently). Fig. 7.12c shows P_{OUT} and PAE contours at 3 dB gain compression using a 7 Ω pre-match fixture (center of Smith chart is 7 Ω).

It is important to note that all of the above measurements were performed in an active load-pull environment with no passive mechanical tuners used in any hybrid configuration.

7.3 Device characterization for high efficiency power amplifier design

The continuous struggle towards higher efficiencies has led to the extensive use in industry of power amplifiers working in higher classes of operation [15]. Even though significant progress is made in the modelling of such devices, conventional models may not predict the device behavior under large-signal conditions properly. For this reason, power amplifier designers quite often rely on data from load-pull systems. With this perspective, the capability to control the higher harmonics terminations provided to the device under test, and the ability to measure the time-domain voltage and current waveforms developed in this thesis work prove essential to the power amplifier designer in order to achieve higher and higher efficiencies.

In this section, an example of high-efficiency amplifier design is presented. For this purpose, the mixed-signal active load-pull is used to find the optimum fundamental and second harmonic load impedances on the 50 W-rated, pack-

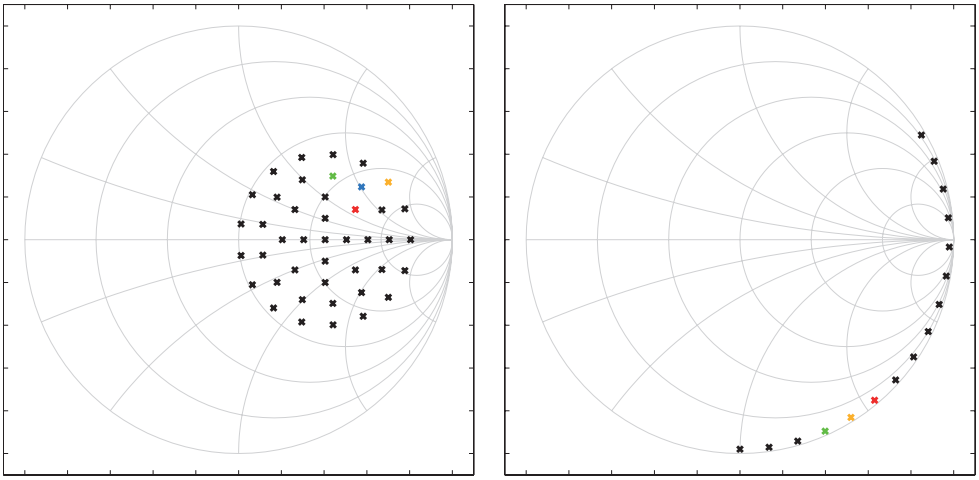

(a) (b)

Figure 7.13: (a) Fundamental load Γ sweep, (b) second harmonic load Γ sweep on a Smith chart (10 Ω reference impedance).

aged NXP GaN HEMT with a gate width of 12 mm, already used in Section 6.2.3. Also, the device in this example is measured at a frequency of 2 GHz and is biased at a V_{DD} of 50 V with a quiescent current I_{DQ} of 150 mA. Once again, the simple model shown in Fig. 6.17 has been used to de-embed the voltage and current waveforms at the level of the internal drain node.

In order to find the optimum tuning impedances yielding the highest efficiency, the fundamental and second harmonic load Γ are swept simultaneously in the range depicted in Fig. 7.13.

The results are shown in Fig. 7.14, where the efficiency versus output power is reported at a gain compression level of 3 dB. The gain is plotted versus output power and the dynamic load line, measured at 35 dBm and at 45 dBm of output power, is depicted for every combination of fundamental and 2^{nd} harmonic load Γ.

It may be noted from Fig. 7.14c that the device is operating into class J for the combination of Γ highlighted in yellow. This is more clearly visible by looking at the voltage and current waveforms versus time as a function of power, shown in Fig. 7.15a and 7.15c. Here, the peak voltage approaches the theoretical value of $2.92 \cdot V_{DD}$ for class J very closely.

In Fig. 7.14a, however, it is easy to identify that the highest efficiency reaches 80 % for the fundamental and 2^{nd} harmonic Γ highlighted in red. In

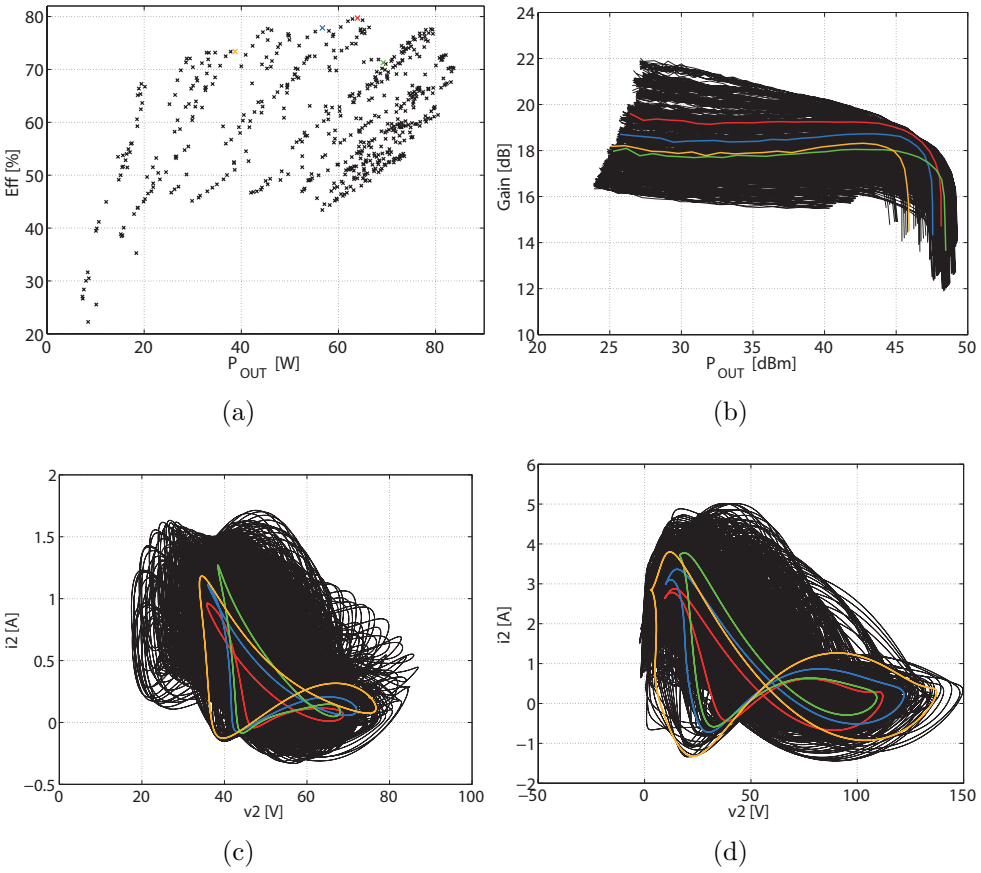

Figure 7.14: (a) Efficiency (%) versus output power (W) at 3 dB of gain compression, (b) power gain (dB) versus output power (dBm), (c) dynamic load line measured at $P_{OUT} = 35\ dBm$ and (d) dynamic load line measured at $P_{OUT} = 45\ dBm$ plotted for every combination of fundamental and 2^{nd} harmonic load Γ. The highighted points correspond to the combination of fundamental and 2^{nd} harmonic load Γ which are also highlighted in Fig. 7.13.

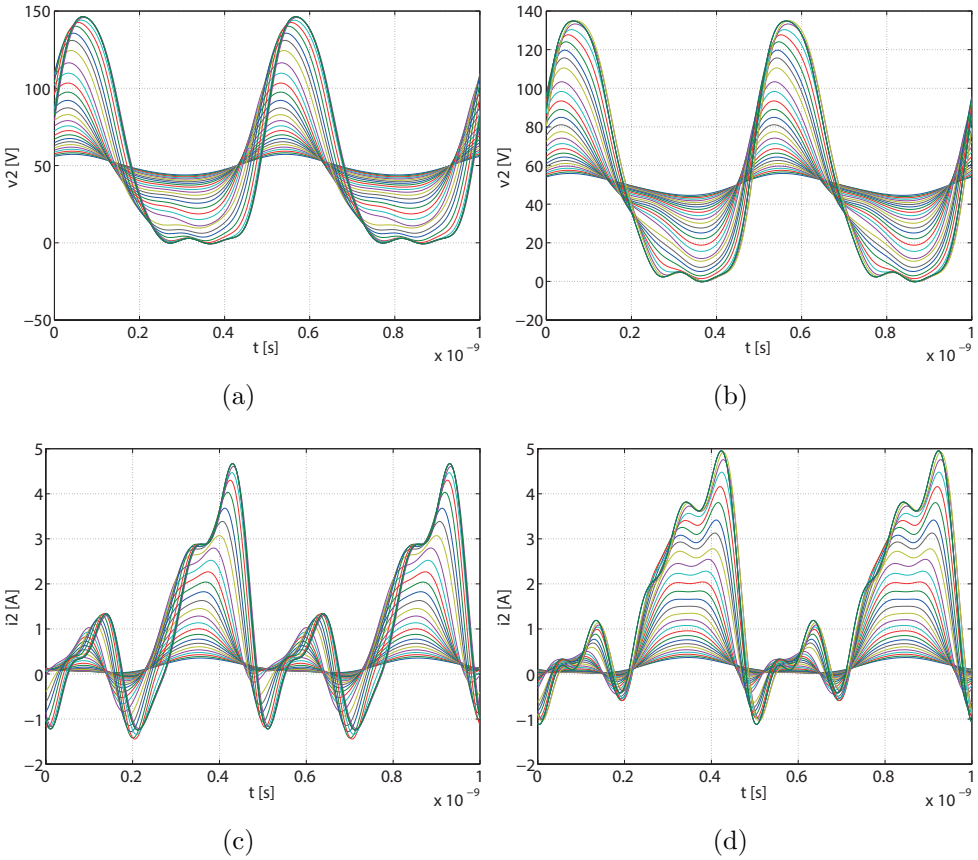

Figure 7.15: (a) Voltage (V_{DS}) and (c) current (I_D) time-domain waveform measured as a function of power at the output current generator of the DUT for the combination of fundamental and 2^{nd} harmonic load Γ highlighted in yellow in Fig. 7.13. (b) Voltage (V_{DS}) and (d) current (I_D) time-domain waveform measured as a function of power at the output current generator of the DUT for the combination of fundamental and 2^{nd} harmonic load Γ highlighted in red.

this case, it is not easy to identify what class the device is operating in from the load-line, while from Fig. 7.15b and 7.15d it can be seen that the peak voltage for this particular point is slightly lower than for pure class-J operation.

This example clearly highlights that the ability to measure time-domain waveforms gives powerful insight into the device behavior, while providing valuable information such as peak voltage and current which can be helpful for considerations such as ruggedness. However, the high speed of the system that allows to quickly search through a wide range of fundamental and harmonic impedances proves to be the real added value when using such a large-signal measurement system for power amplifier design.

7.4 Conclusions

Several examples have been presented which highlight the most important features of the mixed-signal load-pull system developed during this thesis work.

Experimental results obtained using this setup show that active device linearity, when operating with wideband-modulated signals (e.g., LTE) is severely influenced by the baseband impedance offered to the device under test. The ability to control these baseband impedances vs. frequency allows the user to optimize the linearity of active devices for complex modulated signals, and to troubleshoot memory effects due to the baseband impedance terminations provided by a realistic matching network implementation as well.

Furthermore, the system is flexible enough to serve many different kinds of applications, ranging from low-power, high-linearity measurements to the characterization of extremely high-power devices for base-stations applications.

Finally, the high speed of the system coupled with the ability to measure time-domain waveforms at the device intrinsic current generator plane, makes the mixed-signal load-pull system a valuable tool for high-efficiency power amplifier design.

Chapter 8

Conclusions and Future Work

8.1 Conclusions

The focus of this thesis is the creation of new characterization techniques that support technology development, (compact) model device extraction / validation and design activities, that address the specific needs of advanced wideband communication systems. Since the transmit path in these next-generation wireless systems presents the largest challenges in terms of efficiency, linearity and bandwidth, special attention is given to extending the current state-of-the-art in pulsed and large-signal characterization techniques in terms of duty-cycle, accuracy, power, impedance control, bandwidth, measurement speed and functionality.

One of the key inventions in this work is a novel time gating and data alignment approach that, when applied in an isothermal measurement system, enables pulsed-DC and RF measurements down to 200 ns with an excellent dynamic range which is independent from duty-cycle. As such, the realized setup facilitates the characterization of RF / microwave devices under truly isothermal conditions. This functionality gives significant advantages in defining, extracting and verifying (compact) models for various RF power devices that typically suffer severely from bias and operation-dependent self-heating and/or trapping effects.

The second and dominant part of this thesis relates to the development and realization of a revolutionary active harmonic load-pull system. The system capabilities are summarized and compared to state-of-the-art load-pull systems in Fig. 8.1. This system provides, for the first time, the capability to synthesize truly arbitrary source and loading conditions vs. frequency at the fundamental and harmonic frequencies over a large bandwidth (currently

120 MHz). This setup enables testing of active devices under realistic (circuit-like) conditions with wideband modulated signals. The ability to control up to three harmonics at high power levels with an extremely high speed (up to 1,000 measurement points per minute), dramatically enhances the process of developing new transistor technologies and their application in very efficient and linear power-amplifiers. Moreover, the option to measure time-domain voltage and current waveforms can provide significant insight into the actual device behavior, which benefits power amplifier design, ruggedness evaluation, as well as (database) model extraction and validation. The usefulness of the system has been demonstrated by applying this newly developed load-pull characterization system to several relevant application examples.

All measurement setups and techniques introduced in this thesis are based on the innovative mixed-signal measurement concept, which replaces traditional analog solutions with digital data acquisition and digital signal generation. This approach, sometimes also referred to as "synthetic" or "software-defined" instruments [106], provides much higher flexibility, functionality, performance and speed in many different applications when compared to traditional techniques. It is expected that mixed-signal systems will change the current landscape of RF/microwave characterization.

8.2 Future work

The flexibility of the mixed-signal approach, and of the resulting measurement setups developed during this thesis work, provides many opportunities for future work. In this concluding section some of the future trends and topics are identified that can motivate future research activities and developments in this field.

8.2.1 Supporting new generation signals and systems

The introduction of new modulation standards, such as LTE Advanced and 802.11ac, which make use of wider bandwidths to provide higher data rates, is pushing the bandwidth requirements of the underlying hardware beyond current capabilities. At the same time, the growing interest in handling multiple standards in one single transmit / receive chain demands the design of power amplifiers that maintain high efficiency over multiple bands or across a wide frequency range while accommodating multiple standards.

Another trend in the R&D world is defined by the presence of large segments of unlicensed spectrum at mm-wave frequencies (e.g., 57 to 64 GHz),

Comparison of load-pull methods				
	Passive LP	Active LP	Hybrid-active LP	Mixed-signal LP
VSWR/Γ at DUT	Relatively low VSWR (reduced further by losses of cables, fixture, etc.)	Γ≥1 possible	Γ≥1 possible	Γ≥1 possible
Harmonic impedance control	Available (requires one tuner per freq or large multi-freq tuner)	Available (requires one signal source per harmonic)	Available (requires one signal source per harmonic)	Integrated up to 3rd harmonic
Tuning speed	1-5 seconds per impedance due to tuner movement	≤1 second per state	≤1 second per state on active paths	Up to 1,000 impedance/power states per minute
Measurement speed	1-15 seconds per state due to instruments	≤1 second per state	≤1 second per state	See above
Amplifier requirements	Only requires driver amplifier	1-10x P_{OUT}	0.5-2x P_{OUT}	1-10x P_{OUT}
Signal Types	CW, pulsed-CW, modulated	CW, pulsed-CW	CW, pulsed-CW	CW, pulsed-CW, modulated
Wideband impedance control	Uncontrolled wideband	N/A	N/A	120 MHz user-defined impedance control
On-wafer integration	Can be difficult due to tuner sizes and movements	Easy, no vibration	Can be difficult due to tuner sizes and movements	Easy, no vibration
Oscillations	Risk due to wideband reflection	Low probability	Risk due to wideband reflection	Low probability
Time-domain	Yes (NVNA dependent)	Yes (NVNA dependent)	Yes (NVNA dependent)	Yes

Figure 8.1: Comparison of state-of-the-art load-pull (LP) methods.

which has initiated a tremendous effort to develop broadband communication systems capable of achieving multi gigabit data transfer rates at mm-waves frequencies.

To support these design developments, there is need for broadband load-pull test-benches and general purpose measurement systems, that are capable of handling ultra-wide modulation bandwidths, not only in the telecommunication bands, but also at higher frequencies. A first effort in this direction has already been made in [107], where the mixed-signal load-pull concept discussed in this thesis is used to enable active load-pull at mm-wave frequencies, with a modulation bandwidth up to 1 GHz. Nevertheless, the desire for greater bandwidth, coupled with the ever-present need for high accuracy and dynamic range, brings about the need for innovative system architectures and measurement techniques.

8.2.2 Supporting high-efficiency and high-linearity advanced PA design

The high peak-to-average ratio of 3G and 4G modulation standards has required the introduction of advanced PA topologies which are able to perform efficiently not only at peak output power, but also in power back-off where (statistically) most of the energy is consumed. A topology like the Doherty PA [12] has found wide use in industry, while concepts like envelope-tracking [14] and outphasing [13] amplifiers are being studied intensively at the research level.

Designing these advanced classes of amplifiers is a challenging task. From this perspective, measurement tools and techniques to enable the load-pull characterization of multi-input amplifiers would be extremely valuable. Moreover, the capability to modulate the bias to the DUT directly in a load-pull environment would be essential to support envelope tracking amplifiers design.

Another opportunity for research is given by the fact that many of these amplifier topologies are extremely non-linear, and require predistortion of the input signal to operate linearly and comply with the communication standard specifications. The possibility to predistort the input signal directly on the active load-pull test bench would be extremely useful to verify directly whether the DUT can comply with the linearity specifications after predistortion, before actually implementing the power amplifier board.

8.2.3 Supporting next generation device modelling

The introduction of new transistor technologies with higher performance (i.e., power, efficiency) brings with it the challenge of creating new and more ac-

curate models for circuit simulation. In a fast growing industry like telecommunication, where time-to-market is extremely important, enabling the rapid and simple extraction of new device models directly from measurements has received significant interest. For this reason, significant effort has been put into the development of behavioral models in recent years, such as the poly-harmonic distortion (PHD) model [108], which enable the extraction of device models directly from large-signal measurements.

These models employ the measurement of time-domain voltage and current waveforms under the different boundary conditions which affect the DUT performance in order to create a database describing the behavior of the DUT. For this reason, they require the device to be measured throughout the multidimensional space of all of the different tunable parameters, such as fundamental and harmonic source and load impedance, frequency, bias, etc.

Thanks to its very high measurement speed of up to 1,000 measurement point per minute, the load-pull system described in this thesis can prove to be an extremely valuable asset for the extraction of these type of models. Furthermore, the development of additional measurement techniques to extend their range of validity (e.g., to include memory effects) is also a topic of interest.

In terms of compact modeling, an issue is represented by the continuous scaling in device size which is necessary to achieve higher cut-off frequencies [109]. For this reason, the thermal resistance of some high-frequency devices can reach values as high as 10,000 K/W [110, 111]. To model these new device generations, faster pulsed-DC measurements than what is currently available are necessary to achieve truly isothermal conditions.

Conventional pulsed bias approaches employ analog pulsers to provide current drive and to deliver the required voltage shape to the DUT. Nevertheless, these methods cannot compensate for the distorting effect on the voltage waveform, arising from the interconnects and parasitic loading, due to the analog nature of the driver. Therefore the minimum DC pulse widths achievable with conventional pulsers are severely limited (to approximately 200 - 300 ns).

A more elaborate approach, based on a mixed-signal technique, can achieve significantly shorter DC pulse widths (e.g., 10 ns or lower) by using a high-speed AWG and a DC-coupled driver amplifier to generate the DC pulse, a high-speed A/D converter to measure the calibrated DC pulse at the DUT, and an iterative approach to optimize the DC pulse provided to the DUT [112]. However, in order for such an approach to be successful, the design of a high-power DC-coupled amplifier, capable of providing high voltage and current (e.g., 200 V and 30 A) with a wide bandwidth (e.g., 100 MHz), is required.

8.3 Future trends

The aforementioned demand for higher bandwidth, efficiency and functionality of next generation communication systems requires more complex design approaches to the power amplifier, which is now shifting further away from the traditional "linear" class-AB operation.

For this reason, RF characterization can no longer be limited to simple S-parameter and spectral distortion measurements. The transmitter output stage with its surrounding circuitry (e.g., voltage supply modulators) should now be considered as a dynamic, non-linear sub-system, which can no longer be described or characterized easily by conventional modelling and measurement tools.

To fully address these upcoming design challenges, innovative and more advanced, test and modelling solutions will be required. The mixed-signal techniques introduced in this thesis provide an enabling platform for a new generation of measurement tools, which can encompass many of the functions of an advanced circuit or system simulator at an hardware level. The device or sub-system under test can now be placed in a virtual circuit environment, where the DUT itself constitutes the actual (most complete) model, and the mixed-signal core of the measurement system is capable to mimic a realistic circuit or system implementation accurately. It is the author's belief that this novel approach will open up new possibilities and measurement applications, which will push microwave and RF characterization to unprecedented levels.

Bibliography

[1] http://newsroom.cisco.com/release/1114955.

[2] http://www.cisco.com/en/US/solutions/collateral/ns341/ns525/ns537/ns705/ns827/white_paper_c11-520862.html.

[3] G. Fettweis and E. Zimmermann, "ICT energy consumption-trends and challenges," in *Proceedings of the 11th International Symposium on Wireless Personal Multimedia Communications*, vol. 2, no. 4, 2008, p. 6.

[4] E. Oh, B. Krishnamachari, X. Liu, and Z. Niu, "Toward dynamic energy-efficient operation of cellular network infrastructure," *Communications Magazine, IEEE*, vol. 49, no. 6, pp. 56–61, 2011.

[5] W. Vereecken, W. Van Heddeghem, M. Deruyck, B. Puype, B. Lannoo, W. Joseph, D. Colle, L. Martens, and P. Demeester, "Power consumption in telecommunication networks: overview and reduction strategies," *Communications Magazine, IEEE*, vol. 49, no. 6, pp. 62–69, 2011.

[6] O. Blume, D. Zeller, and U. Barth, "Approaches to energy efficient wireless access networks," in *Communications, Control and Signal Processing (ISCCSP), 2010 4th International Symposium on*, 2010, pp. 1–5.

[7] I. Stevanovic, A. Skrivervik, and J. R. Mosig, "Smart antenna systems for mobile communications," *Ecole Polytechnique Federale De Lausanne, Technical Report*, 2003.

[8] J. Louhi, "Energy efficiency of modern cellular base stations," in *Telecommunications Energy Conference, 2007. INTELEC 2007. 29th International*, 2007, pp. 475–476.

[9] "Base station conformance testing (FDD)," Technical Specification Group Radio Access Networks - 3rd Generation Partnership Project, 3GPP TS 25.141 V4.1.0 (2001-06), 2001.

[10] LAN/MAN standards Committee and others, "Part 11: Wireless LAN medium access control (MAC) and physical layer (PHY) specifications," *IEEE-SA Standards Board*, 2003.

[11] J. Sevic, "Statistical characterization of RF power amplifier efficiency for CDMA wireless communication systems," in *Wireless Communications Conference, 1997., Proceedings*, 1997, pp. 110–113.

[12] W. H. Doherty, "A new high efficiency power amplifier for modulated waves," *Radio Engineers, Proceedings of the Institute of*, vol. 24, no. 9, pp. 1163–1182, 1936.

[13] H. Chireix, "High power outphasing modulation," *Radio Engineers, Proceedings of the Institute of*, vol. 23, no. 11, pp. 1370–1392, 1935.

[14] F. Raab, P. Asbeck, S. Cripps, P. Kenington, Z. Popovic, N. Pothecary, J. Sevic, and N. Sokal, "Power amplifiers and transmitters for RF and microwave," *Microwave Theory and Techniques, IEEE Transactions on*, vol. 50, no. 3, pp. 814–826, 2002.

[15] S. Cripps, *RF power amplifiers for wireless communications*. Artech House Norwood, MA, 2006.

[16] H. Ku, M. D. McKinley, and J. S. Kenney, "Quantifying memory effects in RF power amplifiers," *IEEE Trans. Microwave Theory Tech.*, vol. 50, no. 12, pp. 2843–2849, 2002.

[17] J. Paasschens, W. Kloosterman, and R. vd Toorn, "Model derivation of Mextram 504," *dNA*, vol. 510, pp. 2–30, 2005.

[18] C. McAndrew, J. Seitchik, D. Bowers, M. Dunn, M. Foisy, I. Getreu, M. McSwain, S. Moinian, J. Parker, D. Roulston, M. Schroter, P. van Wijnen, and L. Wagner, "VBIC95, the vertical bipolar inter-company model," *Solid-State Circuits, IEEE Journal of*, vol. 31, no. 10, pp. 1476 –1483, Oct. 1996.

[19] M. Schroter, *HICUM, a scalable physics-based compact bipolar transistor model*, level 2 ed., http://www.iee.et.tu-dresden.de/iee/eb/eb_homee.html, 2005.

[20] V. Cuoco, M. van den Heijden, and L. de Vreede, "The "Smoothie" data base model for the correct modeling of non-linear distortion in FET devices," in *Microwave Symposium Digest, 2002 IEEE MTT-S International*, vol. 3, 2002, pp. 2149 –2152.

[21] P. Roblin, D. E. Root, J. Verspecht, Y. Ko, and J. P. Teyssier, "New trends for the nonlinear measurement and modeling of high-power RF transistors and amplifiers with memory effects," *IEEE Trans. Microwave Theory Tech.*, vol. 60, no. 6, pp. 1964–1978, 2012.

[22] J. P. Teyssier, M. Campovecchio, C. Sommet, J. Portilla, and R. Quere, "A pulsed S-parameters measurement setup for the non-linear characterization of FETs and bipolar power transistors," in *Microwave Conference, 1993. 23rd European*, Sept. 1993, pp. 489 –493.

[23] B. Taylor, M. Sayed, and K. Kerwin, "A pulse bias/RF environment for device characterization," in *ARFTG Conference Digest-Fall, 42nd*, vol. 24, Dec. 1993, pp. 57 –60.

[24] J. P. Teyssier, P. Bouysse, Z. Ouarch, D. Barataud, T. Peyretaillade, and R. Quere, "40-GHz/150-ns versatile pulsed measurement system for microwave transistor isothermal characterization," *Microwave Theory and Techniques, IEEE Transactions on*, vol. 46, no. 12, pp. 2043 –2052, Dec. 1998.

[25] S. J. Doo, P. Roblin, S. Lee, D. Chaillot, and M. Vanden Bossche, "Pulsed-IV pulsed-RF measurements using a large signal network analyzer," in *ARFTG Conference Digest, 2005. Spring 2005. 65th*, June 2005, p. 7 pp.

[26] C. Baylis, L. Dunleavy, and J. Martens, "Constructing and benchmarking a pulsed-RF, pulsed-bias S-parameter system," in *ARFTG Conference Digest-Fall, 66th*, Dec. 2005.

[27] V. Teppati, A. Ferrero, and U. Pisani, "Recent advances in real-time load-pull systems," *Instrumentation and Measurement, IEEE Transactions on*, vol. 57, no. 11, pp. 2640 –2646, Nov. 2008.

[28] *Application note, 1408-11: accurate pulsed measurements*, Agilent Technologies, Feb. 2004.

[29] *Application note, 1408-12: pulsed-RF S-parameter measurements using wideband and narrowband detection*, Agilent Technologies, May 2006.

[30] Agilent Technologies, "8510 pulsed-RF network analyzer user's guide," Mar. 1995.

[31] L. Betts, "Tracking advances in pulsed S-parameter measurements," *Microwaves & RF*, Sept. 2007.

[32] *8510 pulsed-RF network analyzer user's guide* , Agilent Technologies, Mar. 1995.

[33] I. Kollár, "Evaluation of sine wave tests of ADCs from windowed data," *Computer Standards & Interfaces*, vol. 22, no. 4, pp. 261–268, 2000.

[34] W. Kester, A. Devices, *et al.*, *Data conversion handbook*. Newnes, 2005.

[35] M. Hauser, "Principles of oversampling A/D conversion," *J. Audio Eng. Soc*, vol. 39, no. 1/2, pp. 3–26, 1991.

[36] M. Reisch, *High-frequency bipolar transistors: physics, modelling, applications*. Springer Verlag, 2003.

[37] G. Gonzalez, *Microwave transistor amplifiers: analysis and design*. Prentice hall New Jersey, 1997, vol. 2.

[38] F. van Rijs and S. Theeuwen, "Efficiency improvement of LDMOS transistors for base stations: towards the theoretical limit," in *Electron Devices Meeting, 2006. IEDM '06. International*, Dec. 2006, pp. 1 –4.

[39] P. Deixler, R. Colclaser, D. Bower, N. Bell, W. De Boer, D. Szmyd, S. Bardy, W. Wilbanks, P. Barre, M. v Houdt, J. Paasschens, H. Veenstra, E. v d Heijden, J. Donkers, and J. Slotboom, "QUBiC4G: a fT/fmax = 70/100 GHz 0.25 μm low power SiGe-BiCMOS production technology with high quality passives for 12.5 Gb/s optical networking and emerging wireless applications up to 20 GHz," in *Bipolar/BiCMOS Circuits and Technology Meeting, 2002. Proceedings of the 2002*, 2002.

[40] N. Nenadovic, "Electrothermal behavior of high frequency silicon-on-glass transistors," Ph.D. dissertation, Delft University of Technology, 2004.

[41] M. Spirito, M. Pelk, F. van Rijs, S. Theeuwen, D. Hartskeerl, and L. de Vreede, "Active harmonic load-pull for on-wafer out-of-band device linearity optimization," *Microwave Theory and Techniques, IEEE Transactions on*, vol. 54, no. 12, pp. 4225 –4236, Dec. 2006.

[42] http://www.maurymw.com.

[43] http://www.focus-microwaves.com/.

[44] V. Teppati and A. Ferrero, "A new class of nonuniform, broadband, nonsymmetrical rectangular coaxial-to-microstrip directional couplers for high power applications," *Microwave and Wireless Components Letters, IEEE*, vol. 13, no. 4, pp. 152 – 154, Apr. 2003.

[45] F. De Groote, J. Verspecht, D. Barataud, and J.-P. Teyssier, "An improved coupling method for time domain load-pull measurements," in *Microwave Conference, 2005 European*, vol. 1, Oct. 2005, p. 4 pp.

[46] G. Bava, U. Pisani, and V. Pozzolo, "Active load technique for load-pull characterisation at microwave frequencies," *Electronics Letters*, vol. 18, no. 4, pp. 178 –180, Feb. 1982.

[47] J. E. Muller and B. Gyselinckx, "Comparison of active versus passive on-wafer load-pull characterisation of microwave and mm-wave power devices," in *Microwave Symposium Digest, 1994., IEEE MTT-S International*, May 1994, pp. 1077 –1080 vol.2.

[48] A. Ferrero, F. Sanpietro, U. Pisani, and C. Beccari, "Novel hardware and software solutions for a complete linear and nonlinear microwave device characterization," *Instrumentation and Measurement, IEEE Transactions on*, vol. 43, no. 2, pp. 299 –305, Apr. 1994.

[49] T. Williams, J. Benedikt, and P. Tasker, "Experimental evaluation of an active envelope load pull architecture for high speed device characterization," in *Microwave Symposium Digest, 2005 IEEE MTT-S International*, June 2005, p. 4 pp.

[50] Y. Takayama, "A new load-pull characterization method for microwave power transistors," in *Microwave Symposium, 1976 IEEE-MTT-S International*, June 1976, pp. 218 –220.

[51] K. Nagatomo, S. Koike, M. Shigaki, N. Okubo, H. Takahashi, and T. Nakatani, "38-GHz band high-power MMIC amplifier design using improved load-pull method," in *Microwave Conference, 1990. 20th European*, vol. 1, Sept. 1990, pp. 151 –156.

[52] F. van Raay and G. Kompa, "A 40 GHz large-signal double-reflectometer waveform measurement system designed for load-pull applications," in *Microwave Conference, 1996. 26th European*, vol. 2, Sept. 1996, pp. 657 –661.

[53] J. Benedikt, R. Gaddi, P. Tasker, and M. Goss, "High-power time-domain measurement system with active harmonic load-pull for high-efficiency base-station amplifier design," *Microwave Theory and Techniques, IEEE Transactions on*, vol. 48, no. 12, pp. 2617 –2624, Dec. 2000.

[54] B. Bunz and G. Kompa, "Active load pull with fourth harmonic tuning based on an IQ modulator concept," in *Microwave Conference, 2003. 33rd European*, Oct. 2003, pp. 359 –361.

[55] H. Arthaber, M. Mayer, and G. Magerl, "A broadband active harmonic load-pull setup with a modulated generator as active load," in *Microwave Conference, 2004. 34th European*, vol. 2, Oct. 2004, pp. 685 – 688.

[56] E. McCune, "Modern cellular wireless signals," in *Microwave Measurements Conference (ARFTG), 2010 75th ARFTG*, May 2010, pp. 1 –7.

[57] M. van der Heijden, H. de Graaff, and L. de Vreede, "A novel frequency-independent third-order intermodulation distortion cancellation technique for BJT amplifiers," *Solid-State Circuits, IEEE Journal of*, vol. 37, no. 9, pp. 1176 – 1183, Sept. 2002.

[58] M. Marchetti, M. Pelk, K. Buisman, W. Neo, M. Spirito, and L. de Vreede, "Active harmonic load-pull with realistic wideband communications signals," *Microwave Theory and Techniques, IEEE Transactions on*, vol. 56, no. 12, pp. 2979 –2988, Dec. 2008.

[59] Z. Aboush, C. Jones, G. Knight, A. Sheikh, H. Lee, J. Lees, J. Benedikt, and P. Tasker, "High power active harmonic load-pull system for characterization of high power 100-watt transistors," in *Microwave Conference, 2005 European*, vol. 1, Oct. 2005, p. 4 pp.

[60] W. C. E. Neo, J. Qureshi, M. J. Pelk, J. R. Gajadharsing, and L. C. N. de Vreede, "A mixed-signal approach towards linear and efficient N-way Doherty amplifiers," *Microwave Theory and Techniques, IEEE Transactions on*, vol. 55, no. 5, pp. 866 –879, May 2007.

[61] D. Poulin, J. Mahon, and J.-P. Lanteri, "A high power on-wafer pulsed active load pull system," *Microwave Theory and Techniques, IEEE Transactions on*, vol. 40, no. 12, pp. 2412 –2417, Dec. 1992.

[62] D. Rytting, "Network analyzer error models and calibration methods," *White Paper, September*, 1998.

[63] A. Ferrero and U. Pisani, "An improved calibration technique for on-wafer large-signal transistor characterization," *Instrumentation and Measurement, IEEE Transactions on*, vol. 42, no. 2, pp. 360 –364, Apr. 1993.

[64] M. Pelk, L. de Vreede, M. Spirito, and J. Jos, "Base-band impedance control and calibration for on-wafer linearity measurements," in *ARFTG Conference Digest Spring, 2004. 63rd*, June 2004, pp. 35 – 40.

[65] R. Marchesani, "Digital precompensation of imperfections in quadrature modulators," *Communications, IEEE Transactions on*, vol. 48, no. 4, pp. 552 –556, Apr. 2000.

[66] "UTRA (BS) FDD; Radio Transmission and Reception," Technical Specification Group Radio Access Networks - 3rd Generation Partnership Project, 3GPP TS 25.104 V4.1.0 (2001-06), 2001.

[67] D. Hartskeerl, I. Volokhine, and M. Spirito, "On the optimum 2^{nd} harmonic source and load impedances for the efficiency-linearity trade-off of RF LDMOS power amplifiers," in *Radio Frequency integrated Circuits (RFIC) Symposium, 2005. Digest of Papers. 2005 IEEE*, June 2005, pp. 447 – 450.

[68] F. Verbeyst and M. Bossche, "Real-time and optimal PA characterization speeds up PA design," in *Microwave Conference, 2004. 34th European*, vol. 1, oct. 2004, pp. 431 –434.

[69] T. Williams, J. Benedikt, and P. Tasker, "Fully functional "real time" non-linear device characterization system incorporating active load control," in *Microwave Conference, 2006. 36th European*, sept. 2006, pp. 1610 –1613.

[70] P. Roblin, S. J. Doo, X. Cui, G. Jessen, D. Chaillot, and J. Strahler, "New ultra-fast real-time active load-pull measurements for high speed RF power amplifier design," in *Microwave Symposium, 2007. IEEE/MTT-S International*, jun 2007, pp. 1493 –1496.

[71] M. Marchetti, K. Buisman, M. Pelk, L. Smith, and L. de Vreede, "A low-cost pulsed RF & I-V measurement setup for isothermal device characterization," in *ARFTG Conference Digest Fall, 2007. 70th*, Nov. 2007.

[72] P. Colantonio, F. Giannini, E. Limiti, and V. Teppati, "An approach to harmonic load- and source-pull measurements for high-efficiency PA design," *Microwave Theory and Techniques, IEEE Transactions on*, vol. 52, no. 1, pp. 191 – 198, jan. 2004.

[73] F. van Rijs, R. Dekker, H. Visser, H. Huizing, D. Hartskeerl, P. Magnee, and R. Dondero, "Influence of output impedance on power added

efficiency of Si-bipolar power transistors," in *Microwave Symposium Digest., 2000 IEEE MTT-S International*, vol. 3, 2000, pp. 1945 –1948 vol.3.

[74] M. Squillante, M. Marchetti, M. Spirito, and L. de Vreede, "A mixed-signal approach for high-speed fully controlled multidimensional load-pull parameters sweep," in *Microwave Measurement Conference, 2009 73rd ARFTG*, jun 2009, pp. 1 –5.

[75] D. Barataud, F. Blache, A. Mallet, P. Bouysse, J.-M. Nebus, J. Villotte, J. Obregon, J. Verspecht, and P. Auxemery, "Measurement and control of current/voltage waveforms of microwave transistors using a harmonic load-pull system for the optimum design of high efficiency power amplifiers," *Instrumentation and Measurement, IEEE Transactions on*, vol. 48, no. 4, pp. 835 –842, aug 1999.

[76] D. Morgan, G. Edwards, A. Phillips, and P. Tasker, "Full extraction of PHEMT state functions using time domain measurements," in *Microwave Symposium Digest, 2001 IEEE MTT-S International*, vol. 2, 2001, pp. 823 –826 vol.2.

[77] G. Simpson, J. Horn, D. Gunyan, and D. Root, "Load-pull + NVNA = enhanced X-parameters for PA designs with high mismatch and technology-independent large-signal device models," in *ARFTG Microwave Measurement Symposium, 2008 72nd*, dec. 2008, pp. 88 –91.

[78] O. Jardel, F. De Groote, T. Reveyrand, J.-C. Jacquet, C. Charbonniaud, J.-P. Teyssier, D. Floriot, and R. Quere, "An electrothermal model for AlGaN/GaN power HEMTs including trapping effects to improve large-signal simulation results on high VSWR," *Microwave Theory and Techniques, IEEE Transactions on*, vol. 55, no. 12, pp. 2660 –2669, dec. 2007.

[79] R. Gaddi, J. Pla, J. Benedikt, and P. Tasker, "LDMOS electro-thermal model validation from large-signal time-domain measurements," in *Microwave Symposium Digest, 2001 IEEE MTT-S International*, vol. 1, 2001, pp. 399 –402 vol.1.

[80] M. Spirito, L. de Vreede, L. Nanver, S. Weber, and J. Burghartz, "Power amplifier PAE and ruggedness optimization by second-harmonic control," *Solid-State Circuits, IEEE Journal of*, vol. 38, no. 9, pp. 1575 – 1583, sept. 2003.

[81] D. Barataud, C. Arnaud, B. Thibaud, M. Campovecchio, J.-M. Nebus, and J. Villotte, "Measurements of time-domain voltage/current waveforms at RF and microwave frequencies based on the use of a vector network analyzer for the characterization of nonlinear devices-application to high-efficiency power amplifiers and frequency-multipliers optimization," *Instrumentation and Measurement, IEEE Transactions on*, vol. 47, no. 5, pp. 1259 –1264, oct 1998.

[82] S. Rehnmark, "On the calibration process of automatic network analyzer systems (short papers)," *Microwave Theory and Techniques, IEEE Transactions on*, vol. 22, no. 4, pp. 457 – 458, apr 1974.

[83] U. Lott, "Measurement of magnitude and phase of harmonics generated in nonlinear microwave two-ports," *Microwave Theory and Techniques, IEEE Transactions on*, vol. 37, no. 10, pp. 1506 –1511, oct 1989.

[84] D. Gunyan and Y.-P. Teoh, "Characterization of active harmonic phase standard with improved characteristics for nonlinear vector network analyzer calibration," in *Microwave Symposium Digest, 2008 IEEE MTT-S International*, june 2008, pp. 73 –79.

[85] A. Barel and Y. Rolain, "A microwave multisine with known phase for the calibration of narrowbanded nonlinear vectorial network analyzer measurements," in *Microwave Symposium Digest, 1998 IEEE MTT-S International*, vol. 3, jun 1998, pp. 1499 –1502 vol.3.

[86] C. Barrett, "Fractional/integer-N PLL basics," 1999.

[87] P. Blockley, D. Gunyan, and J. Scott, "Mixer-based, vector-corrected, vector signal/network analyzer offering 300 kHz-20 GHz bandwidth and traceable phase response," in *Microwave Symposium Digest, 2005 IEEE MTT-S International*, june 2005, p. 4 pp.

[88] A. Ferrero, V. Teppati, and B. Noori, "A generalized time-domain waveform test-set," in *Microwave Conference, 2008. EuMC 2008. 38th European*, oct. 2008, pp. 749 –752.

[89] M. Sipila, K. Lehtinen, and V. Porra, "High-frequency periodic time-domain waveform measurement system," *Microwave Theory and Techniques, IEEE Transactions on*, vol. 36, no. 10, pp. 1397 –1405, oct 1988.

[90] G. Kompa and F. van Raay, "Error-corrected large-signal waveform measurement system combining network analyzer and sampling oscilloscope capabilities," *Microwave Theory and Techniques, IEEE Transactions on*, vol. 38, no. 4, pp. 358 –365, apr 1990.

[91] J. Scott, J. Verspecht, B. Behnia, M. Vanden Bossche, A. Cognata, F. Verbeyst, M. Thorn, and D. Scherrer, "Enhanced on-wafer time-domain waveform measurement through removal of interconnect dispersion and measurement instrument jitter," *Microwave Theory and Techniques, IEEE Transactions on*, vol. 50, no. 12, pp. 3022 – 3028, dec 2002.

[92] A. Ramadan, A. Martin, T. Reveyrand, J.-M. Nebus, P. Bouysse, L. Lapierre, J. Villemazet, and S. Forestier, "Efficiency enhancement of GaN power HEMTs by controlling gate-source voltage waveform shape," in *Microwave Integrated Circuits Conference, 2009. EuMIC 2009. European*, sept. 2009, pp. 487 –490.

[93] M. Thorsell and K. Andersson, "Fast multiharmonic active load-pull system with waveform measurement capabilities," *Microwave Theory and Techniques, IEEE Transactions on*, vol. 60, no. 1, pp. 149 –157, jan. 2012.

[94] Agilent Technologies, "The microwave transition analyzer: a versatile measurement set for bench and test. Product note 70820-1," 1991.

[95] J. Verspecht, "Large-signal network analysis," *Microwave Magazine, IEEE*, vol. 6, no. 4, pp. 82 – 92, dec 2005.

[96] http://www.aeroflex.com/ams/metelics/micro-metelics-prods-comb.cfm.

[97] http://www.picosecond.com/product/category.asp?pd_id=22.

[98] http://www.hhft.de/index.php?page=rf&subpage=generators_p2.

[99] J. Verspecht and K. Rush, "Individual characterization of broadband sampling oscilloscopes with a nose-to-nose calibration procedure," *Instrumentation and Measurement, IEEE Transactions on*, vol. 43, no. 2, pp. 347 –354, apr 1994.

[100] T. Clement, P. Hale, D. Williams, C. Wang, A. Dienstfrey, and D. Keenan, "Calibration of sampling oscilloscopes with high-speed photodiodes," *Microwave Theory and Techniques, IEEE Transactions on*, vol. 54, no. 8, pp. 3173 –3181, aug. 2006.

[101] F. Vanaverbeke, W. De Raedt, D. Schreurs, and M. Bossche, "Real-time non-linear de-embedding," in *Microwave Measurement Conference (ARFTG), 2011 77th ARFTG*, june 2011, pp. 1 –6.

[102] J. Pedro and N. De Carvalho, "On the use of multitone techniques for assessing RF components' intermodulation distortion," *Microwave Theory and Techniques, IEEE Transactions on*, vol. 47, no. 12, pp. 2393 –2402, dec 1999.

[103] Agilent Technologies, *U9391C/F Comb generators 10 MHz to 50 GHz technical overview" (2009) Agilent Technologies.*

[104] M. P. van der Heijden, "RF amplifier design techniques for linearity and dynamic range," Ph.D. dissertation, Delft University of Technology, 2005.

[105] K. Buisman, "Device realization, characterization and modeling for linear RF applications," Ph.D. dissertation, Delft University of Technology, 2011.

[106] J. Bains, "Modular systems for RF and microwave measurements," in *Modern RF and Microwave Measurement Techniques*, V. Teppati, A. Ferrero, and M. Sayed, Eds. Cambridge University Press, 2013, ch. 7.

[107] L. Galatro, M. Marchetti, and M. Spirito, "60 GHz mixed signal active load-pull system for millimeter wave devices characterization," in *Microwave Measurement Symposium (ARFTG), 2012 80th ARFTG*, 2012, pp. 1–6.

[108] J. Verspecht and D. Root, "Polyharmonic distortion modeling," *Microwave Magazine, IEEE*, vol. 7, no. 3, pp. 44–57, 2006.

[109] B. Heinemann, R. Barth, D. Bolze, J. Drews, G. Fischer, A. Fox, O. Fursenko, T. Grabolla, U. Haak, D. Knoll, R. Kurps, M. Lisker, S. Marschmeyer, H. Rucker, D. Schmidt, J. Schmidt, M. Schubert, B. Tillack, C. Wipf, D. Wolansky, and Y. Yamamoto, "SiGe HBT technology with fT/fmax of 300GHz/500GHz and 2.0 ps CML gate delay," in *Electron Devices Meeting (IEDM), 2010 IEEE International*, 2010, pp. 30.5.1–30.5.4.

[110] V. D'Alessandro, I. Marano, S. Russo, D. Céli, A. Chantre, P. Chevalier, F. Pourchon, and N. Rinaldi, "Impact of layout and technology parameters on the thermal resistance of SiGe:C HBTs," in *Bipolar/BiCMOS Circuits and Technology Meeting (BCTM), 2010 IEEE*, 2010, pp. 137–140.

[111] M. Schroter, J. Krause, N. Rinaldi, G. Wedel, B. Heinemann, P. Chevalier, and A. Chantre, "Physical and electrical performance limits of high-speed Si GeC HBTs - Part II: lateral scaling," *Electron Devices, IEEE Transactions on*, vol. 58, no. 11, pp. 3697–3706, 2011.

[112] K. Manjanna, K. Buisman, M. Spirito, M. Marchetti, M. Pelk, and L. de Vreede, "Synthesized pulsed bias for device characterization," in *Microwave Measurement Symposium (ARFTG), 2013 81st ARFTG*, 2013, pp. 1–4.

Summary

Title: Mixed-Signal Instrumentation for Large-Signal Device Characterization and Modelling
By: Mauro Marchetti

This thesis concentrates on the development of advanced large-signal measurement and characterization tools to support technology development, model extraction and validation, and power amplifier (PA) designs that address the newly introduced third and fourth generation (3G and 4G) wideband communication standards. By exploiting an innovative mixed-signal approach, the measurement systems developed within this thesis work extend the limits of the current state-of-the-art large-signal characterization in terms of bandwidth, power range, speed and functionality. As described in **Chapter 1** these activities are needed to address the demands that follow from the ever-growing data transfer rates in modern telecommunication systems. Here the introduction of the new 3G and 4G communication standards, which make use of higher bandwidths and peak-to-average ratios, in combination with the necessity to reduce the power consumption of mobile networks, put very stringent demands on the power amplifier in the wireless transmitter. Since the PA is one of the dominant sources of energy consumption in the wireless network, it needs to be very efficient and linear over a wide frequency range and over a wide power span. Therefore, to accomplish this difficult mission, the PA designer has to rely on either an accurate nonlinear model of the active device to perform the design in a circuit simulator, or on device data resulting from load-pull measurements, which can accurately characterize the transistor performance parameters as a function of the load and source impedances at all frequencies of interest.

In order to support the development of compact device models which include self-heating and trapping effects, isothermal measurement systems are required. **Chapter 2** introduces the theory and the requirements for pulsed-RF and pulsed-DC measurements. Moreover, a new isothermal measurement system is presented, which provides the ability to measure with DC and RF

pulses as short as 200 ns, while featuring a very high dynamic range ($\approx$ 85 dB) under pulsed-RF conditions, which is independent on the duty-cycle. The system performance is discussed in detail through a set of benchmarks, and some examples on isothermal active device characterization are provided.

The second and dominant part of this thesis introduces a revolutionary active harmonic load-pull approach. Load-pull device characterization is fundamental to all activities related to PA design and PA development, from technology development, to model extraction and validation, to the actual power amplifier design. For this reason **Chapter 3** reviews conventional passive and active source and load-pull architectures, and discusses their basic limitations, with particular attention to the problems arising when characterizing devices with wideband complex modulated signals. Moreover, the requirements of active load-pull systems to perform high power measurements with complex modulated signals are also explained.

To solve the problems of conventional load-pull systems when dealing with wideband modulated signals, a novel active harmonic load-pull system based on a mixed-signal approach is described in detail in **Chapter 4**. The system developed during this thesis work enables the measurement of active devices up to 120 MHz of modulation bandwidth, and allows arbitrary control of the reflection coefficient in this band. Measurement data highlighting the system performance, and measurement results on active devices are presented.

To enhance the process of developing new transistor technologies and their application in very efficient and linear PAs, in **Chapter 5**, a new approach for enabling high-speed multidimensional source and load-pull parameter sweeps is introduced. The method described allows any combination of multiple parameters (e.g., input power and/or fundamental and harmonic load impedance) to be swept, at a very high speed, while maintaining all other parameters (e.g., second harmonic source impedance) accurately controlled to a user-defined value. Moreover, several measurements are reported, with particular emphasis on the high-power capabilities of the system, both in CW as well as under modulated signal excitations.

The option to measure time-domain voltage and current waveforms can provide significant insight into the actual device behavior, which benefits to power amplifier design, ruggedness evaluation, as well as to (database) model extraction and validation. In **Chapter 6** the basic theory behind the measurement of high frequency time-domain voltage and current waveforms at the device reference planes are discussed, and an extension to the mixed-signal load-pull system described in the previous chapters is presented, with particular attention on the requirements of the calibration device used for the system calibration. Furthermore an approach for time-domain waveform analysis of

multi-tone signals which are closely spaced in frequency is introduced.

To highlight the most unique capabilities of the mixed-signal load-pull system developed in this thesis, **Chapter 7** reports several relevant examples of significant applications. In particular an out-of-band linearity optimization of an HBT device, the characterization of a GaN device for high efficiency PA design, and some very high-power device measurements for base-station applications are described.

Chapter 8 finishes the thesis and gives the most important conclusions and the recommendations for future work.

Samenvatting

Titel: "Mixed-Signal" Meetsystemen voor de Grootsignaal Karakterisatie en Modellering van Componenten
Door: Mauro Marchetti

Dit proefschrift richt zich op de ontwikkeling van geavanceerde grootsignaal meet- en karakterisatietechnieken t.b.v. innovaties in: transistortechnologie, model-extractie / verificatie en RF vermogensversterkers voor de derde en vierde generatie (3G, 4G) breedbandcommunicatiestandaarden. Door gebruik te maken van een innovatieve "mixed-signal" aanpak (een combinatie van analoog en digitaal) zijn, in het kader van dit proefschrift, nieuwe oplossingen ontwikkeld die de limieten van de reeds bekende grootsignaalmeettechnieken overtreffen in termen van bandbreedte, vermogen, snelheid en functionaliteit. **Hoofdstuk 1** geeft de achtergrond waarom de activiteiten, beschreven in dit proefschrift, noodzakelijk zijn om aan de vraag van alsmaar hogere datasnelheden in draadloze netwerken te blijven voldoen. De introductie van de 3G en 4G communicatiestandaarden, welke gebruik maken van signalen met hogere bandbreedtes en amplitude variaties, leveren samen de wens om het energieverbruik van mobiele netwerken te verminderen. Dit leidt tot zeer strenge eisen voor de RF vermogensversterkers in de zenders van deze netwerken. Aangezien deze versterkers de grootste energieverbruikers zijn in een draadloos netwerk, moeten deze RF vermogensversterkers zeer efficiënt en lineair zijn over een voldoende breed frequentiebereik en uitgangsvermogen. Om aan deze hoge eisen te voldoen, vertrouwt de vermogensversterker ontwerper op niet-lineaire modellen van de actieve componenten in een netwerk simulator of hij maakt gebruik van 'load-pull' meetdata. Deze laatste aanpak kan nauwkeurig de optimale "werkcondities" van de transistor bepalen als functie van belasting- en bron-impedanties op alle vereiste frequenties.

Om de modelontwikkeling voor een actieve component te ondersteunen, welke "self-heating" and "trapping" omvat, is een isotherm meetsysteem noodzakelijk. **Hoofdstuk 2** introduceert de theorie en eisen aan zo'n gepulst RF/DC meetsysteem. Met deze kennis wordt een nieuw isothermmeetsys-

teem concept geïntroduceerd, welke de mogelijkheid heeft om zowel DC en RF met zeer korte pulsbreedtes (200 ns) te pulsen. Dit, met een zeer hoog dynamisch bereik ($\approx$ 85 dB) welke onafhankelijk is van de "duty cycle" (aan-uit verhouding). De prestaties van dit systeem zijn gedemonstreerd d.m.v. verschillende benchmarkmetingen en de isotherme karakterisatie van een aantal actieve componenten.

Het tweede en meest belangrijke onderdeel van dit proefschrift betreft de introductie van een revolutionaire actieve harmonische "load-pull" meetmethode. "Load-pull" component karakterisatie is het fundament waarop alle activiteiten m.b.t. vermogensversterker ontwerp en ontwikkeling zijn gebaseerd. Dit geldt zowel voor de ontwikkeling van transistortechnologie zelf, als voor de bijbehorende model extractie / verificatie en het uiteindelijke vermogensversterkerontwerp. **Hoofdstuk 3** bediscussieert de conventionele passieve en actieve "load-pull" architecturen met hun beperkingen, specifieke aandacht wordt gegeven aan de problemen die optreden wanneer de componenten worden gekarakteriseerd m.b.v. breedbandige complex-gemoduleerde signalen. Ter aanvulling worden de eisen verklaard die gesteld worden aan hoogvermogensmetingen met complex-gemoduleerde signalen. Om de problemen van conventionele "load-pull" systemen m.b.t. het gebruik van breedbandige complex-gemoduleerde signalen op te lossen, wordt een er nieuw actief harmonisch "load-pull" meetsysteem geïntroduceerd in **Hoofdstuk 4**. Dit "mixed-signal" meetsysteem maakt metingen van actieve componenten met 120 MHz modulatie bandbreedte mogelijk, terwijl de reflectiecoëfficiënt in deze bandbreedte vrij kan worden gekozen en gecontroleerd. De mogelijkheden van dit nieuwe meetsysteem worden gedemonstreerd d.m.v. meetdata m.b.t. het systeem zelf, alsmede door metingen aan actieve componenten.

Om de ontwikkelingen van nieuwe transistortechnologieën en hun gebruik in hoog-efficiënte en lineaire vermogensversterkers te bespoedigen, is in **Hoofdstuk 5** een nieuwe methode geïntroduceerd die zeer snelle 'load-pull' metingen met meerdimensionale parametervariaties mogelijk maakt. De geïntroduceerde methode staat het toe om iedere combinatie van parameters (bijvoorbeeld: ingangsvermogen en/of fundamentele en harmonische belasting impedantie) te variëren met zeer hoge snelheid, terwijl andere parameters (bijvoorbeeld: de tweede-harmonische bronimpedantie) nauwkeurig worden vastgehouden op een ingesteld waarde. Ook worden diverse hoogvermogens metingen beschreven, zowel voor continue signalen (CW) als voor complex-gemoduleerde signalen.

De mogelijkheid om tijddomein spanning- en stroom golfvormen te meten, geeft aanvullend inzicht in het gedrag van de actieve component. Dit biedt voordelen voor het vermogensversterkerontwerp, de robuustheid evaluatie, als-

mede voor (database) modelextractie en verificatie. In **Hoofdstuk 6** wordt de theorie voor het meten van tijddomein spanning- en stroomgolfvormen bij hoge frequenties aan een specifiek referentievlak geïntroduceerd. Om deze metingen te ondersteunen is het meetsysteem verder uitgebreid en wordt er gebruik gemaakt van een extra kalibratiecomponent. Extra aandacht wordt gegeven aan de specifieke eisen van dit kalibratiecomponent om nauwkeurige meetresultaten te kunnen garanderen. Verder wordt er een tijd-domein analyse / kalibratie methode beschreven welke geschikt is voor signalen met veel spectrale componenten binnen een beperkte bandbreedte.

Om de unieke mogelijkheden van de in dit proefschrift ontwikkelde meettechnieken te belichten, geeft **Hoofdstuk 7** diverse voorbeelden van relevante, praktische toepassingen. Beschreven zijn: de 'out-of-band' lineariteitsoptimalisatie van een HBT transistor, de karakterisatie van een GaN transistor voor een hoog-efficiënte vermogensversterker en enige metingen bij zeer hoge vermogensniveaus aan een transistor voor base-station applicaties.

Hoofdstuk 8 sluit dit proefschrift af met de belangrijkste conclusies en aanbevelingen voor toekomstig werk in dit vakgebied.

List of Publications

Journal Papers

M. Marchetti, "Mixed–signal active load pull: the fast track to 3G and 4G amplifiers," *Microwave Journal*, pp. 108–118, Sep. 2010.

C. Huang, P. J. Zampardi, K. Buisman, C. Cismaru, M. Sun, K. Stevens, J. Fu, **M. Marchetti** and L. C. N. de Vreede, "A GaAs junction varactor with a continuously tunable range of 9 : 1 and an OIP_3 of 57 dBm," *IEEE Electron Device Letters*, vol. 31, no. 2, pp. 108–110, Feb. 2010.

J. H. Qureshi, M. J. Pelk, **M. Marchetti**, W. C. E. Neo, J. R. Gajadharsing, M. P. van der Heijden and L. C. N. de Vreede, "A 90–W peak power GaN outphasing amplifier with optimum input signal conditioning," *IEEE Trans. Microwave Theory Tech.*, vol. 57, no. 8, pp. 1925–1935, Aug. 2009.

C. Huang, K. Buisman, **M. Marchetti**, L. K. Nanver, F. Sarubbi, M. Popadić, T. L. M. Scholtes, H. Schellevis, L. E. Larson and L. C. N. de Vreede, "Ultra linear low–loss varactor diode configurations for adaptive RF systems," *IEEE Trans. Microwave Theory Tech.*, vol. 57, no. 1, pp. 205–215, Jan. 2009.

M. Marchetti, M. J. Pelk, K. Buisman, W. C. E. Neo, M. Spirito and L. C. N. de Vreede, "Active harmonic load–pull with realistic wideband communications signals," *IEEE Trans. Microwave Theory Tech.*, vol. 56, no. 12, pp. 2979–2988, Dec. 2008.

C. Huang, L. C. N. de Vreede, F. Sarubbi, M. Popadić, K. Buisman, J. H. Qureshi, **M. Marchetti**, A. Akhnoukh, T. L. M. Scholtes, L. E. Larson and L. K. Nanver, "Enabling low–distortion varactors for adaptive transmitters," *IEEE Trans. Microwave Theory Tech.*, vol. 56, no. 5, pp. 1149–1163, May 2008.

Conference Papers

A. Kumar Manjanna, **M. Marchetti**, k. Buisman, M. Spirito, M. J. Pelk and L. C. N. de Vreede, "Device characterization for LTE applications with wideband baseband, fundamental and harmonic impedance control," in *Proc. 43rd European Microwave Conference, 2013*, Nuremberg, Germany, Oct. 2013.

K. Buisman, **M. Marchetti**, M. P. van der Heijden, P. J. Zampardi and L. C. N. de Vreede, "Evaluation of HBT device linearity using advanced measurement techniques," in *Proc. 43rd European Microwave Conference, 2013*, Nuremberg, Germany, Oct. 2013.

A. Kumar Manjanna, K. Buisman, M. Spirito, **M. Marchetti** and M. Spirito, M. Pelk and L. C. N. de Vreede, "Synthesized pulsed bias for device characterization," in *Proc. 81st Automatic RF Techniques Group Conf. (ARFTG2013)*, Seattle, WA, Jun. 2013.

L. Galatro, **M. Marchetti** and M. Spirito, "60 GHz mixed signal active load–pull system for millimeter wave devices characterization," in *Proc. 80th Automatic RF Techniques Group Conf. (ARFTG2012)*, San Diego, CA, Nov. 2012.

M. S. Alavi, F. van Rijs, **M. Marchetti**, M. Squillante, Tao Zhang, S. J. C. H. Theeuwen, Y. Volokhine, H. F. F. Jos, M. P. v.d Heijden, M. Acar and L. C. N. de Vreede, "Efficient LDMOS device operation for envelope tracking amplifiers through second harmonic manipulation," in *IEEE MTT-S Digest*, Baltimore, MD, June 2011.

M. Marchetti, R. Heeres, M. Squillante, M. Pelk, M. Spirito and L. C. N. de Vreede, "A mixed–signal load–pull system for base-station applications," in *Radio Frequency Integrated Circuits Symposium (RFIC)*, Anaheim, CA, May 2010, pp. 491–494.

M. Mirra, **M. Marchetti**, F. Tessitore, M. Spirito, L. C. N. de Vreede and L. Betts, "A multi–step phase calibration procedure for closely spaced multi–tone signals," in *Proc. 75th Automatic RF Techniques Group Conf. (ARFTG2010)*, Anaheim, CA, May 2010.

M. Squillante, **M. Marchetti**, M. Spirito and L. C. N. de Vreede, "A mixed–signal approach for high–speed fully controlled multidimensional load-pull parameters sweep," in *Proc. 73rd Automatic RF Techniques Group Conf. (ARFTG2009)*, Boston, MA, Jun. 2009.

L. C. N. de Vreede, M. Pelk, E. Neo, J. Qureshi, M. Spirito, M. Squillante, **M. Marchetti**, "Enhanced RF power amplifiers and device characterization setups using coherent mixed–signal techniques," in *11th Annual Wireless and Microwave Technology Conference (WAMICON)*, Melbourne, FL, April 2010.

M. Marchetti, K. Buisman, M. Pelk, L. Smith and L. C. N. de Vreede, "A low–cost pulsed RF & I-V measurement setup for isothermal device characterization," in *Proc. 70th Automatic RF Techniques Group Conf. (ARFTG2007)*, Tempe, AZ, Nov. 2007.

K. Buisman, C. Huang, A. Akhnoukh, **M. Marchetti**, L. C. N. de Vreede, L. E. Larson and L. K. Nanver, "Varactor topologies for RF adaptivity with improved power handling and linearity," in *IEEE MTT-S Digest*, Honolulu, HI, June 2007, pp. 319–322.

M. Marchetti, M. Pelk, K. Buisman, M. Spirito and L. C. N. de Vreede, "A pulsed network analyzer for high dynamic range isothermal measurements," in *Proc. 68th Automatic RF Techniques Group Conf. (ARFTG2006)*, Broomfield, CO, Dec. 2006.

Patents

M. Marchetti, M. J. Pelk, L. C. N. de Vreede, "Open loop load pull arrangement with determination of injections signals," *World Intellectual Property Organization Patent No. 2009131444*, 30 Oct. 2009.

Book Chapters

M. Spirito and **M. Marchetti**, "Broadband large signal measurements for linearity optimization," in *Modern RF and Microwave Measurement Techniques*, V. Teppati, A. Ferrero, and M. Sayed, Eds. Cambridge University Press, 2013, ch. 14.

Workshop and Short Courses

M. Spirito and **M. Marchetti**, "Mixed–signal active load pull, the fast track to 3G and 4G amplifiers," in *Short Course on Microwave Mea-*

surements, 81st Automatic RF Techniques Group Conf. (ARFTG2013, San Diego, CA, Nov. 2012.

M. Marchetti, M. Squillante, M. Pelk, M. Spirito and L. C. N. de Vreede, "Active harmonic load–pull for LDMOS devices in base station applications," in *Workshop on Silicon Characterization from MHz to THz, 40th European Microwave Conference, 2010*, Paris, France, Sep. 2010.

M. Marchetti, M. Squillante, M. Pelk, M. Spirito and L. C. N. de Vreede, "A mixed–signal approach for large–signal device characterization with wideband modulated signals," in *Workshop on Advanced Non-Linear Characterization of RF and Microwave Components, 39th European Microwave Conference, 2009*, Rome, Italy, Sep. 2009.

Acknowledgments

My personal experience as a Ph.D. could very well be summarized with this old Neapolitan say: "Dicette 'o pappice vicino 'a noce: damme 'o tiemp ca te spertoso" ("The worm told the walnut: give me time and I will pierce you"). That is to say that with perseverance, a good degree of stubbornness and a sufficient amount of time, everything can be accomplished. Since I started as a Ph.D. student in July of 2006, it did take quite some time to complete this journey. Through all this time, I had the chance to meet a lot of exceptional people, who contributed to this thesis in many different ways, and without whom I could have never reached this goal. To all of you goes my unlimited gratitude.

First of all I would like to thank my promotor Prof. John Long for his many advices and for his precious feedback on my thesis. Furthermore, I would like to thank my co-promotor Dr. Leo de Vreede. Without his constant guidance, support and scientific creativity I would have never made it this far. Thank you for believing in me and for giving me the opportunity first to pursue a Ph.D., then to start a company together. A special acknowledgment also goes to my other advisor and also co-founder of Anteverta, Dr. Marco Spirito. Since I arrived in Delft to carry out my master thesis, you have proved to be a constant source of knowledge, a good friend, and the most talented person I know in making the most amazing plots and figures.

For accepting to participate in my Ph.D. defense and for taking the time to review my thesis, I would like to thank all the members of my doctoral committee: Prof. Valeria Teppati, Prof. Rik Jos, Prof. Dominique Schreurs, Dr. Marc Vanden Bossche, Prof. Lis Nanver and Prof. Andrea Neto. I am also grateful to Prof. Lina Sarro for frequently reminding me, and all my co-promotors, that some things in life do need to end (especially the book you are now reading).

Some time after I commenced my Ph.D., my doctoral research went hand in hand with my adventure as an entrepreneur. In this perspective I have to express my gratitude to all the people not mentioned so far that have been involved with successfully starting up and growing Anteverta.

First and foremost I have to thank Michele Squillante for too many things to mention. To name a few, thank you for developing big part of the current load-pull software, for sharing most of the burden and many late evenings of work without ever complaining, for the sausage with beans and the occasional mozzarella, and most of all for being a good friend. I would also like to acknowledge the other two members of the current Anteverta team for their hard work, commitment and good spirit, Ajay Kumar Manjanna and Giampiero "'o 'mericano" Esposito (who has joined us and found the new continent). This is the proper moment to also thank Marco Pelk for being able to solve most of the practical technical issues we encountered and for knowing the answer to some of the most difficult questions.

I also want to express my appreciation for Han Oey, Paul Althuis and Ronald Gelderblom and all the other people of the Delft Valorisation Center for their guidance during the start-up of Anteverta and for their continuous support.

A special acknowledgment goes to all the people at NXP that have believed in us and in our system when we were still writing lines of code to run a measurement. Particularly, I am grateful to Rob Heeres for sharing his knowledge, for the continuous feedback, for his patience with the early versions of the software and for being one of the most sincere supporters of our system. I would also like to thank Steven Theeuwen for generously providing many test devices for us to write papers, test new software and sometimes to destroy. A special acknowledgment also goes to Dr. Mark van der Heijden for many discussions and for even bringing customers to us. Furthermore, I have to thank Dr. Martino Lorenzini for the many measurement sessions and for providing the GaN devices, Rob Bubeck, Angelo Andres, Petra Hammes and Lex Harm for their feedback and for many useful discussions.

I would also like to thank all the people at Maury Microwave for helping us in turning the research shown in this thesis into a commercial product. In particular, I have to thank Steve Dudkiewicz for the many advices and almost daily Skype calls.

Carrying out my Ph.D. first in the HiTec group, then in the ELCA group, has proven to be a very enjoyable experience. I have had the pleasure to work with some of the brightest and most interesting people I know. First of all I am indebted to Dr. Koen Buisman for being always the first user and debugger of my measurement systems, for answering my many questions about device physics, for translating the summary and propositions of this thesis in Dutch, and for a whole lot of other things. I have also had the pleasure to work closely with Dr. Edmund Neo, Dr. Jawad Qureshi and Dr. Cong Huang to whom goes my gratitude. Furthermore, for the enjoyable atmosphere and the

many fun times I would like to acknowledge my colleagues Morteza Alavi, Rui Hou, David Calvillo Cortes, Luca Galatro, Gennaro Gentile, Yi Zhao, Akshay Visweswaran. I would also like to thank Atef Akhnouk for his help in the measurement room, for his phone calls to the Dutch tax office on my behalf, and for continuously reminding me to be careful. I would also like to thank Marysia Lagendijk, Marian Roozenburg, Bianca Knot and Marion de Vlieger for their support.

Being far from home is never easy, therefore I would like to thank all the friends that have made me feel at home both in Delft and in Eindhoven: Luigi "van der Appels" Mele, Agata Ŝakić who shares my same chocolate addiction, Riccardo "Materassi" Donatantonio, Luis Alberto Cusati nonostante non sia il mio presidente, Roberto "Johnny" Amabile with whom I'll always be happy to go surfing, Francesco Vitale and all his wooden spoons, Salvatore "rum e cotechino" Russo my MATLAB GUI teacher, Fabio Santagata, Elina Iervolino, Alessandro "the wall" Baiano, Maria De Biase, Andrea Ingenito and his wonderful light blue Vespa, Daniel Tajari Mofrad, Benjamin Mimoun, Luigi La Spina, Giovanna Razzano, Francesco Sarubbi, Gianpaolo Lorito, Theodoros Zoumpoulidis, Olindo Isabella, Joelle Olivet, Ghazaleh Nazarian, Vladimir "the professor" Jovanovic, Yann "purpette" Civale, Giuseppe Fiorentino, Bruno Morana, the Andricciola's, the De Maio's, the Tripodi's, Fabio Sebastiano the master of beer, Elisa "Dr. House" Buonanno, Salvo Drago, Lisa de Vries, Alberto Fazzi, Laura Pirani, Gerard Villar Pique, Muhammed Bolatkale, the Van der Weide's, the "6 o' clock heroes" football team.

Thanks to my friends back at home (who are now spread throughout the world) because when I am back at home it feels like I never left: Giacomo "o' So'" Sozio, Alessandro "l'avvocato" Caprio, Ciro Pileggio, Marco "o' lion'" Leone, Michele "sapone" Esposito, Francesco Miglino, Francesco Liquido, Claudio "culo" Esposito, Andrea "o' So' grande" Sozio, Luca Russo, Alfonso "pivell" Losco, Roberta "Enzo" Esposito.

Being myself an Italian man from the South, you should know that for us (and probably not only for us), family is the most important thing (and no, not in "the Godfather" kind of way). Truly, life without family is like a babà (typical Neapolitan dessert) without rum.

I would like to thank all my relatives, my aunts and uncles, my parents in law Carmela e Antonio Spella, Claudio "maestro spigola" Spella, Simona "a milanese" De Toni, Francesca Spella, Giovanni Colacurcio e la piccola Giovanna. Thanks to them all for their sustained encouragement and support.

I am grateful to my sister for bringing some mess (and a lot more fun) into my super organized world while growing up together, for being my fashion

advisor, and for coming to visit me in the Netherlands more than I have gone to visit her in Gorizia. I would also like to thank the new addition to the family Salvo Pennisi, who some day will hopefully catch some fresh fish in Palinuro when I am there.

I will always be grateful to my parents for raising me with love, for their continuous encouragements, unconditional support and for making me what I am today. Although we are geographically so distant now, we will always be close to each other.

To conclude, I want to express my love and profound appreciation to my wife Maristella. Thanks for lighting up my existence and for facing life with me while supporting me every step of the way: without you no achievement would be possible. Finally, thanks to my wonderful little son Matteo, because you are my purpose of life and whatever you will grow up to be, you will always be my biggest achievement.

About the Author

Mauro Marchetti was born in Naples, Italy, in 1981. He received his B.S. and M.Sc. degrees (*cum laude*) in electrical engineering from the "Università degli studi di Napoli Federico II", Naples, Italy, in 2004 and 2006 respectively.

In 2006 he joined the Electronic Research Laboratory (ELCA) of Delft University of Technology, The Netherlands, where he carried out his Ph.D. research on the development and implementation of mixed-signal instrumentation for large signal device characterization and modelling.

In 2010 he co-founded and was appointed CEO of Anteverta-mw B.V., a spin-off company of Delft University providing mixed-signal harmonic load-pull measurement systems.